

University of Warwick institutional repository: <http://go.warwick.ac.uk/wrap>

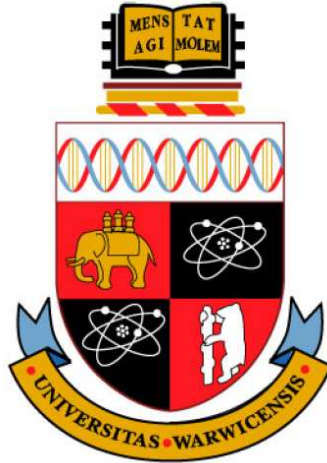
**A Thesis Submitted for the Degree of PhD at the University of Warwick**

<http://go.warwick.ac.uk/wrap/36763>

This thesis is made available online and is protected by original copyright.

Please scroll down to view the document itself.

Please refer to the repository record for this item for information to help you to cite it. Our policy information is available from the repository home page.



# **Finite-Element Time-Domain Modelling of Cylindrical Structures with a Modal Non-Reflecting Boundary Condition**

by

**Konstantinos Bavelis**

Submitted in Partial Fulfilment of the Requirement for the  
**Degree of Doctor of Philosophy in Engineering**

School of Engineering  
**University of Warwick**

**December 2010**

## Table of contents

Table of contents	i
List of Figures and Tables	v
List of Acronyms	x
Acknowledgements	xi
Declaration	xii
Summary	xiii
Publications associated with this work	xv
<b>Chapter 1:</b> Basic Theory and overview	1
1.1 Introduction	1
1.2 Key concepts of cylindrical structures	2
1.2.1 Problem description	2
1.2.2 Maxwell equations and wave equations	4
1.2.3 Radar cross section	5
1.3 Finite-element method	7
1.3.1 Discretisation of domain	9
1.3.2 Elemental approximation with interpolation functions	10
1.3.3 Assembly of the system of equations	10
1.3.4 Solution of the system of equations	11
1.3.5 Post-processing	12
1.4 Frequency and time domain considerations	12
1.5 Potential engineering applications	13

References	15
 <b>Chapter 2: Scattered field FETD-MNRBC formulation</b>	 18
2.1 Introduction	18
2.2 Scattered field concept	20
2.3 FEFD formulation	22
2.4 Application of truncation boundary conditions	23
2.4.1 First order absorbing boundary condition	23
2.4.2 Modal nonreflecting boundary condition	24
2.5 Geometric Discretisation of the FEFD formulation in terms of isoparametric elements	26
2.6 FETD-MNRBC Formulation	30
2.7 Numerical Results	34
2.8 Scientific contribution and future work	42
References	44
 <b>Chapter 3: VF approximation of a cylindrical boundary kernel</b>	 48
3.1 Introduction	48
3.2 Vector Fitting approximation	49
3.3 Cylindrical boundary kernels	51
3.3.1 FETD-MNRBC form	51
3.3.2 Generic form	52
3.3.3 Relation between the two forms	54
3.4 Numerical Results	56
3.4.1 Effect of input parameters	56

3.4.2 VF approximation of boundary kernels	59
3.4.3 Effect on FEM accuracy	67
3.5 Scientific contribution and future work	68
References	70
 <b>Chapter 4</b> Total field FETD-MNRBC formulation	 72
4.1 Introduction	72
4.2 FEFD formulation and application of modal nonreflecting boundary condition	73
4.3 FETD formulation and application of modal nonreflecting boundary condition	77
4.4 Numerical Results	81
4.5 Scientific contribution and future work	87
References	89
 <b>Chapter 5:</b> Periodic FETD-MNRBC formulation	 91
5.1 Introduction	91
5.2 Frequency domain formulation	92
5.2.1 Periodic cylindrical harmonics	92
5.2.2 Scattered field formulation	96
5.2.3 Total field formulation	98
5.3 Time domain formulation	99
5.3.1 Incident Field harmonics	100
5.3.2 Scattered field formulation	106
5.3.3 Total field formulation	107
5.4 Numerical Results	109
5.5 Scientific contribution and future work	116

References	118
<b>Chapter 6</b> Sparse-FETD-MNRBC formulation	120
6.1 Introduction	120
6.2 Scattered field FETD-MNRBC for dielectrics	122
6.2.1 Formulation	122
6.2.2 Numerical results	124
6.3 Sparse-FETD-MNRBC	125
6.3.1 Formulation	126
6.3.2 Numerical results	130
6.4 Scientific contribution and future work	134
References	135
<b>Chapter 7</b> Conclusions and Future work	137
References	140
<b>Appendices</b>	
<b>Appendix A</b> Scattered field harmonics	141
<b>Appendix B</b> First order absorbing boundary condition derivation	145
<b>Appendix C</b> Matrices entries	147
<b>Appendix D</b> Limits of functions $U_n$ and $G_n$	150
<b>Appendix E</b> Mathematical details of periodic formulations	156
<b>Appendix F</b> Effect of time delay to the VF approximation of the incident field components	164

## List of Figures and Tables

### Chapter 1

Fig 1.1	Three dimensional representation of the problem	3
Fig 1.2.	Two dimensional representation of the problem	3
Fig. 1.3	Depiction of the domain $\Omega$ and the boundary $\Gamma$	8
Fig. 1.4	Example of a mesh of square scatterer	10
Fig. 1.5	Planar and cylindrical RF/microwave absorbers	14

### Chapter 2

Fig. 2.1.	TE polarized plane wave scattering from a PEC cylinder of arbitrary cross-section	22
Fig. 2.2.	(a) The 8-noded curvilinear quadrilateral surface element and its square reference element. (b) The 3-noded curvilinear line element and its linear reference element	28
Fig. 2.3.	(a) Circular cylinder geometry (b) FE mesh	39
Fig. 2.4.	Numerical results of the circular scatterer using 1 <sup>st</sup> order Absorbing Boundary Condition, $\theta=\pi-\phi$ (a) Bistatic scattering width normalized with $\lambda$ (b) Error of Bistatic scattering width.	39
Fig. 2.5.	Numerical results of the circular scatterer using MNRBC, $\theta=\pi-\phi$ (a) Bistatic scattering width normalized with $\lambda$ (b) Error of Bistatic scattering width.	40
Fig. 2.6.	(a) Square cylinder geometry (b) FE mesh. The square side length is $s = \lambda/\pi$ .	40
Fig. 2.7.	Bistatic scattering width of the square scatterer, $\theta=\phi-3\pi/4$ .	41
Fig. 2.8.	(a) Triangular cylinder geometry (b) FE mesh.	41
Fig. 2.9.	Bistatic scattering width normalized with $\lambda$ of the triangular scatterer in dB, $\theta=\phi-\pi$ .	42
Table 2.1	Simulation parameters	38

### Chapter 3

Fig 3.1	Derivation of function $U_n$	55
Fig 3.2	$U_{15}$ comparison (a) normal x axis (b) logarithmic	57
Fig 3.3	Absolute error comparisons (a) $f_{max}=0.1\text{Hz}$ , $f_{max}=1\text{Hz}$ , $f_{max}=4\text{Hz}$ and $f_{max}=10\text{Hz}$ (b) $f_{max}=100\text{Hz}$ , $f_{max}=1\text{KHz}$ , $f_{max}=10\text{KHz}$ and $f_{max}=100\text{KHz}$ (c) $f_{max}=1\text{MHz}$ , $f_{max}=10\text{MHz}$ , $f_{max}=100\text{MHz}$ and $f_{max}=1\text{GHz}$	58
Fig 3.4	Plots of (a) $10\log_{10} e_{15}(s=j2\pi f) $ versus frequency $f$ for 4, 8, 40, 400 and 4000 (b) $10\log_{10} e_{15}(s=j2\pi f) $ versus frequency $f$ for 40, 400 and 4000	58
Fig 3.5	Plots of $ U_n(s=j2\pi f) $ and $10\log_{10} e_n(s=j2\pi f) $ versus frequency $f$ for $n = 1, 2, 3, 4$ .	60
Fig 3.6	Plots of time domain functions and differences for $n = 1, 2, 3, 4$	63
Fig 3.7	Plots of $ U_n(s=j2\pi f) $ and $10\log_{10} e_n(s=j2\pi f) $ versus frequency $f$ for $n = 0, 5, 10, 15$ .	64
Fig 3.8	Plots of $ G_n(s=j2\pi f) $ and $10\log_{10} e_n(s=j2\pi f) $ versus frequency $f$ for $n = 0, 5, 10, 15$ .	65
Fig. 3.9	Plots $10\log_{10} e_n(\omega) $ versus frequency $f$ for $\rho = 0.5\text{m}$	66
Fig. 3.10	Plots $10\log_{10} e_n(\omega) $ versus frequency $f$ for $\rho = 1\text{m}$	66
Fig. 3.11	Plots $10\log_{10} e_n(\omega) $ versus frequency $f$ for $\rho = 2\text{m}$	67
Fig 3.12	Comparison for the BSW (a) circular scatterer (b) triangular scatterer	68
Table 3.1	VECTFIT computed parameters	61

### Chapter 4

Fig. 4.1.	(a) Circular cylinders geometry (b) FE meshes	84
Fig. 4.2.	Bistatic scattering width normalized with $\lambda$ of the PEC circular scatterer, $\theta=\pi-\phi$ .	84
Fig. 4.3.	Bistatic scattering width normalized with $\lambda$ of the PEC circular scatterer surrounded with dielectric, $\theta=\pi-\phi$ .	85
Fig. 4.4	Bistatic scattering width normalized with $\lambda$ of the dielectric circular scatterer	85



	for (a) TE and TM (b) polarization, $\theta=\pi-\phi$ .	
Fig. 4.5.	(a) Square cylinder geometry (b) FE mesh	86
Fig. 4.6	Bistatic scattering width normalized with $\lambda$ of the dielectric square scatterer [6] for TE (a) and TM (b) polarization, $\theta=\pi-\phi$ .	86
Fig. 4.7.	(a) Square cylinder geometry (b) FE mesh	87
Fig. 4.8.	Bistatic scattering width normalized with $\lambda$ of the dielectric square scatterer [7] for TE (a) and TM (b) polarization, $\theta=\phi+\pi/4$	87
Table 4.1	Simulation parameters	82
<b>Chapter 5</b>		
Fig. 5.1	(a) The physical geometry of the problem (b) the unit-cell	93
Fig. 5.2	Comparison of the exact incident field against the sum of harmonics (a) Real part (b) Imaginary part (c) Error	94
Fig. 5.3	Numbers of the geometric parts in the unit-cell	97
Fig. 5.4	Decomposition of the incident field harmonics	102
Fig. 5.5	For $\nu_0 = 0$ (a) frequency domain comparison (b) absolute error (c) time domain function	103
Fig. 5.6	For $\nu_0 = 15$ (a) frequency domain comparison (b) absolute error (c) time domain function	104
Fig. 5.7	(a) Frequency domain comparison (b) absolute error	105
Fig. 5.8	(a) Time domain comparison (b) absolute error	105
Fig. 5.9.	Circular PEC cylinder (a) Full mesh (b) Unit-cell	113
Fig. 5.10.	Square PEC cylinder (a) Full mesh (b) Unit-cell	113
Fig. 5.11.	Circular PEC cylinder surrounded by dielectric (a) Full mesh (b) Unit-cell	113
Fig. 5.12.	BSW normalized with $\lambda$ of the circular PEC scatterer for scattered field formulation	115

Fig. 5.13.	BSW normalized with $\lambda$ of the circular PEC scatterer for total field formulation	115
Fig. 5.14.	BSW normalized with $\lambda$ of the square PEC scatterer for total field formulation	116
Fig. 5.15.	BSW normalized with $\lambda$ of the PEC circular scatterer with dielectric for total field formulation	116
Table 5.1	Simulation parameters	111

## Chapter 6

Fig. 6.1.	Bistatic scattering width normalized with $\lambda$ of the dielectric square scatterer [9] for TE polarization, $\theta=\phi+\pi/4$	125
Fig. 6.2.	Bistatic scattering width normalized with $\lambda$ of the dielectric circular scatterer [10] for TE polarization, $\theta=\pi-\phi$ .	125
Fig. 6.3.	Bistatic scattering width normalized with $\lambda$ of the circular scatterer, $\theta=\pi-\phi$ for (a) 40ps; (b) 10ps; (c) 5ps and (d) 1ps.	131
Fig. 6.4.	Error and relative error of Bistatic scattering width for Sparse-FETD	132
Fig. 6.5.	Error and relative error of Bistatic scattering width for Standard-FETD	132
Fig. 6.6.	Bistatic scattering width of the square scatterer, $\theta=\phi-3\pi/4$ . for (a) 25ps; (b) 5ps.	133
Fig. 6.7.	Bistatic scattering width normalized with $\lambda$ of the triangular scatterer in dB, $\theta=\phi-\pi$ for (a) 40ps; (b)10ps.	133
Table 6.1	Computing Time Comparisons	133

## Appendix E

Fig. E.1	Decomposition of the derivative of the incident field harmonics	160
Fig. E.2	For $\nu_0 = 0$ (a) frequency domain comparison (b) absolute error (c) time domain function	161
Fig. E.3	For $\nu_0 = 15$ (a) frequency domain comparison (b) absolute error (c) time domain function	162

Fig. E.4	(a) Frequency domain comparison (b) absolute error	162
Fig. E.5	(a) Time domain comparison (b) absolute error	163

## Appendix F

Fig. F.1.	Delay 700 timesteps (a) frequency domain comparison (b) frequency domain error (c) time domain comparison (d) time domain error	165
Fig. F.2.	Delay 1000 timesteps (a) frequency domain comparison (b) frequency domain error (c) time domain comparison (d) time domain error	166
Fig. F.3.	Delay 1500 timesteps (a) frequency domain comparison (b) frequency domain error (c) time domain comparison (d) time domain error	167
Fig. F.4.	Delay 2000 timesteps (a) frequency domain comparison (b) frequency domain error (c) time domain comparison (d) time domain error	167
Fig. F.5.	Delay 0 timesteps (a) frequency domain comparison (b) frequency domain error (c) time domain comparison (d) time domain error	168
Fig. F.6.	Delay 0 timesteps (a) $\nu_\theta=0$ (b) $\nu_\theta=5$ (c) $\nu_\theta=10$ (d) $\nu_\theta=15$	169
Fig. F.7.	Time domain shifting by 700 timesteps (a) time domain comparison (b) error	169
Fig. F.8.	Delay 0 timesteps, kill=0 (a) frequency domain comparison (b) frequency domain error (c) time domain comparison (d) time domain error	170
Fig. F.9.	Delay 0 timesteps, kill=0 (a) $\nu_\theta=0$ (b) $\nu_\theta=5$ (c) $\nu_\theta=10$ (d) $\nu_\theta=15$	171

## List of Acronyms

ABC	Absorbing Boundary Condition
BC	Boundary Condition
BSW	Bistatic Scattering Width
FE	Finite Element
FEM	Finite Element Method
FEFD	Finite Element Frequency Domain
FETD	Finite Element Time Domain
FT	Fourier Transform
ILT	Inverse Laplace Transform
LHS	Left Hand Side
LT	Laplace Transform
MNRBC	Modal Non-Reflecting Boundary Condition
PBC	Periodic Boundary Condition
PEC	Perfect Electric Conductor
PMC	Perfect Magnetic Conductor
RC	Recursive Convolution
RHS	Right Hand Side
RCS	Radar Cross-Section
TE	Transverse Electric
TM	Transverse Magnetic
VF	Vector Fitting
VFG	Vector Fitting $G_n$ function
VFU	Vector Fitting $U_n$ function

## **Acknowledgments**

I wish to express my deep gratitude to my supervisor Dr Christos Mias for his guidance, support and understanding in all steps and aspects of this work over the last years. His academic excellence and scientific integrity have been invaluable lessons for me. I feel indebted to him for the knowledge and research experience that he shared with me and also for the persistent, honest and hard working approach to life that he taught me. Furthermore it would be an omission if I did not politely thank him for his kindness, succour and humanely approach to all my personal issues and difficulties.

I would like to sincerely thank Prof. Evor Hines and Dr Mark Leeson, my PhD progress panel members, for their advices, support encouragement and trust on my progress over the years of my studies.

I wish to acknowledge the University Studentship from University of Warwick which has been not only a financial support but most importantly a source of motivation and continuous encouragement.

I would like to acknowledge the facilities provided by the University of Warwick and the support of all the services of University of Warwick which significantly made my life easier and helped me in all levels.

I acknowledge two specific contributions to my research which are the Harwell Subroutine Library, Harwell Laboratory, Oxfordshire, UK and Netlib Repository.

I would like to thank my family for bravely standing next to me every step of the way in fulfilling this dream. The completion of this work makes us all very happy but I am sure that in the years to come we will reflect on this experience and feel more proud than happy.

## **Declaration**

This dissertation is the result of my own work except where acknowledgement is given. The acknowledgement indicates the extend to which I have availed myself of work of others. The work presented in this dissertation is original except where references to the work of others are given.

The dissertation is not substantially the same as any that I have submitted for a degree, diploma or other qualification at any other University. I further state that no part of my dissertation has already been or being submitted for any such degree, diploma or qualification.

Konstantinos Bavelis

December 2010

## Summary

This dissertation presents Galerkin weighted residual Finite-Element Time-Domain (FETD) formulations using a 2D cylindrical modal non-reflecting boundary condition (MNRBC) for the modelling of plane wave scattering from cylindrical structures of arbitrary cross-section surrounded by free space.

**Chapter 1** begins by presenting the motivation for this work. Key concepts regarding cylindrical geometries are introduced at this stage. The Galerkin weighted residual Finite-Element method is briefly outlined.

**Chapter 2** presents a novel scattered field FETD-MNRBC formulation for the transverse electric polarisation of a modal non-reflecting boundary condition for plane wave scattering from perfectly electrically conductive (PEC) cylindrical structures of arbitrary cross-section. The boundary condition is based on a Vector-Fitting (VF) approximation of the boundary kernel appearing in the time-domain formulation. The convolution integral appearing in the time-domain formulation of the boundary condition is calculated recursively using the Vector-Fitting coefficients. Accurate numerical results are shown for the bistatic scattering width (BSW) that validate the approach.

**Chapter 3** focuses on the VF approximation of the cylindrical boundary kernel. Two approaches are investigated; the so called Vector-Fitting G function approximation (VFG) and the Vector-Fitting U function approximation (VFU). Both approaches produce satisfactory finite-element results with the VFU being more versatile.

**Chapter 4** presents, for the first time, the total field FETD-MNRBC formulation for both transverse electric and transverse magnetic polarisations. The VFU approach is

employed. The structures considered in this chapter are not only PEC cylinders but also dielectric ones of various cross-sections and various values of relative permittivity and permeability. The numerical results demonstrate the good accuracy of this formulation.

**Chapter 5** combines the cylindrical modal non-reflecting boundary condition with the Floquet theorem and extends this formulation, for the first time, to azimuthally periodic cylinders using scattered and total field time-domain formulations. The advantages and disadvantages of the periodic modal non-reflecting boundary condition approach are discussed and numerical results for the BSW are shown.

**Chapter 6** presents a novel sparse-matrix scattered field FETD-MNRBC formulation in which the fully dense submatrices associated with the boundary integral are avoided. Through numerical results the accuracy of the proposed formulation is investigated.

**Chapter 7** concludes the work by summarizing the main achievements and discussing its impact in electromagnetics.



## **Publications associated with this work**

### **Journal manuscripts**

- [1] K. Bavelis and C. Mias, “Vector fitting realisation of exact time domain modal nonreflecting boundary condition”, *Electronic Letters*, vol. 46, no. 11, pp 760-761, 2010.
- [2] K. Bavelis and C. Mias, “A Sparse matrix methodology for Finite Element for Time Domain modal non-reflecting boundary condition”, *IET Microwaves Antennas and Propagation*, submitted.
- [3] K. Bavelis and C. Mias, “On the accuracy of the Vector Fitting approximations of a cylindrical non-reflecting boundary kernel”, *Microwave and Optical Technology Letters*, submitted.
- [4] K. Bavelis and C. Mias, “Finite-Element Time-Domain modelling of cylinders with angular periodicity” *IET Microwaves Antennas and Propagation*, submitted.

### **Presentations**

- [1] K. Bavelis and C. Mias, “Modelling of plane wave scattering from dielectric cylinders using a scattered field Finite Element formulation ”, *Second UK URSI Festival of Radio Science, University of Leicester*.

*We will either find a way, or make one*

Hannibal

# CHAPTER 1

## Basic Theory and Overview

### 1.1 Introduction

The scope of this work was the derivation of versatile Finite-Element Time-Domain (FETD) formulations for modelling of plane wave scattering from cylindrical structures. Despite their applications the published work on them is not as extensive as for planar structures. Moreover the mathematical difficulties make them more interesting and challenging as a research objective.

For the simulation of the structures studied in this work the FETD method was preferred for specific reasons. The Finite Element Method (FEM) is a widely studied method for electromagnetic use [1-4] and thus there is a solid background to work on. It has the advantage of being very flexible for the simulation of complicated structures. By definition cylindrical structures are more complicated than their planar equivalents.

Moreover time domain methods have certain advantages over frequency domain ones [5-7]. They are computationally more efficient since wideband data can be obtained from a single run and directly simulate nonlinear and time-varying problems [5-7].

Another important aspect is the originality of the area. The modal non-reflecting boundary condition (MNRBC) is developed for cylindrical structures using the FETD method in this work for the first time.

After the presentation of the motivation for this work, this chapter proceeds to demonstrate the fundamental concepts of cylindrical structures. It then provides a short overview of the FEM with focus on the points that are incorporated in this work.

An important issue, that of the relation of the frequency and time domains is then tackled. The chapter closes with the presentation of potential applications of cylindrical scatterers in engineering practice.

## **1.2 Key concepts of cylindrical structures**

This section reviews the basic electromagnetic theory along with the aspects of it that are of extreme relevance and importance in this work. The presentation begins with the demonstration of the physical problem studied in this work. It proceeds with Maxwell equations and wave equations which constitute the cornerstone of every electromagnetic problem. Next the focus is on the field decomposition in harmonics which is the base for the expression of the MNRBC. A practical measurement for scattering from cylinders is the Radar cross section (RCS) and this is the reason it is used in this work as the main accuracy check for the approaches and is reviewed here.

### **1.2.1 Problem description**

The case considered is that of a cylindrical structure uniform along the z-axis with arbitrary cross-section in the x-y plane. The depiction of the problem is presented in Fig.1.1 and its two-dimensional equivalent in Fig.1.2. The cylinder is surrounded by free space.

One very important concept based on which the MNRBC is derived is the expression of the scattered field as a summation of harmonics. This can be found in [8-11] and the proof is included in Appendix A. The scattered field  $\tilde{\Phi}^{sc}$  from a cylinder can be expressed as a summation of harmonics in the form

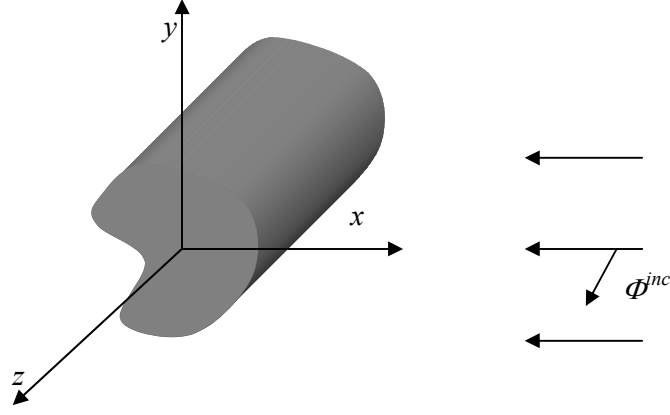


Fig 1.1. Three dimensional representation of the problem

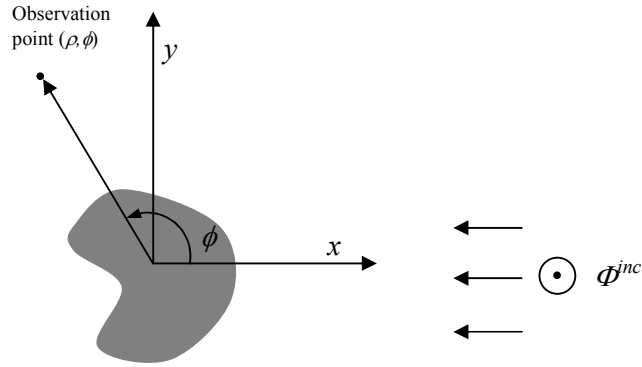


Fig 1.2. Two dimensional representation of the problem

$$\tilde{\Phi}^{sc}(\rho, \phi) = \sum_{v_m=-\infty}^{\infty} A_{v_m} H_{v_m}^{(2)}(k_0 \rho) e^{jv_m \phi} \quad (1.1)$$

where  $H_{v_m}^{(2)}$  is the Hankel function of the second kind of order  $v_m$ ,  $k_0$  is the wavenumber in free space,  $\rho, \phi$  are the radius and angle in polar coordinates where the field is calculated,  $j$  the imaginary unit and  $A_{v_m}$  is an amplitude term for each order. The limit for  $v_m$  is theoretically infinity. For numerical computation this is truncated to maximum value of  $0.5k_0 d$  [2 p. 511] where  $d$  is the largest dimension of the cross-section of the cylindrical structure. This means that larger structures require higher values of  $v_m$  and thus higher order of cylindrical harmonics. In this work electrically

small structures were considered, and in all cases  $-N \leq v_m \leq N$ , where  $N = 15$  was used, which was sufficient for accurate results.

### 1.2.2 Maxwell equations and wave equations

In this work the study domain is assumed lossless, isotropic and charge free. Thus the Maxwell equations [10] in differential form in the frequency domain can be expressed as

$$\nabla \times \tilde{\mathbf{E}} = -j\omega\mu_r\mu_0\tilde{\mathbf{H}} \quad (1.2)$$

$$\nabla \times \tilde{\mathbf{H}} = j\omega\epsilon_r\epsilon_0\tilde{\mathbf{E}} \quad (1.3)$$

$$\nabla \cdot \tilde{\mathbf{E}} = 0 \quad (1.4)$$

$$\nabla \cdot \tilde{\mathbf{H}} = 0 \quad (1.5)$$

where ‘ $\sim$ ’ denotes that the variable is in the frequency domain,  $\tilde{\mathbf{E}}$ ,  $\tilde{\mathbf{H}}$  are the electric and the magnetic field intensities respectively,  $\omega$  the angular frequency,  $\epsilon_r$ ,  $\mu_r$  are the relative permittivity and permeability respectively and  $\epsilon_0$ ,  $\mu_0$  the permittivity and permeability of free space.

From (1.2)-(1.5) by eliminating either  $\tilde{\mathbf{E}}$  or  $\tilde{\mathbf{H}}$  one obtains the vector wave equations. These can be expressed as [2 p.8]

$$\nabla \times \left( \frac{1}{\mu_r\mu_0} \nabla \times \tilde{\mathbf{E}} \right) - \omega^2\epsilon_r\epsilon_0\tilde{\mathbf{E}} = 0 \quad (1.6)$$

and

$$\nabla \times \left( \frac{1}{\epsilon_r\epsilon_0} \nabla \times \tilde{\mathbf{H}} \right) - \omega^2\mu_r\mu_0\tilde{\mathbf{H}} = 0 \quad (1.7)$$

These can be further simplified to scalar wave equations. These will be [2 p.9]

$$\nabla \cdot \frac{1}{\mu_r} \nabla \tilde{E}_z + k_0^2\epsilon_r\tilde{E}_z = 0 \quad (1.8)$$

and

$$\nabla \cdot \frac{1}{\epsilon_r} \nabla \tilde{H}_z + k_0^2 \mu_r \tilde{H}_z = 0 \quad (1.9)$$

In concise form (1.8) and (1.9) can be written as

$$\nabla \cdot \frac{1}{p_r} \nabla \tilde{\Phi} + k_0^2 q_r \tilde{\Phi} = 0 \quad (1.10)$$

where  $p_r = \mu_r$ ,  $q_r = \epsilon_r$ ,  $\tilde{\Phi} = \tilde{E}_z$  for TE polarisation and  $p_r = \epsilon_r$ ,  $q_r = \mu_r$ ,  $\tilde{\Phi} = \tilde{H}_z$  for TM polarisation. Equation (1.10) will be the starting point for the derived formulations in this work. The time-harmonic field components will be related to their frequency domain equivalents with [10]

$$\mathbf{E} = \text{Re}[\tilde{\mathbf{E}} \cdot e^{j\omega t}] \quad (1.11)$$

$$\mathbf{H} = \text{Re}[\tilde{\mathbf{H}} \cdot e^{j\omega t}] \quad (1.12)$$

### 1.2.3 Radar cross section

Radar cross section (RCS) is a very useful far-field parameter for describing the scattering properties of a target and has many practical applications [10,12,13]. The RCS is defined as *“the area intercepting that amount of power which, when scattered isotropically, produces at the receiver a density which is equal to that scattered by the actual target”* [10,13]. For two dimensional targets it is also referred as scattering width [10 p. 577]. The interest in this work is in the bistatic radar cross section or bistatic scattering width (BSW) which refers to the case when the incidence is in one angle and the scattered field is studied over a range of angles, in contrast to the monostatic where the transmitter and the receiver are in the same location [13 p. 98].

For the two dimensional case the RCS ( $\sigma_{2-D}$ ) is given by [10 p. 577]

$$\sigma_{2-D} = \lim_{\rho \rightarrow \infty} \left[ 2\pi\rho \frac{|\tilde{\Phi}_z^{sc}|^2}{|\tilde{\Phi}_z^{inc}|^2} \right] \quad (1.13)$$

where  $\rho$  is the distance from target to observation point,  $\tilde{\Phi}_z^{sc}$  is the component of the scattered electric or magnetic field and  $\tilde{\Phi}_z^{inc}$  of the incident depending on polarisation. The unit for  $\sigma_{2-D}$  is length (meters). The total field  $\tilde{\Phi}_z^t$  is the sum of the scattered field plus the incident one

$$\tilde{\Phi}_z^t = \tilde{\Phi}_z^{sc} + \tilde{\Phi}_z^{inc} \quad (1.14)$$

Equation (1.13) can be expressed in a form more helpful for the simulation approach. The scattered field for either the electric or magnetic field for the two dimensional case has the pattern described by (1.1). The large argument approximation for the Hankel function of the second kind is [10 p. 606]

$$H_n^{(2)}(k_0\rho) \approx \sqrt{\frac{2j}{\pi k_0\rho}} j^n e^{-jk_0\rho} \quad (1.15)$$

By replacing (1.15) to (1.1) the latter becomes

$$\lim_{\rho \rightarrow \infty} [\tilde{\Phi}^{sc}(\rho, \phi)] = \sum_{n=-\infty}^{\infty} A_n \sqrt{\frac{2j}{\pi k_0\rho}} j^n e^{-jk_0\rho} e^{jn\phi} \quad (1.16)$$

$$\lim_{\rho \rightarrow \infty} [\tilde{\Phi}^{sc}(\rho, \phi)] = \sqrt{\frac{2j}{\pi k_0\rho}} e^{-jk_0\rho} \sum_{n=-\infty}^{\infty} A_n j^n e^{jn\phi} \quad (1.17)$$

The amplitude squared will be:

$$\lim_{\rho \rightarrow \infty} [|\tilde{\Phi}^{sc}(\rho, \phi)|^2] = \left| \sqrt{\frac{2}{\pi k_0\rho}} \sum_{n=-\infty}^{\infty} A_n j^n e^{jn\phi} \right|^2 \quad (1.18)$$

So the bistatic scattering width will be:



$$\sigma_{2-D}(\phi) = \lim_{\rho \rightarrow \infty} \left[ 2\pi\rho_a \frac{2}{\pi k_0 \rho} \frac{\left| \sum_{n=-\infty}^{\infty} A_n j^n e^{jn\phi} \right|^2}{\left| \tilde{\Phi}_z^{inc} \right|^2} \right] \quad (1.19)$$

$$\sigma_{2-D}(\phi) = \frac{2\lambda}{\pi} \frac{\left| \sum_{n=-\infty}^{\infty} A_n j^n e^{jn\phi} \right|^2}{\left| \tilde{\Phi}_z^{inc} \right|^2} \quad (1.20)$$

Since the parameters  $A_n$  are found in order to calculate the RCS, one can also calculate the scattered field based on (1.1) at any given point as well.

### 1.3 Finite-element method

The FEM is a numerical method for the solution of boundary-value problems [2 p. 19, 14 p.87]. The problem to be solved consists of a governing differential equation and the boundary conditions. The differential equations of (1.6)-(1.10) can be expressed with the general form

$$\Lambda\Phi = 0 \quad (1.21)$$

where  $\Lambda$  is the differential operator in (1.6)-(1.10) and  $\Phi$  the unknown. In this work  $\Phi$  is the scattered or total electric or magnetic field. Equation (1.21) is defined in the studied domain  $\Omega$  which is truncated by the outer boundary  $\Gamma$ . In the problems considered here the outer boundary  $\Gamma$  is either a circle or a circular arc for the periodic approach. For the case of a circular outer boundary, the domain  $\Omega$  and the boundary  $\Gamma$  based on Fig. 1.2 are depicted in Fig. 1.3.

In most practical applications (1.21) does not have an analytical solution and thus an approximate one  $\Phi_{app}$  needs to be found. For this, there have been developed traditionally two methods the Ritz method and the Galerkin weighted residual method

[2 p.20]. Here the Galerkin weighted residual method is used. In the Galerkin method the residual which will appear if  $\Phi_{app}$  is substituted in (1.21) will be

$$r = \Lambda \Phi_{app} \neq 0 \quad (1.22)$$

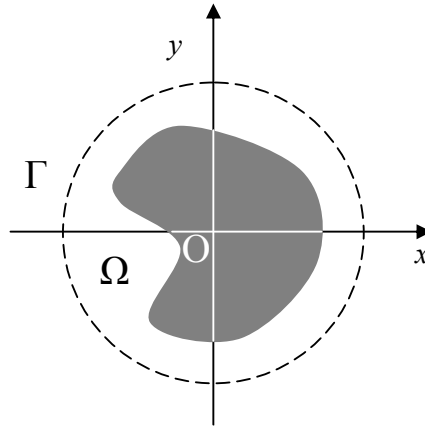


Fig. 1.3 Depiction of the domain  $\Omega$  and the boundary  $\Gamma$

In the weighted residual methods  $\Phi_{app}$  is obtained by multiplying the error  $r$  by the weighting function  $W$ , integrating over the domain  $\Omega$  and setting the weighted residual error  $R$  equal to zero.

$$R = \int_{\Omega} W r d\Omega = 0 \quad (1.23)$$

in the Galerkin method the same functions that are used for the weighting functions are also the basis functions that are used for the representation of the approximate solution  $\Phi_{app}$  [2 p.22]. The implementation of the FEM method can be separated to four steps [2 p. 31, 14 p.87]. These are

- Discretisation of domain
- Elemental approximation with interpolation functions
- Assembly of the system of equations
- Solution of the system of equations

To these the following can also be added

- Post-processing of the matrix solution

In the cases considered in this work, post-processing includes obtaining the BSW from the field values and plotting it.

### **1.3.1 Discretisation of domain**

The first step of the FEM is the discretisation of the domain  $\Omega$  to the subdomains, the elements. There is a wide range of elements for 2D structures but in this work 8-noded quadrilateral curvilinear elements [1,2] were used for the domain and 3-noded curvilinear line elements for the boundary [15]. These are considered in Chapter 2. The important thing is that their sides can be curved and thus they can effectively model circular boundaries. [2 p.156]. The 8-noded quadrilateral curvilinear elements are widely used curvilinear elements [1] and have been applied in the past to 2D cylindrical problems [11, 16]. The number of elements should be large enough in order to achieve accuracy but not unnecessarily large because that would be a computational burden. In the simulations of this dissertation there are always more than 6 elements per wavelength.

In this work the discretisation of the domain was performed in all cases with the FEMGEN mesh generator. An example of a mesh is depicted in Fig. 1.4. This is the cross-section of a square dielectric cylinder surrounded by free space. It has 1061 nodes and 340 elements in total. One can notice how accurately the boundary elements follow the circular curvature.

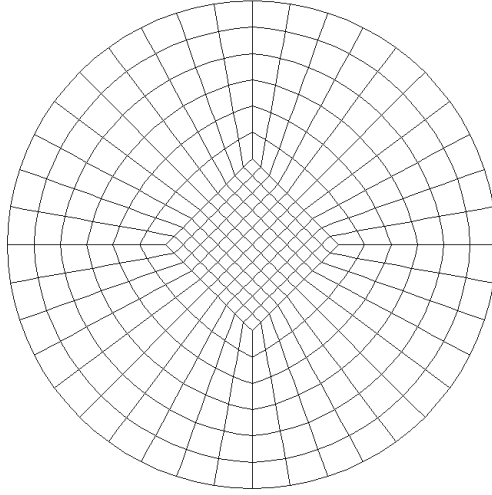


Fig. 1.4 Example of a mesh of square scatterer

### 1.3.2 Elemental approximation with interpolation functions

The next step is the choice of the basis functions. The field in an element can be expressed as

$$\Phi_{app}^e = \sum_i N_i^e \Phi_i^e \quad (1.24)$$

where  $N_i$  are the interpolation or basis functions. The highest order of the interpolation function  $N_i$  is considered the order of the element [2 p.33]. The order of 8-noded quadrilateral curvilinear elements is 3.

An important point is that in the Galerkin weighted residual method the interpolation functions are the same as the weighting function, thus

$$W_i = N_i \quad (1.25)$$

### 1.3.3 Assembly of the system of equations

The third step is the assembly of the system of equations. This is performed by deriving the FEM formulation based on (1.23), by applying the vector identity of [17]

$$\nabla \cdot (U\mathbf{A}) = U\nabla \cdot \mathbf{A} + \mathbf{A} \cdot \nabla U \quad (1.26)$$

and the divergence theorem to it. Thus (1.23) becomes

$$R = \int_{\Omega} \nabla W \nabla \Phi_{app} d\Omega - \int_{\Gamma} W \frac{\partial \Phi_{app}}{\partial \rho} d\Gamma = 0 \quad (1.27)$$

This procedure will become clear throughout this work. The MNRBC is based on an expression of the boundary integral of (1.27) with the cylindrical harmonics of (1.1). At this point what should be mentioned is that, after an appropriate mathematical derivation, (1.27) yields to a matrix form such as

$$[\mathbf{K}] \{\Phi_{app}\} = \{\mathbf{b}\} \quad (1.28)$$

where  $[\mathbf{K}]$  is  $N \times N$  square matrix and  $\{\mathbf{b}\}$  a  $N \times 1$  matrix vector and  $N$  the total number of nodes in the domain. The FEFD formulations result to a system such as (1.28) directly from (1.27), and is solved once for each frequency studied. FETD requires time discretisation which is performed with Newmark-beta which is a second-order accurate discretisation scheme [2 pp.534-535] . Then the system results in a form such as (1.28), and is solved for each timestep.

### 1.3.4 Solution of the system of equations

The next step is the solution of (1.28). The matrix  $[\mathbf{K}]$  has many zero entries, and this can be used by the matrix solver to achieve efficiency. In this work the ME28 solver from the Harwell library was used for the complex global matrix and the MA28 for the real case. For the calculation of the Bessel and Hankel functions needed in this work, the ZBESH subroutine from Netlib Repository was used.

For the assembly and the solution of the system of equations, FORTRAN 95 was used. The computer used for the numerical results in this work was a desktop one with a 2.8GHz processor and 1.5GB of Random-access memory (RAM). The

computing times presented in this work can be improved with the application of more optimized FORTRAN codes.

### **1.3.5 Post-processing**

The last part of the FEM simulation is the post-processing in order to extract from the field values the BSW. This is performed with Matlab which is also used for the creation of all the plots in this thesis.

## **1.4 Frequency and time domain considerations**

In this dissertation the formulations and the work are held for both the frequency and time domain. The results are shown in terms of BSW. This is a representation at a specific frequency. This means that the FEFD is applied at this specific frequency which in this work was chosen  $f_c=0.3\text{GHz}$  (wavelength  $\lambda=1\text{m}$ ) following the choice of [12] for similar problems. The resulting field from the finite element simulation is post-processed in order to calculate the BSW. For the FETD the procedure is different. The field calculated is in the time domain and Fourier transform is applied to it by using the iterative algorithm of [18] and normalized with the amplitude of the incident field as will be shown in Chapter 2. Then, the same post-processing procedure as in FEFD is applied to it, and the BSW is calculated.

One important point in the transition between frequency and time domain is whether the Fourier Transform (FT) or the Laplace Transform (LT) is applied. Either of these transformations can be used and they can be treated as equivalent by replacing  $s = j\omega$ , only if the transform function in the Laplace domain has no poles in the right half of the s-plane [19]. In other words the system should be stable [19].

The transition from the Laplace domain to the time domain of the functions needed in this work is performed either analytically or with Vector-Fitting (VF) [20].

Vector Fitting approximates a known frequency response  $F(s)$  as [20]:

$$F(s) \approx F_{app}(s) = \sum_{m=1}^M \frac{r_m}{s - a_m} + h + ds \quad (1.29)$$

where  $M$  is the number of poles used,  $r_m$ ,  $a_m$  are the pole coefficients (or residues) and pole locations respectively and are either real or conjugate pairs,  $h$ ,  $d$  are the steady and proportional terms. The subscript ‘*app*’ indicates an approximation. Vector Fitting gives the choice of using unstable poles or not, and, for the FEM simulations, the approximations using only stable poles were in all cases accurate and successful. The use of an unstable pole means exponential growth, and this would be catastrophic for a time domain scheme. For these reasons the replacement of  $s = j\omega$  can be used.

## 1.5 Potential engineering applications

This chapter closes with a short presentation of potential applications of cylindrical structures where generally the formulations derived in this work can be useful. Specific contributions and extensions are considered in each chapter. This section as this chapter in whole connects the specific focus of this work with the general physical knowledge and engineering practice.

Antenna systems include cylindrical objects such as struts and masts that support them. These objects interfere with the signal and thus it would be beneficial to know their effect on communications.

Pyramidal RF/microwave absorbers are usually used to cover planar metallic surfaces. However, sometimes are employed to cover cylindrical structures. Thus it

would be beneficial to know how effective these absorbers are when they are used over cylindrical surfaces. This example is depicted in Fig.1.5.

Another application for cylinders is for metamaterial structures and cloaking devices [21, 22, 23]. Calculation and study of the RCS and scattering properties is of extreme interest for these applications. Cylindrical ferrite posts have very useful applications in microwave engineering which include steering the electromagnetic field, changing the coupling and changing the filtering frequency [24].

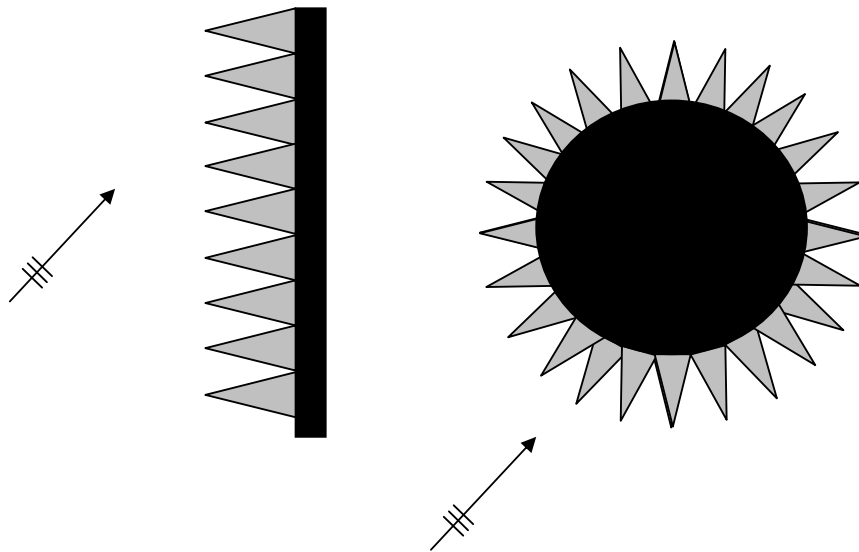


Fig. 1.5 Planar and cylindrical RF/microwave absorbers

Cylindrical antennas [25] and conformal antennas [14] of cylindrical shape are widely used in engineering practice. These applications are based on their aerodynamic shape e.g. for aircraft use and their potential for 360 degree coverage [14 p. 2]. Cylindrical microstrips are also an important area of research as they have all the advantages of their planar equivalents with the addition of being able to conform to the structures in which they are mounted [26]. The work performed here is a natural first step and a valuable background for the study of cylindrical arrays.



## REFERENCES

- [1] P.P. Silvester, and R.L. Ferrari, *Finite elements for electrical engineers*, 3rd ed., Cambridge University Press, Cambridge, 1996.
- [2] J. M. Jin, *The Finite Element Method in Electromagnetics*, 2nd ed., Wiley-IEEE Press, New York, 2002.
- [3] Y. Zhu, A. Cangellaris, *Multigrid Finite Element Methods for Electromagnetic Field Modeling*, John Wiley & Sons, 2006.
- [4] J.L. Volakis, A. Chatterjee, L.C. Kempel, *Finite Element Method for Electromagnetics, Antennas, Microwave circuits and scattering applications*, IEEE press, 1998.
- [5] E.K. Miller, "Time-domain modeling in electromagnetics", *Journal of electromagnetic Waves and Applications*, vol.8, no. 9/10, pp.1125-1172,1994.
- [6] F.L. Teixeira, "Time-Domain Finite-Difference and Finite-Element Methods for Maxwell Equations in Complex Media", *IEEE Trans. Antennas Propag.* vol. 56, no8, pp.2150-2166, Aug. 2008.
- [7] A. Taflov, S. C. Hagness, *Computational Electrodynamics: The Finite-Difference-Time Domain Method*, 2nd ed., Boston, London, Artech House, 2000.
- [8] T. Cwik, "Coupling into and Scattering from Cylindrical Structures Covered Periodically with Metallic Patches", *IEEE Trans. Antennas Propag.* vol. 38, no. 2, pp.220-226, Feb. 1990.
- [9] T. Cwik, "Scattering from general periodic screens," Ph.D. dissertation, Univ. Illinois, Urbana, 1986.
- [10] C.A. Balanis, *Advanced Engineering Electromagnetics*, John Wiley & Sons, 1989.

- [11] A. Freni, “On plane-wave scattering from an azimuthally periodic cylindrical structure”, *Microwave and Optical Technology Letters*, vol. 25, no. 4, pp. 255-257, 2000.
- [12] K. Umashankar, A. Taflove, *Computational Electromagnetics*, Artech House, 1993.
- [13] C.A. Balanis, *Antenna Theory, Analysis and Design*, 3<sup>rd</sup> edition, John Wiley & Sons, 2005.
- [14] L. Josefsson, P. Persson, *Conformal array antenna theory and design*, Wiley-Interscience, 2006.
- [15] G. Dhatt, G. Touzot, *The Finite Element Method Displayed*, John Wiley & Sons, 1984.
- [16] S.-K. Jeng, and C.-H. Chen, “On Variational Electromagnetics: Theory and Application”, *IEEE Transactions on Antennas and Propagation*, vol. 32, no. 9, pp. 902-907, 1984.
- [17] F. T. Ulaby, *Fundamentals of applied electromagnetics*, Media ed., Pearson Prentice Hall, 2004.
- [18] D. M. Sullivan, *Electromagnetic Simulations Using the FDTD method*, Wiley-IEEE Press, 2000.
- [19] M.L. Meade and C.R. Dillon, *Signals and Systems Models and Behaviour*, 2<sup>nd</sup> ed. Kluwer Academic Publishers, 2000.
- [20] B. Gustavsen, and A. Semlyen, “Rational Approximation of Frequency Domain Responses by Vector Fitting”, *IEEE Trans. on Power Delivery*, vol. 14, no. 3, pp. 1052-1061, 1999.
- [21] A. Alu, N. Engheta, “Achieving transparency with plasmonic and metamaterial coatings”, *Phys. Rev.*, E 72, 016623, 2005.

- [22] A. Alu, M.G. Silveirinha, A. Salandrino, N. Engheta, “Epsilon-near-zero metamaterials and electromagnetic sources: Tailoring the radiation phase pattern”, *Phys. Rev.*, B 75, 0155410, 2007.
- [23] B. Edwards, A. Alu, M.G. Silveirinha, N. Engheta, “Experimental Verification of Plasmonic cloaking at Microwave Frequencies with metamaterials”, *Phys. Rev. Letters*, 0153901, 2009.
- [24] W.B. Dou and E.K.N. Yung, “Scattering properties of cylindrical ferrite posts and their applications”, *International Journal of Infrared Waves*, vol.21, no.6, 2000.
- [25] R. W. P. King, G. J. Fikioris, R. B. Mack, *Cylindrical antennas and arrays*, Cambridge University Press, 2002.
- [26] C.A. Valagiannopoulos, “Semi-analytic solution to a cylindrical microstrip with inhomogeneous substrate”, *Electromagnetics*, vol. 27, no. 8, pp. 527-544, November 2007.

## CHAPTER 2

### Scattered field FETD-MNRBC formulation

#### 2.1 Introduction

After some important concepts of the Finite Element Method (FEM) and cylindrical structures were presented in the previous chapter, this one starts the realisation of these concepts into FEM simulations. Here for the first time a two dimensional FETD formulation of a Vector Fitting (VF) approximated cylindrical, nonlocal modal non-reflective boundary condition (MNRBC) is derived and applied in a two dimensional formulation of plane wave scattering from perfectly electrically conducting (PEC) cylinders.

This boundary condition is based on the fact that the scattered field around the simulated cylindrical scatterer can be expressed as summation of modal functions, which are products of Hankel functions of the second kind and azimuthal function terms as described in (1.1). These modal functions are found from the solution of the Helmholtz equation in cylindrical coordinates as proven in Appendix A.

In this chapter, a transverse electric (TE) polarized incident plane wave is considered and a scattered field formulation is employed to model electromagnetic plane wave scattering from perfectly electrically conducting cylinders of arbitrary cross-section. Moreover, as in all cases in this thesis, the region surrounding the cylinder is assumed to be free space. The presentation of the formulations begins with the scattered field formulations since this is simpler, compared to the ones presented in the next chapters.

Several methods have been proposed for the truncation of the Finite-Element meshes in the time domain [1-3]. Moreover, the application of the modal (eigenfunction expansion) non-reflecting boundary condition (MNRBC) in the Finite Element Frequency Domain (FEFD) method was considered [4-8], but it has not been applied to the Finite Element Time Domain (FETD) method.

The eigenfunction (modal) expansion technique can be combined with the finite element method [4]. Furthermore, modal boundary conditions have been applied for FETD formulations in Cartesian coordinates, including periodic or waveguide problems [9,10]. Here for the first time the modal non-reflective boundary condition, in cylindrical coordinates is derived and applied in two dimensional FETD simulations, resulting in original formulations and numerical results.

The FETD-MNRBC realisation requires the knowledge of a convolution kernel. The exact values of this kernel are not known, and the available partial fraction approximations such as [11] are mathematically complex, and only a few cylinder kernels are available [11]. The application of the VF method [12] is an elegant and accurate way to approximate these kernels as a sum of partial fractions [13]. The accuracy of the VF approximation will be thoroughly presented in the next chapter, but in this chapter the results of this approximation will be used. This is done in order to ensure continuity in the presentation of the FEFD-MNRBC and FETD-MNRBC approaches. Furthermore it allows elaborating more on the approximation procedure in the next chapter and examining the parameters that affect it.

A very important advantage of expressing the boundary kernel as a sum of partial fractions is that the convolution integral that appears in the FETD formulation does not have to be computed in a standard way as in [9], but can be calculated recursively as introduced in [14], which is more time efficient.

This chapter begins with the presentation of the basic concepts of scattered field formulation. It continues with the presentation of the weighted residual FEFD formulation, in terms of the scattered transverse electric field component. Following that, the first order absorbing boundary condition [4, 15 p.121] is shortly presented and then the MNRBC is derived. The geometric discretisation using third order isoparametric surface (8-noded) [16] and line (3-noded) elements [17] is subsequently presented. In addition, the time discretisation of the FETD formulation and the details of the recursive convolution implementation of the MNRBC are presented. The next part presents numerical results of the proposed FETD formulation which are compared with analytical results, frequency domain results and with results that appeared in the literature. Three PEC cylindrical cross-sections are considered: a circular, a triangular and a square. The last section concludes the work presented in this chapter and discusses the advantages and disadvantages of the approach implemented.

## 2.2 Scattered field concept

Finite element formulations can be derived not only for the total field but for the scattered field as well [15,18]. This is advantageous for cases such as the one analysed in this chapter, where the resulting formulations are easier than the total field equivalents. In this chapter it is assumed that the simulated structure is a PEC cylindrical scatterer surrounded by free space.

The Helmholtz equation in the lossless region surrounding the cylinder, for the transverse electric (TE) polarization, in which the total electric field component  $\tilde{E}_z^t(x, y)$  is the unknown, is [4 p.8]

$$\nabla \cdot \frac{1}{\mu_r} \nabla \tilde{E}_z^{sc}(x, y) + k_0^2 \varepsilon_r \tilde{E}_z^{sc}(x, y) = 0 \quad (2.1)$$

The ‘ $\sim$ ’ denotes that the variable is in frequency domain. The parameters  $\mu_r, \varepsilon_r, k_0$  refer to the relative permeability, the relative permittivity and the wavenumber in free space respectively. Since the structure is surrounded by free space,  $\mu_r = \varepsilon_r = 1$ , thus (2.1) reduces to

$$\nabla^2 \tilde{E}_z^t + k_0^2 \tilde{E}_z^t = 0 \quad (2.2)$$

As described before the total field  $\tilde{E}_z^t$  can be expressed as the sum of the scattered field  $\tilde{E}_z^{sc}$  plus the incident one  $\tilde{E}_z^{inc}$ .

$$\tilde{E}_z^t = \tilde{E}_z^{sc} + \tilde{E}_z^{inc} \quad (2.3)$$

By inserting (2.3) in (2.2) it becomes

$$\nabla^2 (\tilde{E}_z^{sc} + \tilde{E}_z^{inc}) + k_0^2 (\tilde{E}_z^{sc} + \tilde{E}_z^{inc}) = 0 \quad (2.4)$$

$$\nabla^2 \tilde{E}_z^{sc} + k_0^2 \tilde{E}_z^{sc} = -\nabla^2 \tilde{E}_z^{inc} - k_0^2 \tilde{E}_z^{inc} \quad (2.5)$$

The incident field satisfies by definition the Helmholtz equation in free space [18]

$$\nabla^2 \tilde{E}_z^{inc} + k_0^2 \tilde{E}_z^{inc} = 0 \quad (2.6)$$

Thus (2.5) reduces to

$$\nabla^2 \tilde{E}_z^{sc} + k_0^2 \tilde{E}_z^{sc} = 0 \quad (2.7)$$

Equation (2.7) will be the basis for the formulations derived next in this chapter. The next interesting point is the introduction of the incident field. Since the scatterer is assumed to be a PEC one, the total field on its surface will be zero and thus from (2.3) the scattered field will be “minus the incident field”. This way, by assigning the points on the PEC surface with values equal to “minus the incident field”, the incident field is applied.

### 2.3 FEFD formulation

The weighted residual formulation of (2.2) is:

$$R = \iint_{\Omega} W \left( \nabla^2 \tilde{E}_z^{sc} + k_0^2 \tilde{E}_z^{sc} \right) d\Omega = 0 \quad (2.8)$$

where  $W$  is the weighting function.

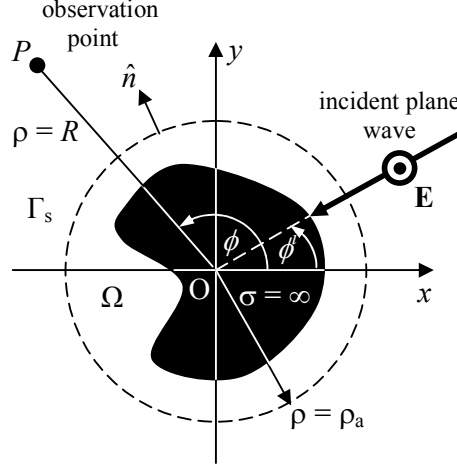


Fig. 2.1. TE polarized plane wave scattering from a PEC cylinder of arbitrary cross-section.

After applying the vector identity [19]

$$\nabla \cdot (U\mathbf{A}) = U\nabla \cdot \mathbf{A} + \mathbf{A} \cdot \nabla U \quad (2.9)$$

to the weighted residual formulation of the Helmholtz equation (2.8) followed by the divergence theorem, equation (2.8) becomes:

$$R = \iint_{\Omega} \left[ (\nabla W \cdot \nabla \tilde{E}_z^{sc}) - k_0^2 W \tilde{E}_z^{sc} \right] d\Omega - \oint_{\Gamma_s} W \nabla \tilde{E}_z^{sc} \cdot \hat{n} d\Gamma = 0 \quad (2.10)$$

where  $\hat{n}$  is the outward unit normal vector to the circular contour  $\Gamma_s$  of radius  $\rho_a$  which encloses the simulated area  $\Omega$  (see Fig.2.1).

Since

$$\nabla \tilde{E}_z^{sc} \cdot \hat{n} = \frac{\partial \tilde{E}_z^{sc}}{\partial n} = \frac{\partial \tilde{E}_z^{sc}}{\partial \rho} \quad (2.11)$$



equation (2.10) becomes:

$$R = \iint_{\Omega} \left( \frac{\partial W}{\partial x} \frac{\partial \tilde{E}_z^{sc}}{\partial x} + \frac{\partial W}{\partial y} \frac{\partial \tilde{E}_z^{sc}}{\partial y} - k_0^2 W \tilde{E}_z^{sc} \right) d\Omega - \oint_{\Gamma_s} W \frac{\partial \tilde{E}_z^{sc}}{\partial \rho} d\Gamma = 0 \quad (2.12)$$

Assuming incidence along the  $-x$  direction, thus  $\phi^i = 0$  as depicted in Fig.2.1, the transverse electric field component of the incident wave, is given by:

$$\tilde{E}_z^{inc}(x) = E_o e^{jk_0 x} \quad (2.13)$$

On the surface of the PEC cylinder the scattered electric field is

$$\tilde{E}_z^{sc} \Big|_{PEC} = -\tilde{E}_z^{inc} \Big|_{PEC} = -E_o e^{jk_0 x} \text{ since } \tilde{E}_z^{tot} = 0 \quad (2.14)$$

which is an inhomogeneous Dirichlet boundary condition and  $\tilde{E}_z^{tot}$  and  $\tilde{E}_z^{inc}$  refer to the total and the incident transverse electric field components respectively.

## 2.4 Application of truncation boundary conditions

The next step of the formulation is the application of the truncation boundary condition. The scope of the truncation boundary conditions is to simulate the propagation of the scattered field to infinity, despite the fact that a mesh of specific dimensions is used. The application of the boundary conditions considered in this work requires the re-expression of the boundary integral term of (2.12) by analysing the field derivative of this integral.

### 2.4.1 First order absorbing boundary condition

At this point the first order absorbing boundary condition will be presented [4, 15], which is also called the first order radiation boundary condition [4]. This is a simple and well studied absorbing boundary condition and is presented for demonstration purposes. Therefore only the basic equation will be shown here. The

way the first order absorbing boundary condition can be derived from the cylindrical scattered field decomposition is described in Appendix B. The first order boundary condition is based on the asymptotic form of the scattered or radiated field in the far zone [4]. Using the first order boundary condition the field derivative of (2.12) can be expressed as

$$\frac{\partial \tilde{E}_z^{sc}}{\partial \rho} = \left( -\frac{1}{2\rho} - jk_0 \right) \tilde{E}_z^{sc} \quad (2.15)$$

This relation can be easily incorporated into the FEFD algorithm [4].

#### 2.4.2 Modal nonreflecting boundary condition

The application of MNRBC in FEFD has been considered [4-8]. Here it is presented for reasons of completeness and because it introduces useful concepts for the FETD formulation. To apply the MNRBC, the boundary integral of (2.12) will be re-expressed in terms of modal functions, which are the cylindrical harmonics of (1.1). Equation (1.1) will be used for the field derivative appearing in the boundary integral of (2.12). The summation of (1.1) will be appropriately truncated, as discussed before. Following the decomposition of [20 p.604], the scattered field from a cylindrical scatterer at the outer boundary,  $\Gamma_s$ , can be written as

$$\tilde{E}_z^{sc}(x, y) \Big|_{\rho=\rho_a} = \tilde{E}_z^{sc}(\rho_a, \phi) = \sum_{m=-\infty}^{\infty} A_m H_m^{(2)}(k_0 \rho_a) e^{jm\phi} \quad (2.16)$$

And it will be

$$\tilde{E}_z^{sc}(\rho_a, \phi) e^{-jn\phi} = \sum_{m=-\infty}^{\infty} A_m H_m^{(2)}(k_0 \rho_a) e^{jm\phi} e^{-jn\phi} \quad (2.17)$$

$$\int_0^{2\pi} \tilde{E}_z^{sc}(\rho_a, \phi) e^{-jn\phi} d\phi = \int_0^{2\pi} \sum_{m=-\infty}^{\infty} A_m H_m^{(2)}(k_0 \rho_a) e^{jm\phi} e^{-jn\phi} d\phi \quad (2.18)$$

$$\int_0^{2\pi} \tilde{E}_z^{sc}(\rho_a, \phi) e^{-jn\phi} d\phi = A_n H_n^{(2)}(k_0 \rho_a) \int_0^{2\pi} e^{jm\phi} e^{-jn\phi} d\phi \quad (2.19)$$

From orthogonality relations of the azimuthal exponential function, it follows that

$$A_n = \frac{\oint_{\Gamma_s} \tilde{E}_z^{sc}(\rho_a, \phi) e^{-jn\phi} d\Gamma}{2\pi \rho_a H_n^{(2)}(k_0 \rho_a)} \quad (2.20)$$

where use of the fact that  $d\Gamma = \rho_a d\phi$  was made. Note that:  $\oint_{\Gamma_s} \dots d\Gamma = \int_0^{2\pi} \dots \rho_a d\phi$ . The

boundary condition to be used in (2.12) is obtained by differentiating both sides of (2.16) with respect to  $\rho$ .

$$\left. \frac{\partial E_z^{sc}(\rho, \phi)}{\partial \rho} \right|_{\rho=\rho_a} = \sum_{n=-\infty}^{\infty} A_n \left( \frac{\partial H_n^{(2)}(k_0 \rho)}{\partial \rho} \right) e^{jn\phi} \Big|_{\rho=\rho_a} \quad (2.21)$$

Using (2.20) and (2.21) the boundary integral in (2.12) can be expressed as follows:

$$\begin{aligned} \oint_{\Gamma_s} W \left. \frac{\partial \tilde{E}_z^{sc}(\rho, \phi)}{\partial \rho} \right|_{\rho=\rho_a} d\Gamma = \\ \oint_{\Gamma_s} W \sum_{n=-\infty}^{\infty} \left[ \frac{\oint_{\Gamma_s} \tilde{E}_z^{sc}(\rho_a, \phi) e^{-jn\phi} d\Gamma}{2\pi \rho_a H_n^{(2)}(k_0 \rho_a)} \right] \left. \frac{\partial H_n^{(2)}(k_0 \rho)}{\partial \rho} \right|_{\rho=\rho_a} e^{jn\phi} d\Gamma = \\ \sum_{n=-\infty}^{\infty} G_n(\omega) \oint_{\Gamma_s} W e^{jn\phi} d\Gamma \oint_{\Gamma_s} \tilde{E}_z^{sc}(\rho_a, \phi) e^{-jn\phi} d\Gamma \end{aligned} \quad (2.22)$$

where  $G_n$  is given by

$$G_n(\omega) = \frac{1}{2\pi \rho_a} \frac{\left. \frac{\partial H_n^{(2)}(k_0 \rho)}{\partial \rho} \right|_{\rho=\rho_a}}{H_n^{(2)}(k_0 \rho_a)} \quad (2.23)$$

which becomes, through the use of derivative identities of the Hankel functions [20],

$$G_n(\omega) = \frac{-k_0}{2\pi \rho_a} \frac{H_{n+1}^{(2)}(k_0 \rho_a)}{H_n^{(2)}(k_0 \rho_a)} + \frac{n}{2\pi \rho_a^2} \quad (2.24)$$

This  $G_n$  function is the frequency response of the boundary kernel which will be analyzed in Chapter 3. The application of the FETD-MNRBC will be based on this

kernel.

## 2.5 Geometric Discretisation of the FEFD formulation in terms of isoparametric elements

The finite element region  $\Omega$  is meshed with 8-noded isoparametric curvilinear quadrilateral elements. Within an element, the following transformation holds between the global Cartesian coordinates  $x, y$  and the local coordinates  $u, v$  [16 p.285]

$$x(u, v) = \sum_{i=1}^8 N_i^e(u, v) x_i, \quad y(u, v) = \sum_{i=1}^8 N_i^e(u, v) y_i \quad (2.25)$$

This transformation between an actual and a transformed element is depicted in Fig. 2.2(a). The basis functions  $N^e$  are given in [16 p.286] and are

$$N_1(u, v) = \frac{1}{4}(u+1)(v+1)(u+v-1) \quad (2.26a)$$

$$N_2(u, v) = \frac{1}{2}(u+1)(v+1)(-u+1) \quad (2.26b)$$

$$N_3(u, v) = \frac{1}{4}(-u+1)(v+1)(-u+v-1) \quad (2.26c)$$

$$N_4(u, v) = \frac{1}{2}(-u+1)(v+1)(-u+1) \quad (2.26d)$$

$$N_5(u, v) = \frac{1}{4}(u-1)(-v+1)(u+v+1) \quad (2.26e)$$

$$N_6(u, v) = \frac{1}{2}(u+1)(-v+1)(-u+1) \quad (2.26f)$$

$$N_7(u, v) = \frac{1}{4}(u+1)(-v+1)(u-v-1) \quad (2.26e)$$

$$N_8(u, v) = \frac{1}{2}(u+1)(v+1)(-v+1) \quad (2.26f)$$

The superscript  $e$  denotes the  $e$ th element. Furthermore the unknown scattered field is approximated interpolatively within an element using the same basis functions as those in (2.25).

$$\tilde{E}_z^{sc,e}(x(u,v), y(u,v)) = \sum_{i=1}^8 N_i^e(u,v) \tilde{E}_{z,i}^{sc,e} \quad (2.27)$$

In the boundary integral computation along  $\Gamma_s$  one uses the side of the surface element that coincides with  $\Gamma_s$ . Thus, effectively, the integration is performed over a boundary mesh with 3-noded isoparametric curvilinear line elements (see Fig. 2.2 (b) ) having the following basis functions

$$\begin{aligned} N_1(u) &= -\frac{1}{2}u(-u+1) \\ N_2(u) &= (-u+1)(u+1) \\ N_3(u) &= \frac{1}{2}u(u+1) \end{aligned} \quad (2.28)$$

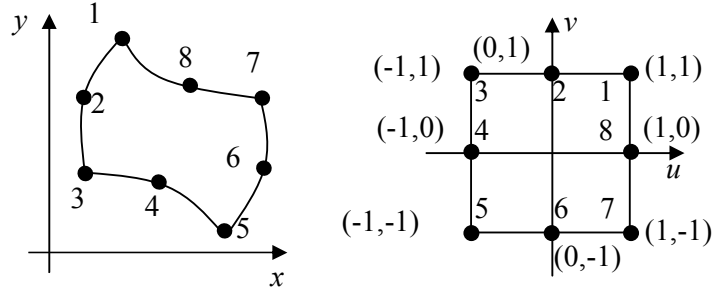
These functions result from (2.26) by setting in one side of the element  $v=1$ . Alternatively they can be found explicitly in [17 p.82]. Following the finite element geometric discretisation of the weighted residual formulation using the Galerkin procedure, (2.7) and (2.22) lead to the global matrix equation

$$\underbrace{[ [\mathbf{S}^\Omega] - k_0^2 [\mathbf{T}^\Omega] + [\mathbf{P}^\Gamma] ]}_{[\mathbf{M}^{\Omega,\Gamma}]} \{ \tilde{\mathbf{E}}_z^{sc} \} = \{ \mathbf{F} \} \quad (2.29)$$

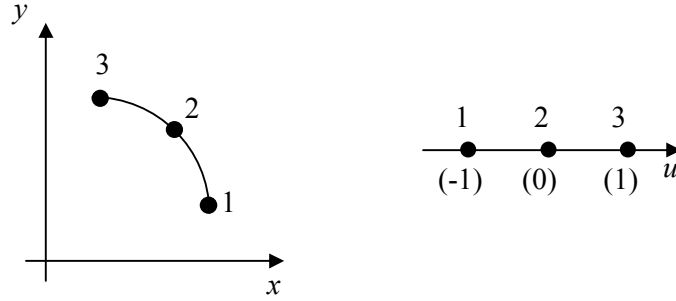
Or

$$[\mathbf{M}^{\Omega,\Gamma}] \{ \tilde{\mathbf{E}}_z^{sc} \} = \{ \mathbf{F} \} \quad (2.30)$$

where  $[...]$  and  $\{...\}$  denote a square matrix and a column vector respectively. Matrices  $[\mathbf{S}^\Omega]$ ,  $[\mathbf{T}^\Omega]$  are sparse and symmetric. Matrix  $[\mathbf{P}^\Gamma]$  is fully populated and it is symmetric. The superscripts  $\Omega$  and  $\Gamma$  indicate that the corresponding matrices are assembled from surface and boundary elemental matrix contributions. The entries of



(a)



(b)

Fig. 2.2. (a) The 8-noded curvilinear quadrilateral surface element and its square reference element. (b)

The 3-noded curvilinear line element and its linear reference element.

the surface elemental matrices that constitute  $[\mathbf{S}^\Omega]$  and  $[\mathbf{T}^\Omega]$  can be found in [16] and are described in Appendix C. From (2.22), the entries of the boundary elemental matrices, from which  $[\mathbf{P}^\Gamma]$  is assembled, are given by

$$P_{ij}^{kl,e} = - \sum_{n=-\infty}^{\infty} G_n(\omega) B_{n,i}^k C_{n,j}^l \quad (2.31)$$

where

$$\begin{aligned} B_{n,i}^k &= \int_{\Gamma^k} N_i^k(u) e^{jn\phi} d\Gamma = \int_{-1}^1 N_i^k(u) e^{jn\phi} J_s^k du \\ &= \int_{-1}^1 N_i^k(u) \exp \left[ jn \times \sin^{-1} \left( \frac{1}{\rho_a} \sum_{p=1}^3 N_p(u) y_p^k \right) \right] J_s^k du \end{aligned} \quad (2.32)$$

$$\begin{aligned}
C_{n,j}^l &= \int_{\Gamma^l} N_j^l(u) e^{-jn\phi} d\Gamma = \int_{-1}^1 N_j^l(u) e^{-jn\phi} J_s^l du \\
&= \int_{-1}^1 N_j^l(u) \exp \left[ -jn \times \sin^{-1} \left( \frac{1}{\rho_a} \sum_{p=1}^3 N_p(u) y_p^l \right) \right] J_s^l du
\end{aligned} \tag{2.33}$$

in which  $J_s^{k,l}$  can be calculated from [17 p.82]

$$\begin{aligned}
J_s^{k,l} &= \sqrt{\left( \frac{dx}{du} \right)^2 + \left( \frac{dy}{du} \right)^2} \\
&= \sqrt{\left( \sum_{p=1}^3 \frac{dN_p(u)}{du} x_p^{k,l} \right)^2 + \left( \sum_{p=1}^3 \frac{dN_p(u)}{du} y_p^{k,l} \right)^2}
\end{aligned} \tag{2.34}$$

The limits of the summation of (2.31) in this work are  $-N \leq n \leq N$ , where  $N=15$ . As discussed in the previous chapter these limits are related with the dimensions of the simulated structures. In (2.32) and (2.33),  $\Gamma^k$  and  $\Gamma^l$  are the boundary sections corresponding to the  $k$ th and  $l$ th boundary elements respectively. Element  $k$  may be different or the same as element  $l$ . Subscripts are used to indicate that the variables ( $P, B, C, N$ ) are associated with the element node number  $i$  (of the  $k$ th element) and/or element node number  $j$  (of the  $l$ th element). Following the evaluation of (2.31) for a given set of parameter values ( $k, l, n, i, j$ ) the result is inserted at the appropriate position in the global matrix that corresponds to the global node numbers of the element node numbers  $i$  and  $j$ .

In other words for a specific order  $n$ ,  $B$  (2.32) is calculated for the  $k$ th boundary element and  $C$  (2.33) is calculated for the  $l$ th boundary element. After that  $P$  is found from (2.31) and placed in the global matrix using indexes  $i,j$ . Next,  $C$  is calculated for the  $(l+1)$ th element and again  $P$  is found from (2.31) using the same value of  $B$  as before and placed in the global matrix. After this procedure is repeated for all values  $l$  of  $C$ , then  $B$  is calculated for  $(k+1)$  and the process starts over. After the procedure is completed for all values of  $k$ , then the next order  $n$  is approached the

same way. In this work the integrations of (2.32) and (2.33) are performed numerically using the 5-point Gaussian quadrature formula [16 pp. 290-291].

The global matrix  $[\mathbf{M}^{\Omega, \Gamma}]$  in (2.29) is initially assembled ignoring the inhomogeneous Dirichlet boundary condition (2.14). Thus initially  $\{\mathbf{F}\} = \{\mathbf{0}\}$ . Subsequently, this boundary condition is imposed following a procedure outlined in [4] by suitably modifying  $[\mathbf{M}^{\Omega, \Gamma}]$  and filling appropriate positions of  $\{\mathbf{F}\}$  with entries based on the incident field. The final form of the matrices after the 5-point Gaussian quadrature formula is applied is presented in Appendix C.

## 2.6 FETD-MNRBC Formulation

This section proceeds to the FETD-MNRBC formulation, which is done for the first time. Equation (2.7) can be rewritten as

$$\nabla^2 \tilde{E}_z^{sc} + \frac{\omega^2}{c^2} \tilde{E}_z^{sc} = 0 \quad (2.35)$$

Or

$$\nabla^2 \tilde{E}_z^{sc} - \frac{(j\omega)^2}{c^2} \tilde{E}_z^{sc} = 0 \quad (2.36)$$

The time domain version of (2.36) is

$$\nabla^2 E_z^{sc} - \frac{1}{c^2} \frac{\partial^2 E_z^{sc}}{\partial t^2} = 0 \quad (2.37)$$

similarly its weak formulation expression is

$$R = \iint_{\Omega} \left( \nabla W \bullet \nabla E_z^{sc} + \frac{1}{c^2} W \frac{\partial^2 E_z^{sc}}{\partial t^2} \right) d\Omega - \oint_{\Gamma_s} W \frac{\partial E_z^{sc}}{\partial \rho} d\Gamma = 0 \quad (2.38)$$

where  $E_z^{sc}$  is the scattered field variable in the time domain. The time domain version of the first order boundary condition (2.15) can be found the same way



$$\frac{\partial \tilde{E}_z^{sc}}{\partial \rho} = \left( -\frac{1}{2\rho} - \frac{j\omega}{c} \right) \tilde{E}_z^{sc} \quad (2.39)$$

And by applying ILT to it

$$\frac{\partial E_z^{sc}}{\partial \rho} = -\frac{\tilde{E}_z^{sc}}{2\rho} - \frac{1}{c} \frac{d\tilde{E}_z^{sc}}{dt} \quad (2.40)$$

The time domain version of the boundary integral of (2.22) is

$$\oint_{\Gamma_s} W \frac{\partial E_z^{sc}}{\partial \rho} \bigg|_{\rho=\rho_a} d\Gamma = \sum_{n=-\infty}^{\infty} \oint_{\Gamma_s} W e^{jn\phi} d\Gamma \left( g_n(t) * \oint_{\Gamma_s} E_z^{sc}(t, \rho_a, \phi) e^{-jn\phi} d\Gamma \right) \quad (2.41)$$

where the symbol  $*$  denotes the convolution operator. The multiplication in the Laplace domain became a convolution in the time domain. The convolution kernel  $g_n(t)$  is the inverse Laplace transform (ILT) of  $G_n(\omega)$  in (2.23). Following finite element geometric discretisation of the weighted residual formulation using the Galerkin procedure, (2.38) and (2.41) lead to the following global matrix equation (before the inhomogeneous Dirichlet boundary condition is accounted for)

$$[\mathbf{S}^\Omega] \{\mathbf{E}_z^{sc}\} + \frac{1}{c^2} [\mathbf{T}^\Omega] \frac{d^2 \{\mathbf{E}_z^{sc}\}}{dt^2} + [\mathbf{\Psi}^\Gamma(t)] * \{\mathbf{E}_z^{sc}\} = \{\mathbf{0}\} \quad (2.42)$$

The sub-matrices  $[\mathbf{S}^\Omega]$ ,  $[\mathbf{T}^\Omega]$  are obtained from surface elemental matrix entries that are identical to those of the FEFD method. The entries of  $[\mathbf{\Psi}^\Gamma]$  are of the form

$$\Psi_{ij}^{kl,e} = - \sum_{n=-\infty}^{\infty} g_n(t) B_{n,i}^k C_{n,j}^l \quad (2.43)$$

As described before the summation of (2.43) is truncated at  $-N \leq n \leq N$ , where  $N=15$ . The terms  $B$  and  $C$  are given in (2.32) and (2.33). Using the Vector Fitting method [12], function  $G_n$  can be approximated as (1.29)

$$G_n(\omega) \approx \sum_{m=1}^M \frac{r_{m,n}}{s - a_{m,n}} + h_n + d_n s \quad (2.44)$$

where  $n$  is the order of function  $G_n$ , as defined in (2.24),  $M$  is the number of poles used,  $r_{m,n}$ ,  $a_{m,n}$  are the pole coefficients (or residues) and pole locations respectively for order  $n$  and  $h_n$ ,  $d_n$  are the steady and proportional terms for order  $n$ .

By applying Inverse Laplace Transform to (2.44),  $g_n(t)$  can be expressed in the following form

$$g_n(t) = d_n \delta(t) + h_n \delta'(t) + \sum_{m=1}^M r_{m,n} e^{a_{m,n} t} \quad (2.45)$$

where  $\delta(t)$  is the Dirac function [21 p. 33],  $\delta'(t)$  is its first derivative, and  $d_n$ ,  $h_n$ ,  $r_{m,n}$ ,  $a_{m,n}$  are the VF computed coefficients (see Chapter 3). Substituting (2.45) in (2.43) leads to

$$\Psi_{ij}^{kl,e} = - \sum_{n=-\infty}^{\infty} d_n \delta(t) B_{n,i}^k C_{n,j}^l - \sum_{n=-\infty}^{\infty} h_n \delta'(t) B_{n,i}^k C_{n,j}^l - \sum_{m=1}^M r_{m,n} e^{a_{m,n} t} B_{n,i}^k C_{n,j}^l \quad (2.46)$$

Thus, the convolution term in (2.42) can be expressed as

$$[\Psi^\Gamma(t)] * \{\mathbf{E}_z^{sc}\} = [\mathbf{Q}^\Gamma] \{\mathbf{E}_z^{sc}\} + [\mathbf{V}^\Gamma] \frac{d\{\mathbf{E}_z^{sc}\}}{dt} + \{\mathbf{D}^\Gamma(t)\} \quad (2.47)$$

where the entries of  $[\mathbf{Q}^\Gamma]$ ,  $[\mathbf{V}^\Gamma]$  and  $\{\mathbf{D}^\Gamma(t)\}$  are

$$Q_{ij}^{kl,e} = - \sum_{n=-\infty}^{\infty} d_n B_{n,i}^k C_{n,j}^l \quad (2.48)$$

$$V_{ij}^{kl,e} = - \sum_{n=-\infty}^{\infty} h_n B_{n,i}^k C_{n,j}^l \quad (2.49)$$

$$D_i^{kl,e}(t) = - \sum_j \sum_{n=-\infty}^{\infty} B_{n,i}^k C_{n,j}^l \sum_{m=1}^M R_{m,n,j}(t) \quad (2.50)$$

$$R_{m,n,j}(t) = r_{m,n} e^{a_{m,n} t} * E_{z,j}^{sc}(t) = \int_0^t r_{m,n} e^{a_{m,n}(t-\tau)} E_{z,j}^{sc}(\tau) d\tau \quad (2.51)$$

Therefore (2.42) can be rewritten as

$$[\mathbf{S}^\Omega + \mathbf{Q}^\Gamma] \{\mathbf{E}_z^{sc}\} + [\mathbf{V}^\Gamma] \frac{d\{\mathbf{E}_z^{sc}\}}{dt} + \frac{1}{c^2} [\mathbf{T}^\Omega] \frac{d^2\{\mathbf{E}_z^{sc}\}}{dt^2} + \{\mathbf{D}^\Gamma(t)\} = \{\mathbf{0}\} \quad (2.52)$$

In the time discretisation of (2.52),  $t = q \Delta t$  where  $q$  is the current time step number and  $\Delta t$  is the time step interval. The Newmark-beta formulation [22], [23], [24], as employed in [10], is used except for the column vector  $\{\mathbf{D}^\Gamma(t)\}$  which is evaluated at time step  $q$ , i.e.  $\{\mathbf{D}^\Gamma(t=q\Delta t)\} = \{\mathbf{D}^\Gamma\}^q$ . Because of the exponential terms present in the convolution (2.45), the value of the latter, at time step  $q$ , is obtained recursively [14]

$$R_{m,n,j}^q = e^{\alpha_{m,n}\Delta t} R_{m,n,j}^{q-1} + r_{m,n} \frac{\Delta t}{2} \left[ e^{\alpha_{m,n}\Delta t} E_{z,j}^{sc}((q-1)\Delta t) + E_{z,j}^{sc}(q\Delta t) \right] \quad (2.53)$$

The Newmark-beta time discretization for the field component will be [10]

$$\frac{d^2\{E_z^{sc}(t)\}}{dt^2} = \frac{1}{\Delta t^2} (\{E_z^{sc}\}^{q+1} - 2\{E_z^{sc}\}^q + \{E_z^{sc}\}^{q-1}) \quad (2.54)$$

$$\frac{d\{E_z^{sc}(t)\}}{dt} = \frac{1}{2\Delta t} (\{E_z^{sc}\}^{q+1} - \{E_z^{sc}\}^{q-1}) \quad (2.55)$$

$$\{E_z^{sc}(t)\} = \beta \{E_z^{sc}\}^{q+1} + (1-2\beta) \{E_z^{sc}\}^q + \beta \{E_z^{sc}\}^{q-1} \quad (2.56)$$

where  $\beta = 0.25$ . Following time discretisation (2.52) becomes

$$[\mathbf{K}^{\Omega,\Gamma}] \{\mathbf{E}_z^{sc}\}^{q+1} = \{\mathbf{b}\} \quad (2.57)$$

where

$$\{\mathbf{b}\} = [\mathbf{L}_1^{\Omega,\Gamma}] \{\mathbf{E}_z^{sc}\}^q - [\mathbf{L}_2^{\Omega,\Gamma}] \{\mathbf{E}_z^{sc}\}^{q-1} - \{\mathbf{D}^\Gamma\}^q \quad (2.58)$$

$$[\mathbf{K}^{\Omega,\Gamma}] = \frac{1}{c^2 \Delta t^2} [\mathbf{T}^\Omega] + \frac{1}{4} [\mathbf{S}^\Omega] + \frac{1}{2\Delta t} [\mathbf{V}^\Gamma] + \frac{1}{4} [\mathbf{Q}^\Gamma] \quad (2.59)$$

$$[\mathbf{L}_1^{\Omega,\Gamma}] = \frac{2}{c^2 \Delta t^2} [\mathbf{T}^\Omega] - \frac{1}{2} [\mathbf{S}^\Omega] - \frac{1}{2} [\mathbf{Q}^\Gamma] \quad (2.60)$$

$$[\mathbf{L}_2^{\Omega,\Gamma}] = \frac{1}{c^2 \Delta t^2} [\mathbf{T}^\Omega] + \frac{1}{4} [\mathbf{S}^\Omega] - \frac{1}{2\Delta t} [\mathbf{V}^\Gamma] + \frac{1}{4} [\mathbf{Q}^\Gamma] \quad (2.61)$$

The global matrices  $[\mathbf{K}^{\Omega,\Gamma}]$ ,  $[\mathbf{L}_1^{\Omega,\Gamma}]$ ,  $[\mathbf{L}_2^{\Omega,\Gamma}]$  are real. They are assembled in the same way as matrix  $[\mathbf{M}^{\Omega,\Gamma}]$  in (2.29) and are created once. The vector  $\{\mathbf{b}\}$  represents the right hand side of (2.57). The Dirichlet boundary condition is applied to (2.57) as in (2.29) and hence the vector  $\{\mathbf{b}\}$  is updated with entries equal to “minus the incident field” at time step number  $q+1$ . Also updated at each time step are the column vectors  $\{\mathbf{D}^\Gamma\}^q$ ,  $\{\mathbf{E}_z^{sc}\}^q$  and  $\{\mathbf{E}_z^{sc}\}^{q-1}$ . The matrix equation (2.57) is solved using the direct matrix solver MA28 from the Harwell Subroutine Library. The matrices  $[\mathbf{K}^{\Omega,\Gamma}]$ ,  $[\mathbf{L}_1^{\Omega,\Gamma}]$ ,  $[\mathbf{L}_2^{\Omega,\Gamma}]$  are partially sparse/partially dense. This is because of the submatrices with the superscript  $\Gamma$  which are related with the computationally costly double boundary integral of (2.41) are fully populated. Note that matrix  $[\mathbf{K}^{\Omega,\Gamma}]$  is time invariant and needs to be factorized only once.

The incident field is a sinusoidal wave modulated by a Gaussian pulse,

$$E_z^{inc}(t) = E_0 \exp\left[-\frac{(q - q_0 + \frac{x}{c\Delta t})^2}{2W^2}\right] \sin[2\pi f_c \Delta t (q - q_0 + \frac{x}{c\Delta t})] \quad (2.62)$$

where  $q_0\Delta t$  is a deliberately introduced time delay,  $W\Delta t$  is the pulse width and  $f_c$  is a suitably chosen central frequency. Sinusoidal signals modulated with a Gaussian pulse are used in FETD simulations for the modelling of problems of plane wave incidence [9, 25, 26]. The incident wave propagates in the negative  $x$ -direction, which is why the proper time delay related with  $x$  has been incorporated to it. This pulse has symmetry about the central frequency  $f_c$  and a zero dc component [27]. Moreover it should be  $q_0 > 3W$  [27].

## 2.7 Numerical Results

To validate the accuracy of the work the FETD results are compared with FEFD ones and analytical or other published results where available. Three PEC

cylindrical cross-sections are considered: circular, square and triangular. The results are expressed in terms of bistatic scattering width in terms of the electric field component

$$\sigma_{2-D}(\theta) = \frac{2\lambda}{\pi} \frac{\left| \sum_{n=-\infty}^{\infty} A_n j^n e^{jn\theta} \right|^2}{\left| \tilde{E}_z^{inc} \right|^2} \quad (2.63)$$

The terms  $A_n$  can be found by applying (2.20) to the scattered field along the outer boundary. In the FETD modeling the Fourier transform of the scattered and incident field are required which are obtained with the use of the iterative algorithm of [28 pp. 21-22]. The reason that this algorithm is preferred is specific. The interest in this work is in obtaining the RCS of a cylindrical scatterer at a certain frequency (0.3GHz) for all angles. This algorithm allows the calculation of the Fourier transform at each point at the outer boundary, which is updated every timestep until the end of the simulation. This means that at the end there is one Fourier transform value for each point. This is more efficient than storing the field in time domain for each point at the outer boundary for each timestep and applying Fourier transform afterwards to them.

This algorithm [28 pp. 21-22] is repeated shortly here for convenience. Assuming that  $\tilde{E}_z^{sc}(f_c)$  is the Fourier transform at frequency  $f_c$  of the time domain field  $E_z^{sc}(t)$  at time  $t$ , then these will be connected by

$$\tilde{E}_z^{sc}(f_c) = \int_0^{t_T} E_z^{sc}(t) e^{-j2\pi f_c t} dt \quad (2.64)$$

Where  $t_T$  is the total time of the simulation, which will be

$$t_T = q_{max} \Delta t \quad (2.65)$$

and  $q_{max}$  is the maximum number of iterations of the time domain code, or in other words the maximum number of timesteps. By discretising (2.64) it becomes

$$\tilde{E}_z^{sc}(f_c) = \sum_{q=0}^{q_{\max}} E_z^{sc}(q\Delta t) e^{-j2\pi f_c q\Delta t} \quad (2.66)$$

And by separating the real and the imaginary part

$$\tilde{E}_z^{sc}(f_c) = \sum_{q=0}^{q_{\max}} E_z^{sc}(q\Delta t) \cos(2\pi f_c q\Delta t) - j \sum_{q=0}^{q_{\max}} E_z^{sc}(q\Delta t) \sin(2\pi f_c q\Delta t) \quad (2.67)$$

Using this algorithm, the Fourier transform of the scattered field for frequency  $f_c$  at timestep  $q_{\max}$  at each point at the outer boundary is calculated by

$$\tilde{E}_z^{sc}(\rho_a, \theta, f_c) = \sum_{q=0}^{q_{\max}} E_z^{sc}(\rho_a, \theta, q\Delta t) \cos(2\pi f_c q\Delta t) - j \sum_{q=0}^{q_{\max}} E_z^{sc}(\rho_a, \theta, q\Delta t) \sin(2\pi f_c q\Delta t) \quad (2.68)$$

This algorithm is performed by finding the frequency values at timestep  $q+1$  from the frequency values at timestep  $q$  and the time values at timestep  $q+1$  which can be expressed in computer code similarly to [28 p.22] as

$$real(\tilde{E}_z^{sc}(\rho_a, \theta, f_c)) = real(\tilde{E}_z^{sc}(\rho_a, \theta, f_c)) + E_z^{sc}(\rho_a, \theta, (q+1)\Delta t) \cos(2\pi f_c (q+1)\Delta t) \quad (2.69)$$

$$imag(\tilde{E}_z^{sc}(\rho_a, \theta, f_c)) = imag(\tilde{E}_z^{sc}(\rho_a, \theta, f_c)) - E_z^{sc}(\rho_a, \theta, (q+1)\Delta t) \sin(2\pi f_c (q+1)\Delta t) \quad (2.70)$$

The same equations (2.67)-(2.70) are also applied to the incident field of (2.62) for  $x=0$ . This is used for the normalisation of the calculated values of the Fourier transform of the scattered field. This is how FETD simulations provide in principle the same results as the FEFD ones.

In the simulations for the order  $n$  of the summations of (2.31) and (2.43) it was  $-N \leq n \leq N$ , where  $N = 15$ . This number is adequate for simulating the scattering from these cylindrical structures. The Vector Fitting approximation is applied with the use of the VECTFIT software which is available in public domain

[29]. Certain input parameters must be set in order to use this software. This aspect of the approximation will be thoroughly discussed and investigated in the next chapter. At this point the input parameters used in this chapter will be given for anyone who wishes to repeat this work. These input parameters for VECTFIT are (i)  $f_{max}=3\text{GHz}$  ; (ii) 3000 samples; (iii) iter = 20 iterations; (iv) asympflag = 3 and (v)  $M=10$  poles. More than 6 elements per wavelength were employed at the outer boundary. Table 2.1 presents the details for the parameters for each structure.

Fig. 2.3 shows the circular cylinder's cross-section and the FE mesh. The numerical results for the application first order absorbing boundary condition in the frequency domain and the time domain are in Figure 2.4. The numerical results for the MNRBC are in Fig. 2.5. In both cases the simulation results for the Bistatic Scattering Width (BSW) are compared with the analytical results, which refers to the closed form [20]. These numerical results include also the error comparison,  $10\log_{10}|e_{BSW}|$ . This is defined as the difference between the calculated value of the bistatic scattering width using the finite element simulations and the reference solution, which in this case is the analytical.

$$e_{BSW} = BSW_{FEM} - BSW_{reference} \quad (2.71)$$

Fig. 2.6 shows the square cylinder's geometry and its mesh. Fig. 2.7 shows the BSW comparison for this structure. The reference solution results were obtained from [30]. Lastly, in Fig. 3.8, there is the depiction of the triangular cylinder cross-section. The BSW results of this scatterer were compared with those of [5] and in order to be able to compare them with the reference results, Fig. 2.9 is presented in dB. In all cases the FETD and FEFD results are practically indistinguishable.

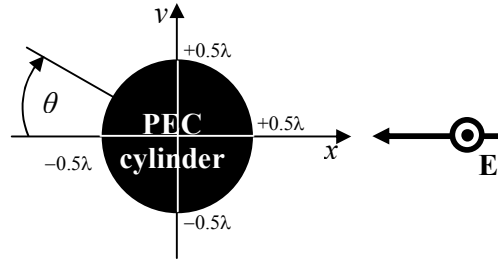
**Table 2.1**

Simulation parameters

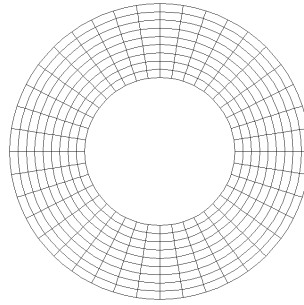
Parameters	Geometry (cross-section)		
	Circular	Square	Triangular
Elements (nodes)	360 (1160)	360 (1160)	648 (2088)
$\Delta s$ min. <sup>*†</sup> (mm)	27.778	15.910	27.778
$\Delta s$ max. <sup>*†</sup> (mm)	78.520	78.520	67.964
Courant limit <sup>†</sup> (ps)	65.473	37.5	65.473
$f_{max}^+$ (GHz)	0.451	0.451	0.451
Nyquist criterion (ps) <sup>§</sup>	1109.6	1109.6	1109.6
$\Delta t$ (ps)	40	25	40
$E_0$ (V/m)	1.0	1.0	1.0
$q_0 (\Delta t)$	700	1200	700
$W (\Delta t)$	150	240	150
$\rho_\alpha (\lambda)^*$	1.0	1.0	1.5
$f_c$ (GHz)	0.3	0.3	0.3
Number of time steps	3000	5000	4000
Computing Time (s) <sup>**</sup>	692.546	1187.593	3673.776



<sup>+</sup> frequency ( $>f_c$ ) at which the incident field spectral amplitude is  $10^{-7} \times$  (spectral amplitude at  $f_c$ ); \* at  $\lambda = 1$  m; \*\* for the FETD-MNRBC method; <sup>§</sup>  $\Delta t \leq 0.5/f_{max}$ ; <sup>†</sup>  $\Delta s$  = distance between consecutive nodes in a finite element,  $\Delta s \leq 0.125c/f_{max} = 83.2\text{mm}$ ; <sup>†</sup>  $\Delta t \leq \Delta s/(c\sqrt{2})$  adapted from [27].

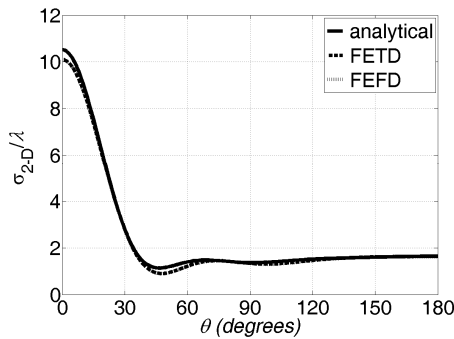


(a)

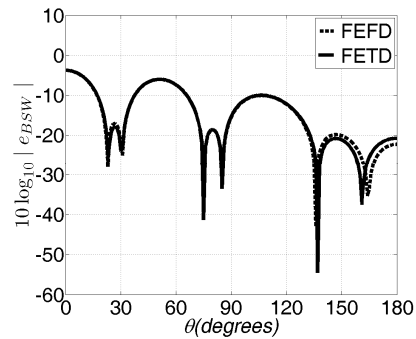


(b)

Fig. 2.3. (a) Circular cylinder geometry (b) FE mesh



(a)



(b)

Fig. 2.4. Numerical results of the circular scatterer using 1<sup>st</sup> order Absorbing Boundary Condition,

$\theta = \pi - \phi$  (a) Bistatic scattering width normalized with  $\lambda$  (b) Error of Bistatic scattering width

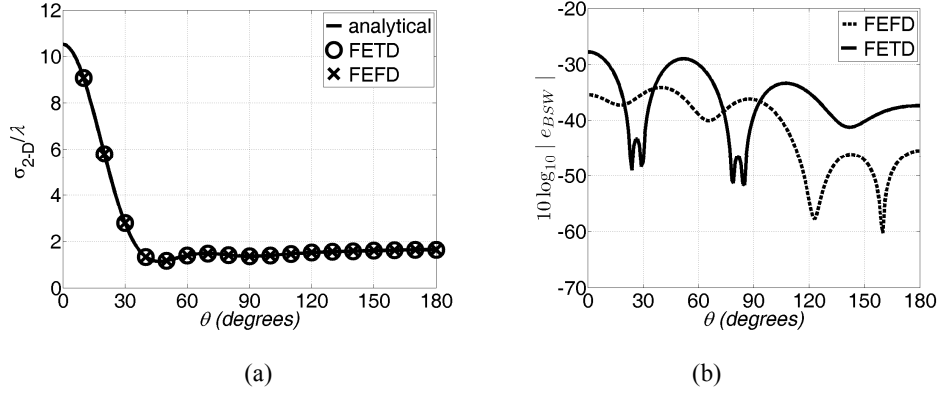
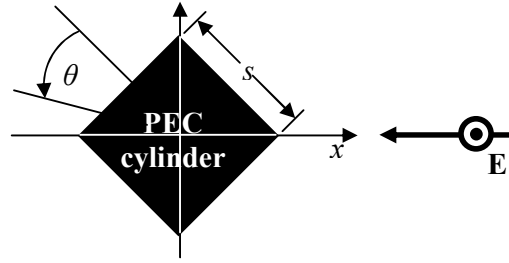
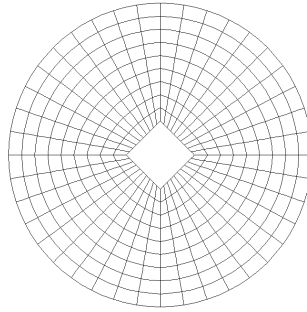


Fig. 2.5. Numerical results of the circular scatterer using MNRBC,  $\theta=\pi-\phi$ . (a) Bistatic scattering width normalized with  $\lambda$  (b) Error of Bistatic scattering width



(a)



(b)

Fig. 2.6. (a) Square cylinder geometry (b) FE mesh. The square side length is  $s = \lambda/\pi$ .

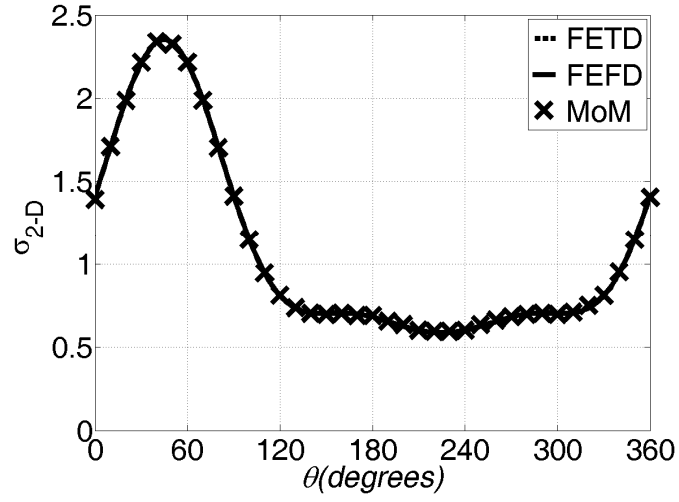
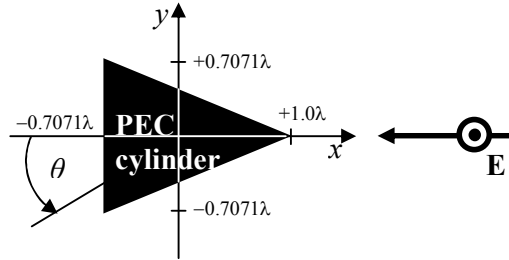
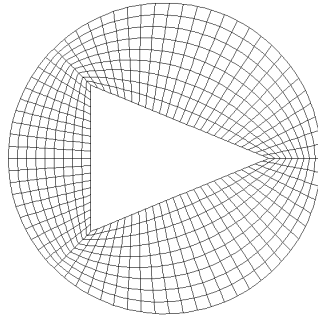


Fig. 2.7. Bistatic scattering width of the square scatterer,  $\theta = \phi - 3\pi/4$ .



(a)



(b)

Fig. 2.8. (a) Triangular cylinder geometry (b) FE mesh.

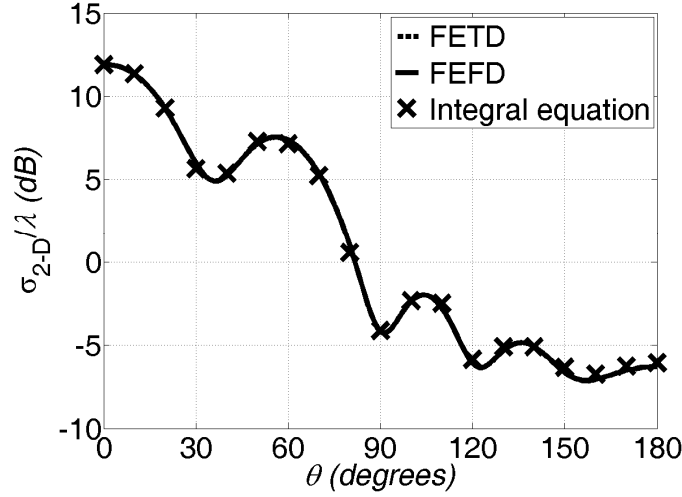


Fig. 2.9. Bistatic scattering width normalized with  $\lambda$  of the triangular scatterer in dB,  $\theta=\phi-\pi$ .

The MNRBC results were in all cases very close to the reference ones. For the case compared with the closed form it was found that the error was for all angles  $10\log_{10}|e_{BSW}| < -27.8$  while for the first order ABC it was  $10\log_{10}|e_{BSW}| < -3.75$  as highlighted in Figs 2.4 and 2.5. A couple of interesting points are the simplicity of the meshes used for these results and the fact that the MNRBC does not require extra layers. For all three structures, the FETD-MNRBC simulations were repeated for  $10^5$  timesteps and no instability was observed.

## 2.8 Scientific contribution and future work

In this chapter a FETD-MNRBC methodology that simulates the scattering of a plane wave from a 2D cylinder was presented for the first time. The numerical results presented, which included Bistatic scattering width comparisons and error plots, validated the accuracy of the methodology.

A very important part of the approach is the approximation of the kernel that appears in boundary integral term of the formulation as a summation of exponential terms using vector fitting. This way of expressing the boundary kernel has the

advantage of allowing the use of recursive convolution for computing the convolution integrals present in the FETD-MNRBC formulation, which is much more time efficient than the standard convolution. In this way the problem of not knowing the exact value of the boundary kernel was turned into an advantage.

So far the FETD-MNRBC has been applied to scattered field formulation for perfectly electrically conducting cylinders. The scattered field formulation can be extended to simulated dielectric cylinders as well [25, 31]. This is something that is investigated in Chapter 6 of this work. Before that, in Chapter 4, for the sake of completeness, the total field formulation is derived.

From duality it is straightforward to derive the formulations for TM polarisation based on the TE ones of this chapter. This formulation could be used for perfect magnetic conductors (PMC). The  $E_z$  field would be replaced with the  $H_z$  one. The same principles based on which the MNRBC was derived would still be applicable. The TM polarisation was not considered here as this chapter aimed to explain with simplicity the basic formulation of the FETD-MNRBC but is considered in Chapter 4 for the more general total field formulation.

As can be seen from (2.59)-(2.61) the formulation derived here is based on matrices that are partially dense and partially sparse. This has a negative effect on the memory and time efficiency of the approach. Therefore a sparse approach would be more advantageous. Again this is something which is performed in chapter 6.

Another important point is that the outer boundary where the mesh is truncated needs to be circular. Therefore if the cross-section of the cylinder is elongated there will be a need for a grid with unnecessary many elements. This method is more efficient when applied to a nearly circular cross-section which makes it suitable for metamaterial applications.

## REFERENCES

- [1] T. Roy, T. K. Sarkar, A. R. Djordjevic, and M. Salazar-Palma, "Time-domain analysis of TM scattering from conducting cylinders using a hybrid method," *IEEE Trans. Microwave Theory Tech*, vol. 46, no. 10, pp. 1471–1477, 1998.
- [2] S. Caorsi, and G. Cevini, "Assessment of the performances of first- and second-order time-domain ABC's for the truncation of finite element grids", *Microwave and Optical Technology Letters*, vol. 38, no. 1, pp. 11-16, 2003.
- [3] T. Rylander, and J.-M. Jin, "Perfectly matched layer for the time domain finite element method", *Journal of Computational Physics*, vol. 200, pp. 238–250, 2004.
- [4] J. M. Jin, *The Finite Element Method in Electromagnetics*, 2nd ed., Wiley-IEEE Press, New York, 2002.
- [5] A.F. Peterson and S.P. Castillo, "A Frequency-Domain Differential Equation Formulation for Electromagnetic Scattering from Inhomogeneous Cylinders" , *IEEE Transactions on Antennas Propag.*, vol. 37, no.5, pp. 601-607, 1989.
- [6] A.F. Peterson, S.L. Ray, and R. Mittra, *Computational Methods for Electromagnetics*, IEEE Press, New York, 1998.
- [7] S.-K. Jeng, and C.-H. Chen, "On Variational Electromagnetics: Theory and Application", *IEEE Transactions on Antennas and Propagation*, vol. 32, no. 9, pp. 902-907, 1984.
- [8] L.W. Pearson, R.A. Whitaker, and L.J. Bahrmasel, "An exact radiation boundary condition for the finite-element solution of electromagnetic scattering on an open domain", *IEEE Transactions on Magnetics*, vol. 25, no. 4, pp. 3046-3048, 1989.

- [9] Y. Cai and C. Mias, "Finite-element time-domain modelling of plane wave scattering by a periodic structure using an exact boundary condition", *IEE Microwaves, Antennas & Propagation*, vol. 1, no. 3, pp. 609-616, 2007.
- [10] T.H. Loh, and C. Mias, "Implementation of an exact modal absorbing boundary termination condition for the application of the finite-element time-domain technique to discontinuity problems in closed homogeneous waveguides", *IEEE Transactions on Microwave Theory and Techniques*, vol. 52, no. 3, pp. 882-888, 2004.
- [11] B. Alpert, L. Greengard, and T. Hagstrom, "Rapid evaluation of nonreflecting boundary kernels for time-domain wave propagation", *SIAM J. Numer. Anal.*, vol. 37, no. 4, pp. 1138–1164, 2000.
- [12] B. Gustavsen, and A. Semlyen, "Rational Approximation of Frequency Domain Responses by Vector Fitting", *IEEE Trans. on Power Delivery*, vol. 14, no. 3, pp. 1052-1061, 1999.
- [13] K. Bavelis and C. Mias, "Vector fitting realisation of exact time domain modal nonreflecting boundary condition", *Electronic Letters*, vol. 46, no. 11. pp 760-761, 2010
- [14] Y. Cai, and C. Mias, "Fast Finite Element Time Domain – Floquet Absorbing Boundary Condition modelling of periodic structures using recursive convolution", *IEEE Trans. Antennas Propag.*, vol. 55, no. 9, pp. 2550-2558, 2007.
- [15] J.L. Volakis, A. Chatterjee, L.C. Kempel, *Finite Element Method for Electromagnetics, Antennas, Microwave circuits and scattering applications*, IEEE press, 1998.
- [16] P.P. Silvester, and R.L. Ferrari, *Finite elements for electrical engineers*, 3rd ed., Cambridge University Press, Cambridge, 1996.

- [17] G. Dhatt, G. Touzot, *The Finite Element Method Displayed*, John Wiley & Sons, 1984.
- [18] Y. Zhu, A. Cangellaris, *Multigrid Finite Element Methods for Electromagnetic Field Modeling*, John Wiley & Sons, 2006.
- [19] F. T. Ulaby, *Fundamentals of applied electromagnetics*, Media ed., Pearson Prentice Hall, 2004.
- [20] C.A. Balanis, *Advanced Engineering Electromagnetics*, John Wiley & Sons, 1989.
- [21] M.L. Meade and C.R. Dillon, *Signals and Systems Models and Behaviour*, 2<sup>nd</sup> ed. Kluwer Academic Publishers, 2000.
- [22] N. M. Newmark, "A method of computation for structural dynamics", *J. Engineering Mechanics Division, ASCE*, vol. 85, pp. 67-94, July 1959.
- [23] O. C. Zienkiewicz, "A new look at the Newmark, HouBolt, and other time-stepping formulas: a weighted residual approach," *Earthquake Engineering and Structural Dynamics*, vol. 5, pp.413-418, 1997.
- [24] S.D. Gedney, and U. Navsariwala, "An Unconditionally Stable Finite Element Time-Domain Solution of the Vector Wave Equation", *IEEE Microwave and Guided Wave Letters*, vol. 5. no. 10, pp. 332-334, 1995.
- [25] A.F. Peterson and J. M. Jin, "A Two-Dimensional Time-domain Finite Element formulation for periodic structures.", *IEEE Transactions on Antennas Propag.*, vol. 53, no.4, pp. 1480-1488, 2005.
- [26] A.F. Peterson and J. M. Jin, "A Three-Dimensional Time-domain Finite Element formulation for periodic structures.", *IEEE Transactions on Antennas Propag.*, vol. 54, no.1, pp. 12-19, 2006.



- [27] A. Taflove, S. C. Hagness, *Computational Electrodynamics: The Finite-Difference-Time Domain Method*, 2nd ed., Boston, London, Artech House, 2000.
- [28] D. M. Sullivan, *Electromagnetic Simulations Using the FDTD method*, Wiley-IEEE Press, 2000.
- [29] <http://www.energy.sintef.no/Produkt/VECTFIT/index.asp>. Retrieved 21 April 2011.
- [30] K. Umashankar, A. Taflove, *Computational Electromagnetics*, Artech House, 1993.
- [31] I. Bardi, Z. Badics, and Z. J. Cendes, "Total and Scattered Field Formulations in the Transfinite Element Method", *IEEE Trans. on Magnetics*, vol. 44, no. 6, pp. 778-781, 2008.

## CHAPTER 3

### VF approximation of a cylindrical boundary kernel

#### 3.1 Introduction

The scope of this chapter is to present for the first time a Vector fitting (VF) [1] approximation of the cylindrical boundary kernel [2] that appears in the boundary integral of the FETD-MNRBC. The derivation of the frequency response of this kernel was performed in the previous chapter and now the focus is on the VF approximation of this function and how this is affected by the input parameters of the VF software and the approximation approach.

Vector Fitting performs a partial fraction expansion for a given frequency domain function [1]. It is applicable not only to finite element simulations but to a wide range of applications [3-7]. For FETD application it allows the boundary kernel to be expressed as a sum of exponentials and thus the boundary integral in the time domain is calculated recursively [8].

To employ the modal nonreflecting boundary condition (MNRBC) in cylindrical coordinates in the finite element time domain (FETD) method, a time domain kernel expression must be found such that it is the inverse Laplace transform (ILT) of a known frequency domain function. The inverse Laplace transformation is achieved using a methodology based on the partial fraction expansion of the frequency domain function. A much simpler approach to [9], which is based on the Vector Fitting method [1] is employed in this work. The properties of this approach and the accuracy are discussed.

This chapter begins with the presentation of the fundamental concepts of a VF approximation. It continues with the cylindrical boundary kernels and the two VF approaches for their approximation that are utilized in this work. In the first approach the VF software is applied directly to the frequency response  $G_n$  (2.24) (called the VFG approach) of the boundary kernel and in the second approach VF is applied to  $U_n$  function (3.8) which is the generic form of  $G_n$  and then the VF parameters are transformed through (3.21) to obtain  $G_n$  (called the VFU approach). The relation between these two approaches is then discussed. The next part of this chapter is dedicated to the numerical results. Firstly, through experimentation, the parameters that affect the accuracy of the VF algorithm such as the maximum frequency and the number of frequency samples are investigated. Next the boundary kernel approximation of cylindrical kernels of [9] (equation (3.7) and (3.8)) is compared with the VF approximation of these kernels [2]. Lastly, the accuracy of the two proposed VF approximations are compared in terms of separate order kernel comparison and final FEM comparison for the BSW of cylindrical structures.

Vector Fitting is extensively used in this work. Later in Chapter 5 it is used for the approximation of the incident field components for the periodic FETD-MNRBC. Therefore it is required to make a detailed presentation of the approaches incorporated, the parameters that affect it and validate its accuracy for cylindrical FEM use.

### **3.2 Vector Fitting approximation**

Vector Fitting is an accurate and efficient tool for rational approximation of a known frequency domain response [1]. This approximation is obtained using the Matlab subroutine VECTFIT which is available in the public domain [10]. A known frequency response  $F(s)$  is approximated as [1]:

$$F(s) \approx F_{app}(s) = \sum_{m=1}^M \frac{r_m}{s - a_m} + h + ds \quad (3.1)$$

where  $s$  is the Laplace domain variable and in this case  $s=j\omega$ ,  $\omega$  is the angular frequency,  $M$  is the number of poles used,  $r_m$ ,  $a_m$  are the pole coefficients (or residues) and pole locations respectively and are either real or conjugate pairs,  $h$ ,  $d$  are the steady and proportional term and are always real and the software allows to omit them. The subscript ‘*app*’ indicates an approximation. The time domain function can be obtained from (3.1) by applying Inverse Laplace Transform (ILT) to it:

$$f_{app}(t) = \sum_{m=1}^M r_m e^{a_m t} + h\delta(t) + d\delta'(t) \quad (3.2)$$

where  $\delta(t)$  is the Dirac or impulse function [11] and  $\delta'(t)$  its first derivative.

For the application of the VECTFIT subroutine some input parameters need to be set. These parameters are explained in detail in [11], but they will be shortly described here. These parameters are:

- The number of poles in (3.1)
- The maximum frequency which defines the frequency range of interest for the approximated function
- The number of frequency samples in this range
- Parameter ‘iter’ which defines the number of iterations performed by the software in order to find the poles in (3.1)
- Parameter ‘asymflag’ which defines whether  $h$  and  $d$  in (3.1) will be calculated or set to zero. For asymflag=3 they are calculated and for asymflag=1 they are set to zero.

### 3.3 Cylindrical boundary kernels

In order to apply the MNRBC in the FETD method, one must find, for each scattered field order  $m$  (2.16), the time domain expression of a cylindrical nonreflecting boundary kernel that appears in the MNRBC. The kernel is the inverse Laplace transform (ILT) of a known function that appears in the MNRBC in the frequency domain.

In this work two approaches to the approximation of the kernel are considered. The first one is to apply VF software directly to the frequency response of the kernel (2.24) and the second is to apply VF to its generic form (3.8) (also used in [9]) and then appropriately scale the result and add the large argument approximation to obtain the form of (2.24), which unlike (3.8) depends upon the radial distance  $\rho$  and the speed of light  $c$ . These points are examined in detail below. The proofs for the small and the large arguments approximations of these functions are included in Appendix D.

#### 3.3.1 FETD-MNRBC form

The frequency domain expression  $G_n(s)$  or  $G_n(\omega)$  in terms of angular frequency of this kernel is given in (2.24) The small and large argument approximations for radius  $\rho$  and order  $n$  of  $G_n(\omega)$  are

$$\lim_{\omega \rightarrow 0} G_n(\omega) = -\frac{|n|}{2\pi\rho} \quad (3.3)$$

and

$$\lim_{\omega \rightarrow \infty} G_n(\omega) = -\frac{k_0}{2\pi\rho} \mathbf{j} - \frac{1}{4\pi\rho^2} \quad (3.4)$$

or

$$\lim_{\omega \rightarrow \infty} G_n(\omega) = -\frac{1}{2\pi\rho c} s - \frac{1}{4\pi\rho^2} \quad (3.5)$$

As can be seen (3.5) has a steady and a proportional term so there is need for nonzero values for  $d$  and  $h$  parameters of (3.1). Thus the VF approximated boundary kernel will have the form

$$g_{n,app}(t) = \sum_{m=1}^M r_{m,n} e^{a_{m,n}t} + h_n \delta(t) + d_n \delta'(t) \quad (3.6)$$

Use of this kernel for FETD simulations was made in Chapter 2. The disadvantage of this approach is that for different values of the radial distance  $\rho$  there is need for different VF parameters, thus the VECTFIT software must be rerun. In order to avoid rerunning the software for different set of these values it is beneficial to work with the generic form of the kernel.

### 3.3.2 Generic form

The Laplace transform expression  $Q_n(s)$  of the time domain cylindrical nonreflecting boundary kernel  $q_n(t)$ , used by Alpert et al (eq. 2.13 in [9]), is

$$Q_n(s) = \frac{s}{c} + \frac{1}{2\rho} + \frac{s}{c} \frac{K'_n(\rho s/c)}{K_n(\rho s/c)} = \frac{1}{\rho} \left[ v + \frac{1}{2} + v \frac{K'_n(v)}{K_n(v)} \right], \quad v = \frac{\rho s}{c} \quad (3.7)$$

where  $K_n$  is the modified Bessel function of the second kind and  $n$ th order. The derivative  $K'_n$  of  $K_n$  is with respect to the argument  $\rho s/c$ . From the linearity of the Laplace transform ( $1/\rho$  in (3.7)) and its scaling properties ( $v = \rho s/c$ ) it is sufficient to expand the following expression in terms of partial functions

$$U_n(s) = s + \frac{1}{2} + s \frac{K'_n(s)}{K_n(s)} = s + \frac{1}{2} - s \frac{K_{n+1}(s)}{K_n(s)} + n \quad (3.8)$$

In (3.8), the derivative  $K'_n$  of  $K_n$  is now with respect to the argument  $s$ . Once the ILT of  $U_n(s)$  is found, denoted as  $u_n(t)$ , then the ILT of (3.7) can be obtained, for any  $\rho$  and  $c$ , by applying the properties of linearity and scaling as follows

$$q_n(t) = \frac{c}{\rho^2} u_n\left(\frac{c}{\rho} t\right) \quad (3.9)$$

The last expression in (3.8) is obtained using equations of modified Bessel functions in [12] for the calculation of the derivative and it is the expression employed in VECTFIT with  $s = j\omega$ . VF approximately expresses  $U_n(s)$  in (3.8) in the following form

$$U_n(s) \approx U_{n,app}(s) = D_n + H_n s + \sum_{m=1}^M \frac{R_{m,n}}{s - A_{m,n}} \quad (3.10)$$

To enable VECTFIT to produce the desirable results, the asymptotic value of  $U_n(s)$  as  $s \rightarrow 0$  is required. As shown in Appendix D the small argument approximation of  $U_n(s)$  is found to be

$$\lim_{s \rightarrow 0} U_n(s) \approx \frac{1}{2} - |n| \quad \forall n \in \mathbf{Z} \quad (3.11)$$

The small argument approximation is needed as an input for zero frequency in the VECTFIT software. Furthermore, computing  $D_n$  and  $H_n$  is optional in VECTFIT and therefore knowledge of the large argument approximation of  $U_n(s)$  is beneficial. In this case,  $U_n(s) \rightarrow 0$  as  $s \rightarrow \infty$ , hence,  $D_n = H_n = 0$ . Therefore, after applying ILT to the partial fraction expansion in (3.10) one obtains the following approximate time domain expression for  $u_n(t)$ ,

$$u_{n,app}(t) = \sum_{m=1}^M R_{m,n} e^{A_{m,n} t} \quad (3.12)$$

### 3.3.3 Relation between the two forms

The relation between modified Bessel and Hankel function of the second kind is [12]

$$K_n(v) = -\frac{1}{2} \pi j e^{-jn\frac{\pi}{2}} H_n^{(2)}(ve^{-j\frac{\pi}{2}}) \quad (3.13)$$

Thus,

$$K_n(v) = -\frac{1}{2} \pi j e^{-jn\frac{\pi}{2}} H_n^{(2)}(z) \quad (3.14)$$

$$K_{n+1}(v) = -\frac{1}{2} \pi j e^{-j(n+1)\frac{\pi}{2}} H_{n+1}^{(2)}(z) \quad (3.15)$$

Therefore

$$\begin{aligned} G_n(\omega) &= \frac{1}{2\pi\rho^2} \left[ -z \frac{H_{n+1}^{(2)}(z)}{H_n^{(2)}(z)} + n \right] = \frac{1}{2\pi\rho^2} \left[ -\frac{v}{j} \frac{K_{n+1}(v)e^{j\frac{\pi}{2}}}{K_n(v)} + n \right] \\ &= \frac{1}{2\pi\rho} \underbrace{\left\{ \frac{1}{\rho} \left[ -v \frac{K_{n+1}(v)}{K_n(v)} + n \right] \right\}}_{P_n(s)} = \frac{1}{2\pi\rho} P_n(s) \end{aligned} \quad (3.16)$$

Now, from (3.8) and (3.10) it is

$$U_n(s) = s + \frac{1}{2} + s \frac{K'_n(s)}{K_n(s)} = s + \frac{1}{2} - s \frac{K_{n+1}(s)}{K_n(s)} + n \approx \sum_{m=1}^M \frac{R_{m,n}}{s - A_{m,n}} \quad (3.17)$$

And for function  $Q_n(s)$  of equation (3.7) by replacing  $v = \frac{\rho s}{c}$

$$\begin{aligned} Q_n(s) &= \frac{1}{\rho} \left[ v + \frac{1}{2} - v \frac{K_{n+1}(v)}{K_n(v)} + n \right] = \\ &= \frac{s}{c} + \frac{1}{2\rho} + \underbrace{\left\{ \frac{1}{\rho} \left[ -\frac{s\rho}{c} \frac{K_{n+1}(\frac{s\rho}{c})}{K_n(\frac{s\rho}{c})} + n \right] \right\}}_{P_n(s)} \approx \sum_{m=1}^M \frac{\frac{c}{\rho^2} R_{m,n}}{s - \frac{c}{\rho} A_{m,n}} \end{aligned} \quad (3.18)$$

Thus



$$P_n(s) = -\frac{s}{c} - \frac{1}{2\rho} + Q_n(s) \approx -\frac{s}{c} - \frac{1}{2\rho} + \sum_{m=1}^M \frac{\frac{c}{\rho^2} R_{m,n}}{s - \frac{c}{\rho} A_{m,n}} \quad (3.19)$$

Therefore function  $G_n$  of (2.24) can be written as

$$G_n(\omega) = \frac{1}{2\pi\rho} P_n(s) = \frac{1}{2\pi\rho} \left[ -\frac{s}{c} - \frac{1}{2\rho} + Q_n(s) \right] \approx$$

$$-\frac{1}{2\pi\rho c} s - \frac{1}{4\pi\rho^2} + \sum_{m=1}^M \frac{\left( \frac{c}{2\pi\rho^3} R_{m,n} \right)}{s - \left( \frac{c}{\rho} A_{m,n} \right)} \quad (3.20)$$

Hence the partial fraction coefficients of  $g_n$  function (equation (3.6)) can be obtained from those of  $u_n$  from the relations

$$h_n = -\frac{1}{2\pi\rho c}, \quad d_n = -\frac{1}{4\pi\rho^2}, \quad r_{m,n} = \left( \frac{c}{2\pi\rho^3} R_{m,n} \right), \quad a_{m,n} = \left( \frac{c}{\rho} A_{m,n} \right) \quad (3.21)$$

The above derivation can be more easily understood with the help of Fig.3.1.

From function  $G_n$  by multiplying with  $2\pi\rho$  and replacing the Hankel functions of the second kind with modified Bessel functions of the second kind, the function  $P_n$  is obtained. Then by subtracting from  $P_n$  the large argument approximation, function  $Q_n$  is found. Lastly by using the Laplace transform properties of linearity and scaling the function  $U_n$  is obtained.

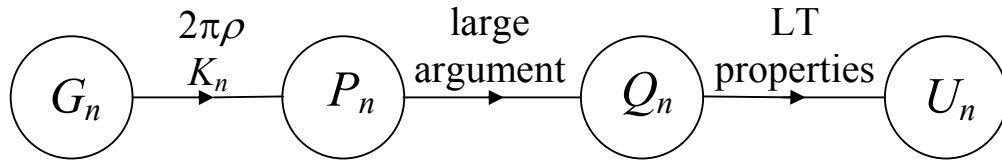


Fig 3.1 Derivation of function  $U_n$

### 3.4 Numerical Results

In this section the numerical results of the application of VECTFIT (version1) software to the kernels are presented.

#### 3.4.1 Effect of input parameters

The first thing that one should consider when implementing the VF method is the appropriate choice of the input parameters, namely the maximum frequency  $f_{max}$  and the number of frequency samples for this range. The meaning of these parameters was described in section 3.2. In this part the analysis will be held for the generic  $U_n$  for  $n=15$ . This is because 15 is the largest order used in this work for FEM simulation and  $U_n$  has a spectrum in which the significant frequency components are confined in the low frequency region which makes it more suitable for the observation of the effect of maximum frequency.

The accuracy of the partial fraction expansion using the VECTFIT software (version 1) is demonstrated by plotting the absolute value of the error  $10\log_{10}|e_n|$  versus frequency  $f$ . For a function ( $G_n(\omega)$  or  $U_n(s)$  for example) the error is defined as the difference between the exact value of the function and its approximation, i.e., for say the function  $U_n(\omega)$ ,

$$e_n(\omega) = U_n(\omega) - U_{n,app}(\omega) \quad (3.22)$$

Firstly the effect of  $f_{max}$  is considered. In Fig. 3.2 there is the plot of  $U_{15}$  in normal and logarithmic  $x$  axis. This way the shape of the function and the frequency at which it reaches zero can be more easily viewed. The exact value of  $U_{15}$  is compared against VF for  $f_{max}=10\text{Hz}$  which is indistinguishable. In Fig. 3.3 there are the error comparisons for various maximum frequencies. Specifically in Fig. 3.3 (a) there are the comparisons for  $f_{max}=0.1\text{Hz}$ ,  $f_{max}=1\text{Hz}$ ,  $f_{max}=4\text{Hz}$  and  $f_{max}=10\text{Hz}$ ; in Fig.

3.3. (b) the comparisons for  $f_{max}=100\text{Hz}$ ,  $f_{max}=1\text{KHz}$ ,  $f_{max}=10\text{KHz}$  and  $f_{max}=100\text{KHz}$  and in Fig. 3.3. (c) the comparisons for  $f_{max}=1\text{MHz}$ ,  $f_{max}=10\text{MHz}$ ,  $f_{max}=100\text{MHz}$  and  $f_{max}=1\text{GHz}$ . The rest of the input parameters used in VECTFIT were: (i) 4000 frequency samples; (ii) iter = 20 iterations; (iii) asympflag = 1 (as  $D_n = H_n = 0$ ) and (iv)  $M=10$  poles. The meaning of these parameters was clarified in section 3.2 and they are listed here for anyone interested in repeating this work. As can be seen,  $f_{max}$  should be just large enough to include all significant frequency components but not unnecessarily large.

The next parameter considered is the number of frequency samples used in the frequency range  $f_{max}$  when this frequency remains the same. In Fig. 3.4 (a) the absolute value of the error  $10\log_{10}|e_{I5}(s=j2\pi f)|$  versus frequency  $f$  for 4, 8, 40, 400 and 4000 samples can be seen. In Fig. 3.4 (b) there is a zoom in of the last three choices of frequency samples. The rest of the input parameters used in VECTFIT were: (i)  $f_{max}=10\text{Hz}$ ; (ii) iter = 20 iterations; (iii) asympflag = 1 (as  $D_n = H_n = 0$ ) and (iv)  $M=10$  poles. It is clear that from a number of samples of  $10^1$ - $10^2$  and onwards the accuracy converges and does not significantly change.

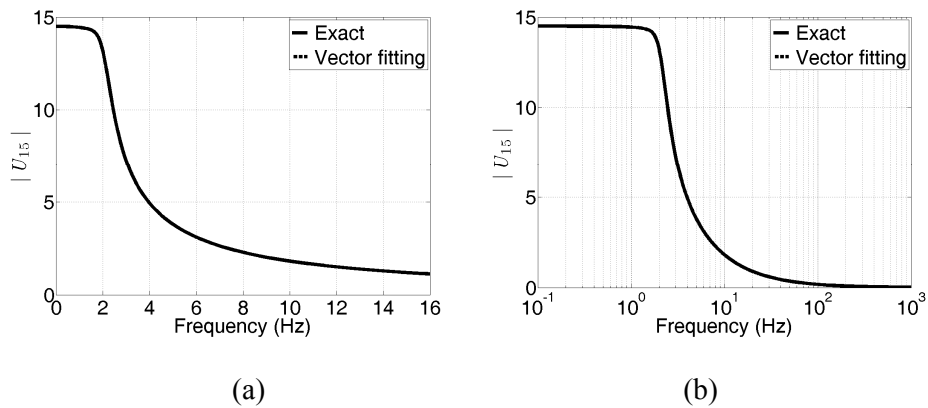


Fig 3.2  $U_{I5}$  comparison (a) normal x axis (b) logarithmic

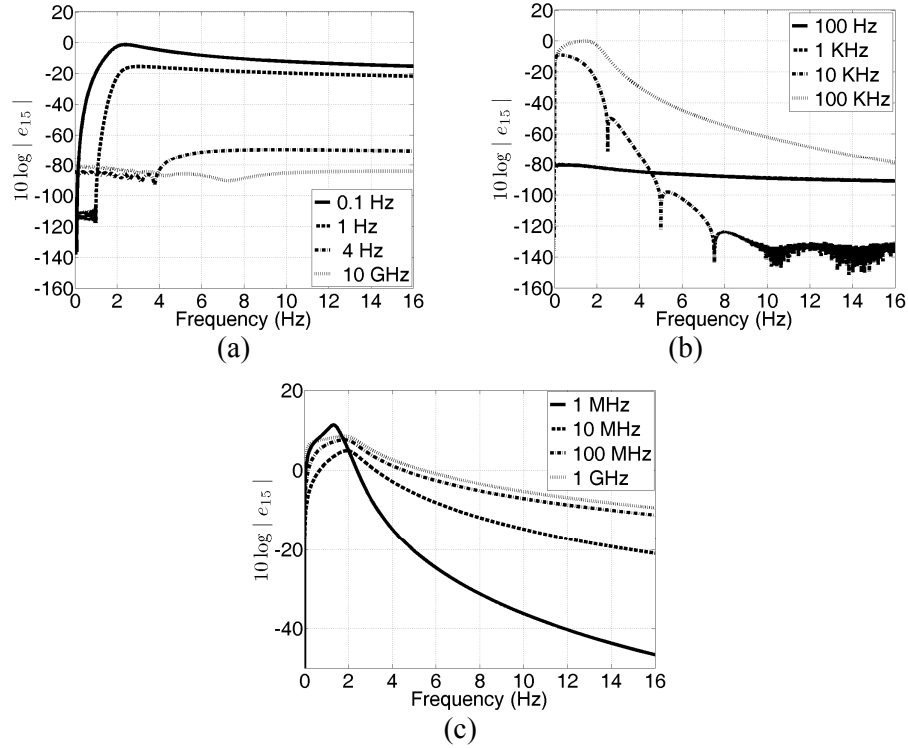


Fig 3.3 Absolute error comparisons (a)  $f_{max}=0.1\text{Hz}, f_{max}=1\text{Hz}, f_{max}=4\text{Hz}$  and  $f_{max}=10\text{Hz}$  (b)  $f_{max}=100\text{Hz}, f_{max}=1\text{KHz}, f_{max}=10\text{KHz}$  and  $f_{max}=100\text{KHz}$  (c)  $f_{max}=1\text{MHz}, f_{max}=10\text{MHz}, f_{max}=100\text{MHz}$  and  $f_{max}=1\text{GHz}$

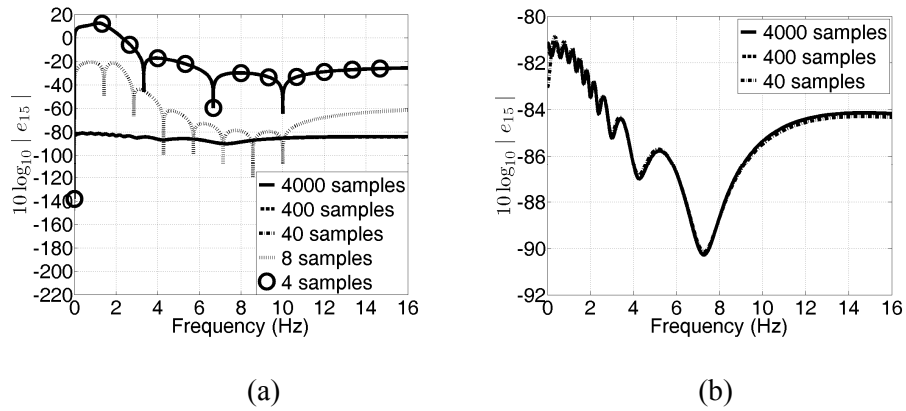


Fig 3.4 Plots of (a)  $10 \log_{10} |e_{15}(s = j2\pi f)|$  versus frequency  $f$  for 4, 8, 40, 400 and 4000

(b)  $10 \log_{10} |e_{15}(s = j2\pi f)|$  versus frequency  $f$  for 40, 400 and 4000

### 3.4.2 VF approximation of boundary kernels

This section firstly considers the comparison of the approach of [9] for the boundary kernel of  $U_n$  against the VF approach as performed in [2]. In [9] there are partial fraction coefficients for kernel modal orders  $n=1,2,3,4$ . For these orders and the same number of poles as used in [9], VF is applied to function  $U_n$  and the accuracy of both approximation approaches is demonstrated. The next step of this section is the application of VF to the kernels  $U_n$  and  $G_n$  for the use of FETD-MNRBC simulations which are used in this work.

For the comparison with [9] the input parameters used in VECTFIT were: (a) 4000 frequency samples; (b) a frequency range of  $0 \leq f \leq f_{max}$  with  $f_{max} = 4$  Hz; (c) iter = 20 iterations; and (d) asympflag = 1 (as  $D_n = H_n = 0$ ). Table 3.1 lists the computed partial fraction parameters,  $R_{m,n}$  and  $A_{m,n}$ . Their values are truncated to six decimal places. For the order of the  $U_n$  function  $n$  and the number of poles  $M$  the values tabulated in [9] are used. Figure 3.5 shows plots of the function  $U_n(s = j2\pi f)$  versus frequency  $f$  based on: (a) the exact equation (3.8); (b) the VF partial fraction approximation using the VECTFIT computed parameters in Table 3.1 (without truncation); and (c) the partial fraction approximation of Alpert et al using the tabulated parameters in [9]. The significance of this comparison is that it is indicated that both approximations are of comparable accuracy and that  $10\log_{10}|e_n| < -50$  for  $n = 1,2,3,4$ .

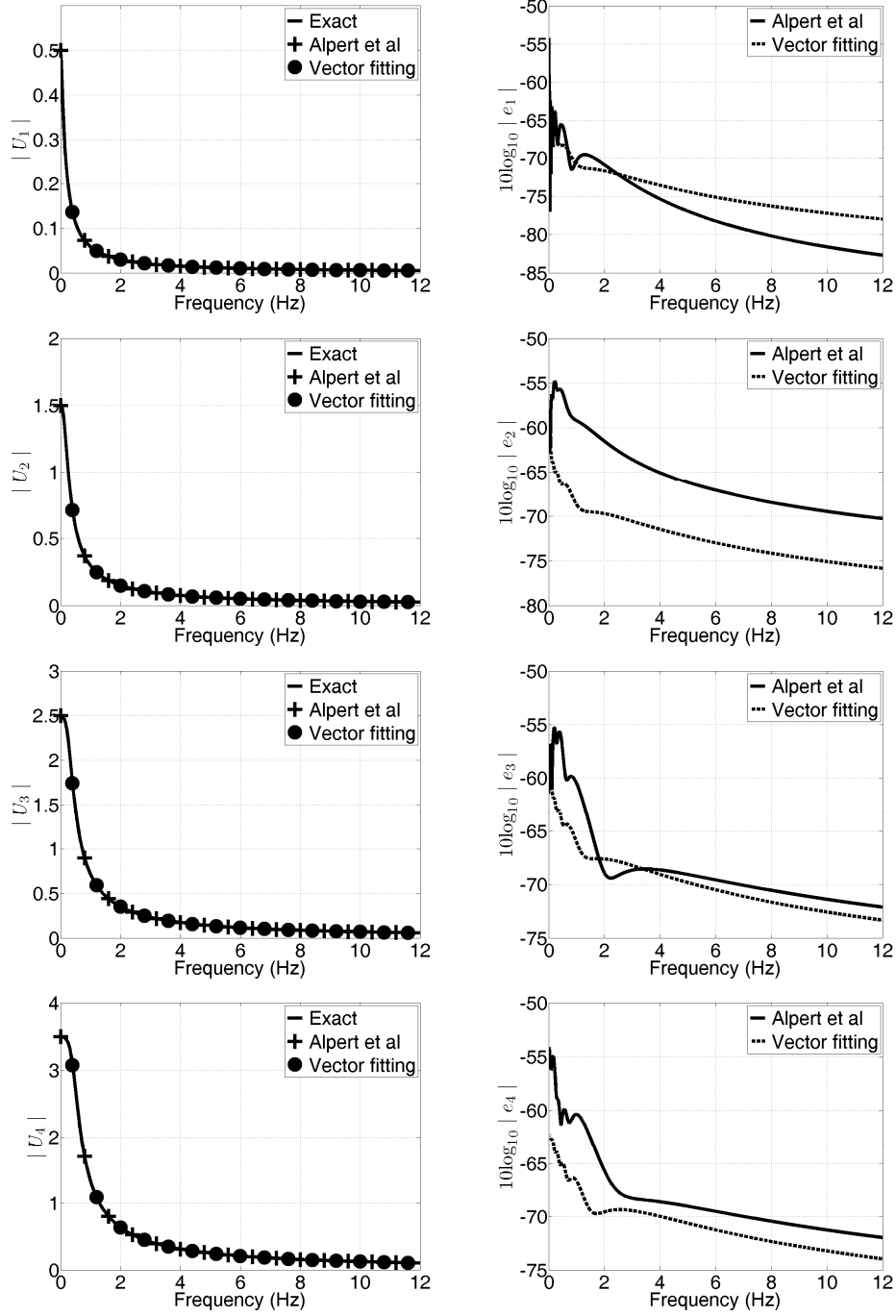


Fig 3.5 Plots of  $|U_n(s = j2\pi f)|$  and  $10\log_{10}|e_n(s = j2\pi f)|$  versus frequency  $f$  for  $n = 1, 2, 3, 4$ .

**Table 3.1**

VECTFIT computed parameters

$n$	$M$	Pole coefficients		Pole locations	
		Real	Imaginary	Real	Imaginary
1	9	$-6.125650 \times 10^{-3}$	0	$-3.465994 \times 10^0$	0
		$-5.259487 \times 10^{-2}$	0	$-1.904945 \times 10^0$	0
		$-1.381366 \times 10^{-1}$	0	$-1.091376 \times 10^0$	0
		$-1.326909 \times 10^{-1}$	0	$-6.548468 \times 10^{-1}$	0
		$-3.918820 \times 10^{-2}$	0	$-3.765733 \times 10^{-1}$	0
		$-5.643938 \times 10^{-3}$	0	$-1.921838 \times 10^{-1}$	0
		$-5.779033 \times 10^{-4}$	0	$-8.671415 \times 10^{-2}$	0
		$-3.945792 \times 10^{-5}$	0	$-3.308866 \times 10^{-2}$	0
		$-1.182999 \times 10^{-6}$	0	$-8.940158 \times 10^{-3}$	0
2	6	$2.087022 \times 10^{-4}$	0	$-2.352687 \times 10^{-1}$	0
		$1.883591 \times 10^{-2}$	0	$-6.004027 \times 10^{-1}$	0
		$9.779644 \times 10^{-1}$	0	$-1.585323 \times 10^0$	0
		$2.405753 \times 10^{-2}$	0	$-3.281031 \times 10^0$	0
		$-1.448034 \times 10^0$	$1.672191 \times 10^{-1}$	$-1.261094 \times 10^0$	$4.080800 \times 10^{-1}$
		$-1.448034 \times 10^0$	$-1.672191 \times 10^{-1}$	$-1.261094 \times 10^0$	$-4.080800 \times 10^{-1}$
3	5	$-1.096578 \times 10^{-2}$	0	$-9.316772 \times 10^{-1}$	0
		$-7.920391 \times 10^{-1}$	0	$-1.852993 \times 10^0$	0
		$-1.997077 \times 10^{-1}$	0	$-3.049055 \times 10^0$	0
		$-1.686141 \times 10^0$	$1.291524 \times 10^0$	$-1.680029 \times 10^0$	$1.307535 \times 10^0$
		$-1.686141 \times 10^0$	$-1.291524 \times 10^0$	$-1.680029 \times 10^0$	$-1.307535 \times 10^0$
4	5	$3.742610 \times 10^{-1}$	0	$-1.975139 \times 10^0$	0
		$-2.148009 \times 10^0$	$1.917512 \times 10^0$	$-2.813927 \times 10^0$	$4.063061 \times 10^{-1}$
		$-2.148009 \times 10^0$	$-1.917512 \times 10^0$	$-2.813927 \times 10^0$	$-4.063061 \times 10^{-1}$
		$-1.976622 \times 10^0$	$2.208657 \times 10^0$	$-1.978586 \times 10^0$	$2.204506 \times 10^0$
		$-1.976622 \times 10^0$	$-2.208657 \times 10^0$	$-1.978586 \times 10^0$	$-2.204506 \times 10^0$

In Fig. 3.6 there are the time-domain comparisons of the two approximations along with their difference  $10\log_{10}|d_n|$  versus time. Since the accuracy of the VF

approximation is validated, now the next step is to apply it to the kernels that are needed for FETD-MNRBC simulations.

Firstly the comparison of  $U_n$  is performed. The comparison is held for order 0, 5, 10 and 15. This choice of orders was done because for the electrically small scatterers considered in this work, kernels up to order 15 are used. The exact function in frequency domain is compared with the VF approximation. In Fig. 3.7 there is the function and error comparison for these orders. The input parameters for VECTFIT are (i)  $f_{max}=10\text{Hz}$  ; (ii) 4000 samples; (ii) iter = 20 iterations; (iii) asympflag = 1 (as  $D_n = H_n = 0$ ) and (iv)  $M=10$  poles.

Next the comparison for  $G_n$  is performed. This is displayed in Fig. 3.8. The input parameters for VECTFIT are (i)  $f_{max}=3\text{GHz}$  ; (ii) 3000 samples; (ii) iter = 20 iterations; (iii) asympflag = 3 and (iv)  $M=10$  poles.

The comparison considered next is based on (3.21). VF is applied is applied to both  $U_n$  and  $G_n$  and  $U_n$  parameters are transformed thought (3.21) and then compared to  $G_n$  function approximation. The input parameters used in VECTFIT were: (i) 4000 frequency samples in both VF approximations; (b) a frequency range of  $0 \leq f \leq f_{max}$  with  $f_{max} = 10 \text{ Hz}$  for  $U_n$  and  $f_{max} = 10 \times c/\rho \text{ Hz}$  for  $G_n$ ; (c) iter = 20 iterations; and (d) asympflag = 1 for  $U_n$  and asympflag = 3 for  $G_n$ . Fig. 3.9 shows plots of the comparison of the errors of the two approximations of the function  $G_n$  for  $n=0, 5, 10, 15$  for  $\rho = 0.5\text{m}$ . Figs 3.10 and 3.11 show the same comparison but for  $\rho = 1\text{m}$  and  $\rho = 2\text{m}$  respectively. For the parameters chosen it can be observed that the error of the generic approach is similar or better than working with the original function  $G_n$ . Moreover using  $U_n$  has the advantage that the VF approximation does not need to be recalculated for different radiuses but the VF coefficient can be easily scaled through (3.21).



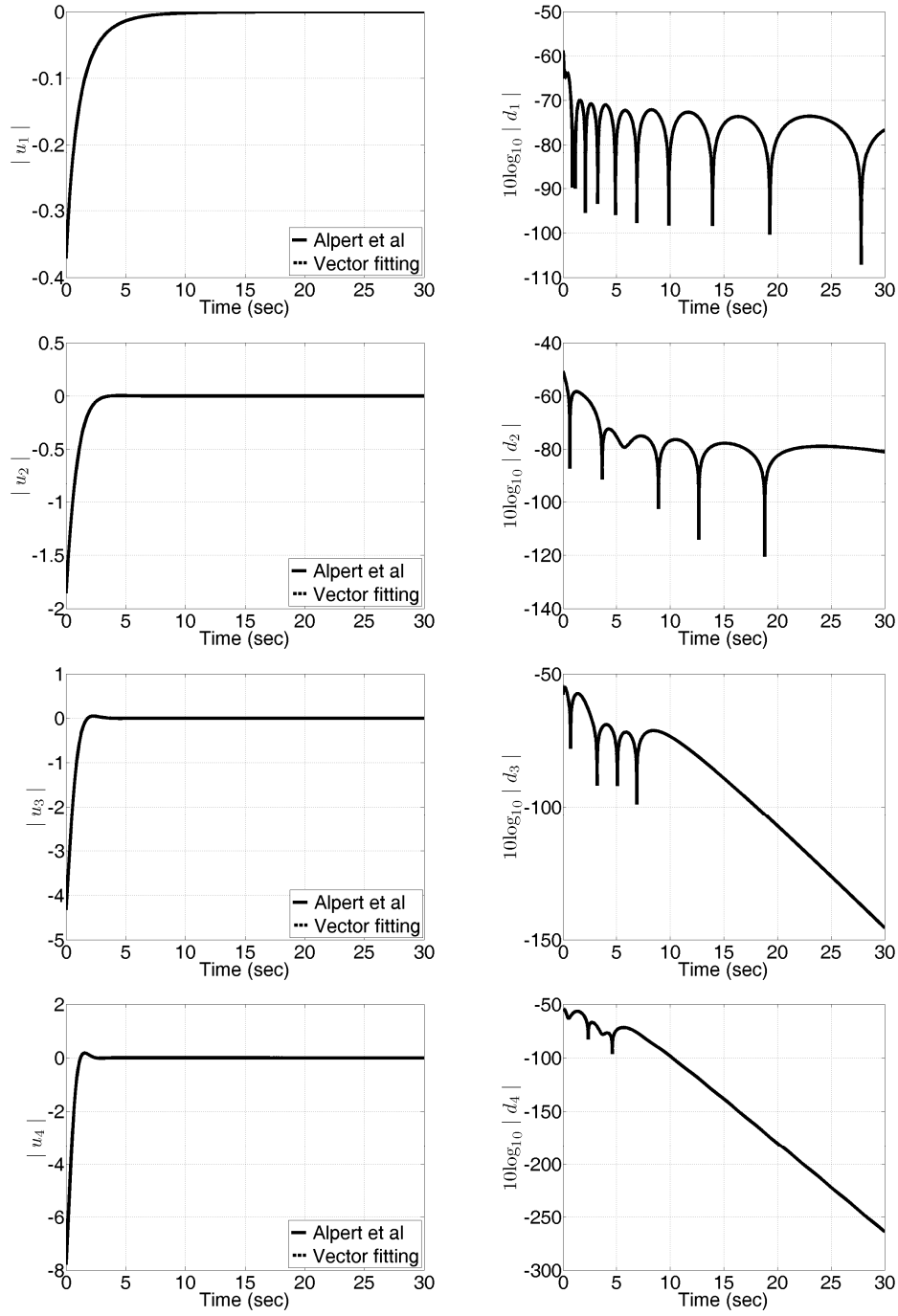


Fig 3.6 Plots of time domain functions and differences for  $n = 1, 2, 3, 4$

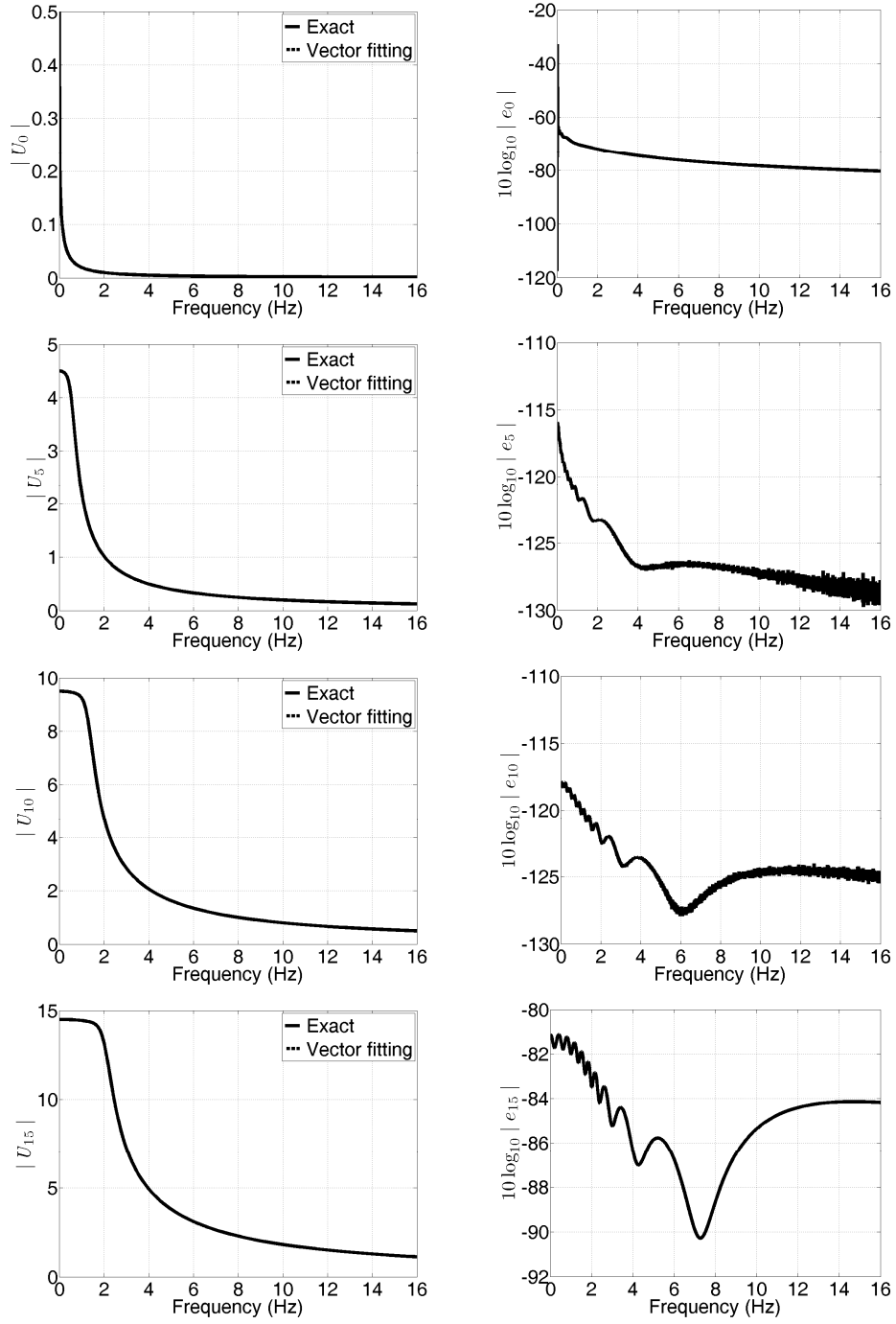
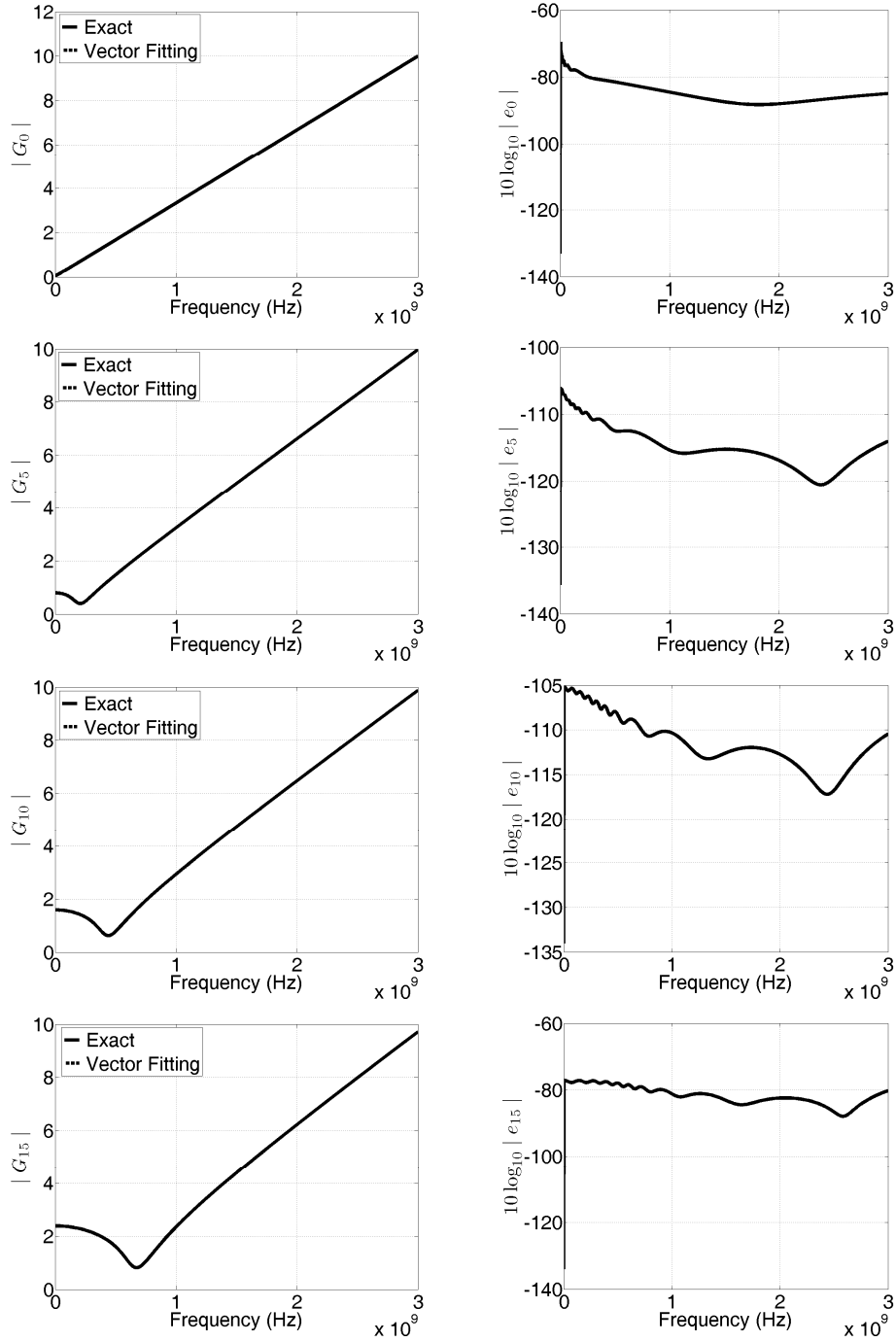


Fig 3.7 Plots of  $|U_n(s = j2\pi f)|$  and  $10 \log_{10} |e_n(s = j2\pi f)|$  versus frequency  $f$  for  $n = 0, 5, 10, 15$ .



3.8 Plots of  $|G_n(s = j2\pi f)|$  and  $10 \log_{10} |e_n(s = j2\pi f)|$  versus frequency  $f$  for  $n = 0, 5, 10, 15$ .

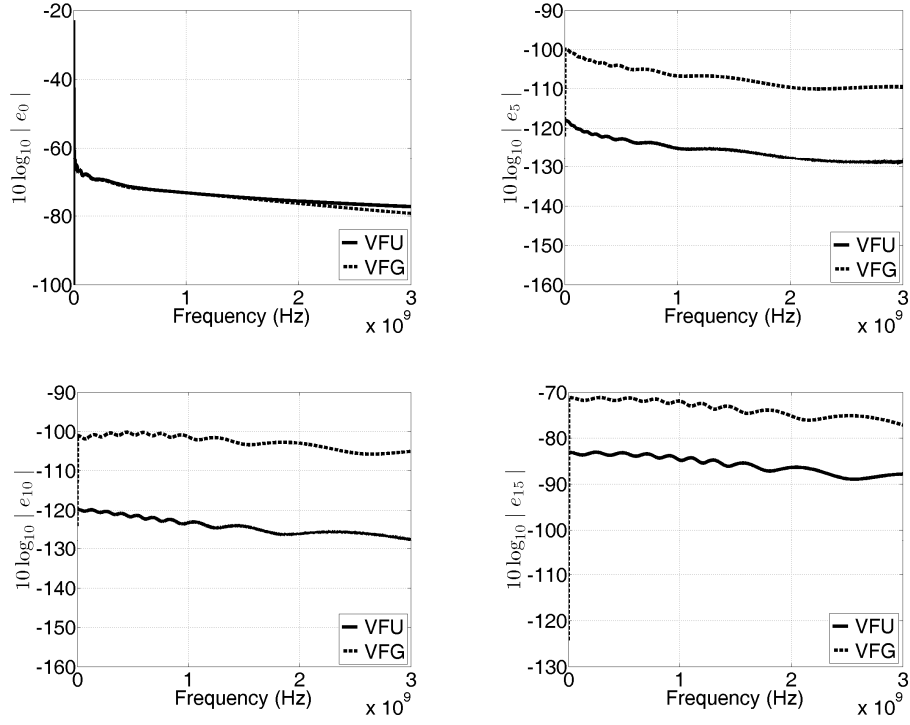


Fig. 3.9 Plots  $10\log_{10}|e_n(\omega)|$  versus frequency  $f$  for  $\rho = 0.5\text{m}$

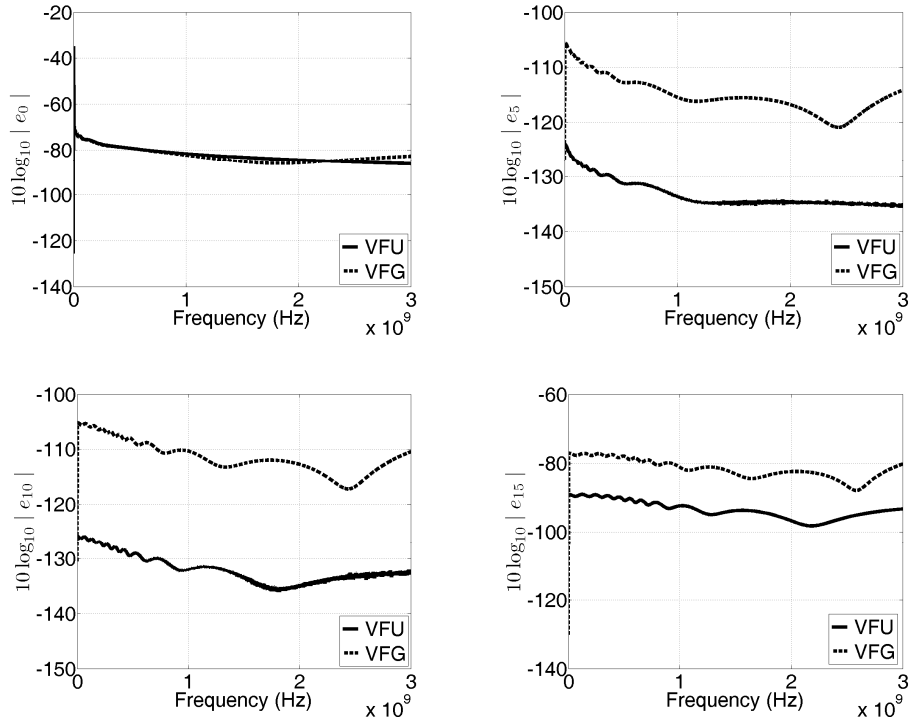


Fig. 3.10 Plots  $10\log_{10}|e_n(\omega)|$  versus frequency  $f$  for  $\rho = 1\text{m}$

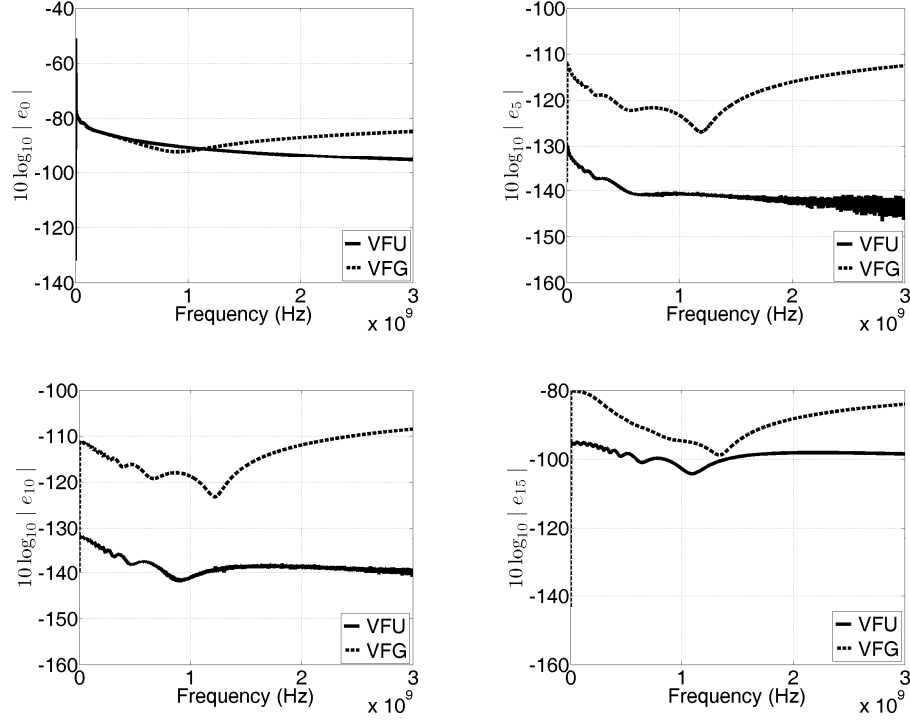


Fig. 3.11 Plots  $10\log_{10}|e_n(\omega)|$  versus frequency  $f$  for  $\rho = 2$  m

### 3.4.3 Effect on FEM accuracy

The last section of the results investigates the effect on the FEM accuracy of the two approaches. The approach where VF is applied directly to  $G_n$  function is called the VFG approach and the approach where VF is applied to  $U_n$  and the parameters are then transformed through (3.21), called the VFU approach. The two approaches are applied to FETD-MNRBC simulations of the previous chapter and the results for the BSW are compared. Two structures are considered; the circular and the triangular perfectly electrically conducting scatterers. For the circular the outer boundary is at 1m and for the triangular the outer boundary is at 1.5m. For the calculation of the error  $e_{BSW}$ , defined in (2.71), a reference solution is needed for each structure. For the circular scatterer this was the analytical solution and for the triangular the FEFD result was considered as reference since there was not an

analytical solution available. The comparison for the two structures for  $10\log_{10}|e_{BSW}|$  is depicted in Fig. 3.12. Due to the fact that the VFU approach is more accurate than VFG for higher orders as displayed in Fig. 3.9, Fig. 3.10 and Fig. 3.11, one could expect it to result to more accurate Bistatic scattering width results. Nevertheless as can be seen, for the electrically small cylindrical structures simulated in this work, the finite element method errors of VFG and VFU for the Bistatic scattering width are practically indistinguishable. Of course the VGU approach has the advantage that it is more versatile since there is no need to rerun it for each different value of the radius.

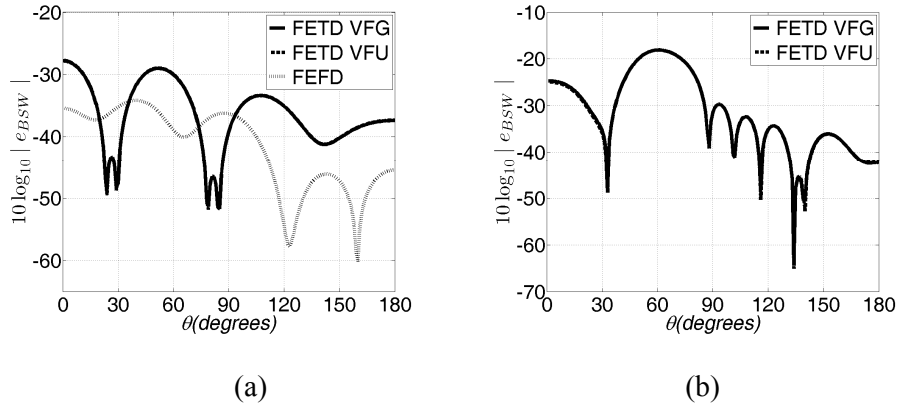


Fig 3.12 Comparison for the BSW (a) circular scatterer (b) triangular scatterer

### 3.5 Scientific contribution and future work

In this chapter partial fraction approximations of cylinder nonreflecting boundary kernels were presented. These approximations were obtained with the use of the publically available VECTFIT software. The VF approximation is easier and of comparable accuracy to other partial fraction approximations [9]. The advantages of working with the generic functions were also discussed. The ease and the accuracy of VF software make it a very useful tool for engineers.

VF approximation allowed the application of the FETD-MNRBC in cylindrical coordinates. An important advantage of the VF software is that it

expresses the kernel as a sum of exponentials which allows the time domain boundary integral to be calculated recursively. This recursive convolution [8] is more time efficient than the standard convolution [13]. This is of special importance in this case of cylindrical kernels since the exact form of the cylindrical kernels is not known. Thus with the use of the VF approximation the time domain boundary integral can not only be calculated but it is also calculated efficiently.

Finally the accuracy of the algorithm will be useful in Chapter 5 as well. There it will be applied to the incident field components of the periodic FETD-MNRBC. In the next chapter the generic approach of the boundary kernel will be utilized for the application of the total field FETD-MNRBC formulation.

## REFERENCES

- [1] B. Gustavsen, and A. Semlyen, "Rational Approximation of Frequency Domain Responses by Vector Fitting", *IEEE Trans. on Power Delivery*, vol. 14, no. 3, pp. 1052-1061, 1999.
- [2] K. Bavelis and C. Mias, "Vector fitting realisation of exact time domain modal nonreflecting boundary condition", *Electronic Letters*, vol. 46, no. 11. pp 760-761, 2010
- [3] K.M. Coperich, J. Morsey, A.C. Cangellaris and S.E. Ruehli, "Physically consistent transmission line models for high-speed interconnects in lossy dielectrics", *IEEE Trans. Advanced Packaging*, vol. 35, no. 2, pp. 129-135, May 2002.
- [4] I.M. Elfadel, H.-M. Huang, A.E. Ruehli, A. Dounavis and M.S. Nakhla, "A comparative study of two transient analysis algorithms for lossy transmission lines with frequency-dependent data", *IEEE Trans. Advanced Packaging*, vol. 25, no. 2, pp. 143-153, May 2002.
- [5] M. Abdel-Rahman, A. Semlyen and M.R. Iravani, "Two-layer network equivalent for electromagnetic transients", *IEEE Trans. Power Delivery*, vol. 18, no. 4, pp. 1328-1335, October 2003.
- [6] J.M. Griffith and M. Toupikov, "Time-domain modeling from S-parameters: applicable to hard-disk drives", *IEEE Trans. Magnetics*, vol. 39, no. 6, pp.3581-3586, Nov. 2003.
- [7] V.I. Okhmatovski and A.C. Cangellaris, "Evaluation of layered media Green's functions via rational function fitting", *IEEE Microwave Components Letters*, vol. 14, no. 1, Jan. 2004.



- [8] Y. Cai, and C. Mias, “Fast Finite Element Time Domain – Floquet Absorbing Boundary Condition modelling of periodic structures using recursive convolution”, *IEEE Trans. Antennas Propag.*, vol. 55, no. 9, pp. 2550-2558, 2007.
- [9] B. Alpert, L. Greengard, and T. Hagstrom, “Rapid evaluation of nonreflecting boundary kernels for time-domain wave propagation”, *SIAM J. Numer. Anal.*, vol. 37, no. 4, pp. 1138–1164, 2000.
- [10] <http://www.energy.sintef.no/Produkt/VECTFIT/index.asp>. Retrieved 21 April 2011.
- [11] M.L. Meade and C.R. Dillon, Signals and Systems Models and Behaviour, 2<sup>nd</sup> ed., Kluwer Academic Publishers, 2000.
- [12] M. Abramowitz and I.A. Stegun, Handbook of Mathematical Functions: With Formulas, Graphs, and Mathematical Tables, Dover Publications, New York, 1965.
- [13] Y. Cai and C. Mias, “Finite-element time-domain modelling of plane wave scattering by a periodic structure using an exact boundary condition”, *IET Microwaves, Antennas & Propagation*, vol. 1, no. 3, pp. 609-616, 2007.

## CHAPTER 4

### Total field FETD-MNRBC formulation

#### 4.1 Introduction

This chapter proceeds to the application of a vector fitting approximated cylindrical two dimensional MNRBC to total field formulation. The total field formulations are more general than the scattered field formulations derived in Chapter 2 but they also include more terms and are more difficult. Therefore it is easier for the reader to comprehend the formulations and follow the mathematical derivations if the scattered field ones have been studied earlier.

The scattered field that was derived in Chapter 2 is applicable only to PEC cylinders. The scattered field formulation can be extended to model dielectrics as shown in [1, 2]. This will be investigated in Chapter 6. Here for reasons of academic completeness the total field formulation will be derived and applied.

The geometric discretisation is performed with third order isoparametric surface (8-noded) and line (3-noded) elements as previously [3,4], thus the relevant analysis will not be repeated. Moreover in this chapter the analysis will be held for both TE and TM polarizations and results will be shown for both excitations.

This chapter initially shows the weighted residual FEFD total field formulation. The boundary considered is the cylindrical two dimensional MNRBC. Following that the FETD-MNRBC is presented. One significant difference with the scattered field formulation is that the FETD for total field formulation requires the calculation of a convolution integral of the boundary kernel for both the scattered and the incident wave. The next part is the presentation of the numerical results. The

cross-sections considered are the circular PEC cylinder from the previous chapter [5 p.607], a circular conductor surrounded with dielectric [6 p.666], a circular dielectric cylinder [6 pp.581-587] and two dielectric square cylinders of different dimensions [6 p. 611, p.570] and [7,8]. The PEC cylinder is used in order to highlight the fact that the total field formulation is a generalization of the analysis of the previous chapter. The last part presents the conclusions and future work and extension to the work done so far.

## 4.2 FEFD formulation and application of modal nonreflecting boundary condition

The Helmholtz equation in the dielectric material and in the free space surrounding the simulated cylindrical scatterer for the total field component is

$$\nabla \cdot \frac{1}{p_r} \nabla \tilde{\Phi}^t + k_0^2 q_r \tilde{\Phi}^t = 0 \quad (4.1)$$

Where  $p_r = \mu_r$ ,  $q_r = \epsilon_r$  for TE excitation and  $p_r = \epsilon_r$ ,  $q_r = \mu_r$  for TM excitation. The field component  $\Phi^t$  represents the total electric field component  $E_z$  for TE modes and the total magnetic field component  $H_z$  for TM modes. The parameters  $p_r$  and  $q_r$  have material dependent values in the dielectric and value equal to one in free space. The total field component will be the sum of the scattered and the incident field

$$\tilde{\Phi}^t = \tilde{\Phi}^{sc} + \tilde{\Phi}^{inc} \quad (4.2)$$

The weighted residual formulation of (4.1) is

$$R = \iint_{\Omega} W \left( \nabla \cdot \frac{1}{p_r} \nabla \tilde{\Phi}^t + k_0^2 q_r \tilde{\Phi}^t \right) d\Omega = 0 \quad (4.3)$$

And, after applying the vector identity of (2.9) and the divergence theorem, equation (4.3) becomes

$$R = \iint_{\Omega} \left[ (\nabla W \bullet \frac{1}{p_r} \nabla \tilde{\Phi}^t) - k_0^2 q_r \tilde{\Phi}^t \right] d\Omega - \oint_{\Gamma_s} \frac{1}{p_r} W \nabla \tilde{\Phi}^t \cdot \hat{n} d\Gamma = 0 \quad (4.4)$$

And since

$$\nabla \tilde{\Phi}^t \cdot \hat{n} = \frac{\partial \tilde{\Phi}^t}{\partial n} = \frac{\partial \tilde{\Phi}^t}{\partial \rho} \quad (4.5)$$

And  $p_r=1$  at the outer boundary for both polarizations, (4.4) becomes

$$R = \iint_{\Omega} \left( \frac{1}{p_r} \frac{\partial W}{\partial x} \frac{\partial \tilde{\Phi}^t}{\partial x} + \frac{1}{p_r} \frac{\partial W}{\partial y} \frac{\partial \tilde{\Phi}^t}{\partial y} - k_0^2 q_r W \tilde{\Phi}^t \right) dx dy - \int_{\Gamma_s} W \frac{\partial \tilde{\Phi}^t}{\partial \rho} d\Gamma = 0 \quad (4.6)$$

To apply the MNRBC in (4.6) a similar procedure as in Chapter 2 is followed. The scattered field at the outer boundary  $\Gamma_s$  of radius  $\rho_a$  (see Fig 2.1) will be (2.16)

$$\tilde{\Phi}^{sc}(x, y) \Big|_{\rho=\rho_a} = \tilde{\Phi}^{sc}(\rho_a, \phi) = \sum_{m=-\infty}^{\infty} A_m H_m^{(2)}(k_0 \rho_a) e^{jm\phi} \quad (4.7)$$

So the total field will be

$$\tilde{\Phi}^t(\rho_a, \phi) = \tilde{\Phi}^{inc}(\rho_a, \phi) + \tilde{\Phi}^{sc}(\rho_a, \phi) = \tilde{\Phi}^{inc}(\rho_a, \phi) + \sum_{m=-\infty}^{\infty} A_m H_m^{(2)}(k_0 \rho_a) e^{jm\phi} \quad (4.8)$$

Or

$$\tilde{\Phi}^t(\rho_a, \phi) - \tilde{\Phi}^{inc}(\rho_a, \phi) = \sum_{m=-\infty}^{\infty} A_m H_m^{(2)}(k_0 \rho_a) e^{jm\phi} \quad (4.9)$$

And, by following the same orthogonalization procedure as in (3.11)-(3.13), results in

$$A_n = \frac{\oint_{\Gamma_s} (\tilde{\Phi}^t(\rho_a, \phi) - \tilde{\Phi}^{inc}(\rho_a, \phi)) e^{-jn\phi} d\Gamma}{2\pi \rho_a H_n^{(2)}(k_0 \rho_a)} \quad (4.10)$$

The derivative of (4.8) with respect to  $\rho$  at  $\rho = \rho_a$  is

$$\frac{\partial \tilde{\Phi}^t(\rho, \phi)}{\partial \rho} \Big|_{\rho=\rho_a} = \frac{\partial \tilde{\Phi}^{inc}(\rho, \phi)}{\partial \rho} \Big|_{\rho=\rho_a} + \sum_{n=-\infty}^{\infty} A_n \left( \frac{\partial H_n^{(2)}(k_0 \rho)}{\partial \rho} \right) e^{jn\phi} \Big|_{\rho=\rho_a} \quad (4.11)$$

By replacing (4.10) and (4.11) in the boundary integral of (4.6), it becomes

$$\begin{aligned}
& \left. \int_{\Gamma_s} W \frac{\partial \tilde{\Phi}^t}{\partial \rho} d\Gamma \right|_{\rho=\rho_a} = \left. \int_{\Gamma_s} W \frac{\partial \tilde{\Phi}^{inc}}{\partial \rho} d\Gamma \right|_{\rho=\rho_a} \\
& + \sum_{n=-\infty}^{\infty} W \frac{\oint_{\Gamma_s} (\tilde{\Phi}^t(\rho_a, \phi) - \tilde{\Phi}^{inc}(\rho_a, \phi)) e^{-jn\phi}}{2\pi\rho_a H_n^{(2)}(k_0\rho_a)} \left( \frac{\partial H_n^{(2)}(k_0\rho)}{\partial \rho} \right) e^{jn\phi} \Bigg|_{\rho=\rho_a} d\Gamma
\end{aligned} \tag{4.12}$$

$$\begin{aligned}
& \left. \int_{\Gamma_s} W \frac{\partial \tilde{\Phi}^t}{\partial \rho} d\Gamma \right|_{\rho=\rho_a} = \left. \int_{\Gamma_s} W \frac{\partial \tilde{\Phi}^{inc}}{\partial \rho} d\Gamma \right|_{\rho=\rho_a} \\
& + \sum_{n=-\infty}^{\infty} G_n(\omega) \oint_{\Gamma_s} W e^{jn\phi} d\Gamma \oint_{\Gamma_s} \tilde{\Phi}^t(\rho_a, \phi) e^{-jn\phi} d\Gamma \\
& - \sum_{n=-\infty}^{\infty} G_n(\omega) \oint_{\Gamma_s} W e^{jn\phi} d\Gamma \oint_{\Gamma_s} \tilde{\Phi}^{inc}(\rho_a, \phi) e^{-jn\phi} d\Gamma
\end{aligned} \tag{4.13}$$

where  $G_n$  is the same as in (2.24).

Assuming incidence along the  $-x$  direction, the incident wave, is given by:

$$\tilde{\Phi}^{inc}(x) = \Phi_o e^{jk_0 x} = \Phi_o e^{jk_0 \rho \cos \phi} \tag{4.14}$$

The derivative with respect to  $\rho$  is

$$\frac{\partial \tilde{\Phi}^{inc}}{\partial \rho} = \Phi_o e^{jk_0 \rho \cos \phi} jk_0 \cos \phi = \tilde{\Phi}^{inc} jk_0 \cos \phi \tag{4.15}$$

By replacing (4.15) to (4.13) the boundary integral yields to

$$\begin{aligned}
& \left. \int_{\Gamma_s} W \frac{\partial \tilde{\Phi}^t}{\partial \rho} d\Gamma \right|_{\rho=\rho_a} = \left. \int_{\Gamma_s} W \tilde{\Phi}^{inc} jk_0 \cos \phi d\Gamma \right|_{\rho=\rho_a} \\
& + \sum_{n=-\infty}^{\infty} G_n(\omega) \oint_{\Gamma_s} W e^{jn\phi} d\Gamma \oint_{\Gamma_s} \tilde{\Phi}^t(\rho_a, \phi) e^{-jn\phi} d\Gamma \\
& - \sum_{n=-\infty}^{\infty} G_n(\omega) \oint_{\Gamma_s} W e^{jn\phi} d\Gamma \oint_{\Gamma_s} \tilde{\Phi}^{inc}(\rho_a, \phi) e^{-jn\phi} d\Gamma
\end{aligned} \tag{4.16}$$

By combining (4.6) and (4.16)

$$\begin{aligned}
R = & \iint_{\Omega} \left( \frac{1}{p_r} \frac{\partial W}{\partial x} \frac{\partial \tilde{\Phi}^t}{\partial x} + \frac{1}{p_r} \frac{\partial W}{\partial y} \frac{\partial \tilde{\Phi}^t}{\partial y} - k_0^2 q_r W \tilde{\Phi}^t \right) dx dy - \int_{\Gamma_s} W \tilde{\Phi}^{inc} j k_0 \cos \phi d\Gamma \Big|_{\rho=\rho_a} \\
& - \sum_{n=-\infty}^{\infty} G_n(\omega) \oint_{\Gamma_s} W e^{jn\phi} d\Gamma \oint_{\Gamma_s} \tilde{\Phi}^t(\rho_a, \phi) e^{-jn\phi} d\Gamma \\
& + \sum_{n=-\infty}^{\infty} G_n(\omega) \oint_{\Gamma_s} W e^{jn\phi} d\Gamma \oint_{\Gamma_s} \tilde{\Phi}^{inc}(\rho_a, \phi) e^{-jn\phi} d\Gamma = 0
\end{aligned} \tag{4.17}$$

And by separating the total field components to the left hand side and the incident ones to the right hand side

$$\begin{aligned}
& \iint_{\Omega} \left( \frac{1}{p_r} \frac{\partial W}{\partial x} \frac{\partial \tilde{\Phi}^t}{\partial x} + \frac{1}{p_r} \frac{\partial W}{\partial y} \frac{\partial \tilde{\Phi}^t}{\partial y} - k_0^2 q_r W \tilde{\Phi}^t \right) dx dy \\
& - \sum_{n=-\infty}^{\infty} G_n(\omega) \oint_{\Gamma_s} W e^{jn\phi} d\Gamma \oint_{\Gamma_s} \tilde{\Phi}^t(\rho_a, \phi) e^{-jn\phi} d\Gamma = \int_{\Gamma_s} W \tilde{\Phi}^{inc} j k_0 \cos \phi d\Gamma \Big|_{\rho=\rho_a} \\
& - \sum_{n=-\infty}^{\infty} G_n(\omega) \oint_{\Gamma_s} W e^{jn\phi} d\Gamma \oint_{\Gamma_s} \tilde{\Phi}^{inc}(\rho_a, \phi) e^{-jn\phi} d\Gamma
\end{aligned} \tag{4.18}$$

The next step is to discretize (4.18) with 8-noded isoparametric curvilinear quadrilateral elements for the surface and 3-noded isoparametric curvilinear line elements for the boundary as described in Chapter 2. The discretised version of (4.18) is

$$\underbrace{[ [\mathbf{S}_{p_r}^{\Omega}] - k_0^2 [\mathbf{T}_{q_r}^{\Omega}] + [\mathbf{P}^{\Gamma}] ]}_{[\mathbf{M}_{p_r, q_r}^{\Omega, \Gamma}]} \{ \tilde{\Phi}^t \} = \underbrace{[ [\mathbf{O}^{\Gamma}] - [\mathbf{P}^{\Gamma}] ]}_{[\mathbf{M}^{\Omega, \Gamma}]} \{ \tilde{\Phi}^{inc} \} \tag{4.19}$$

Or

$$[\mathbf{M}_{p_r, q_r}^{\Omega, \Gamma}] \{ \tilde{\Phi}^t \} = \{ \mathbf{d} \} \tag{4.20}$$

Matrices  $[\mathbf{S}_{p_r}^{\Omega}]$ ,  $[\mathbf{T}_{p_r}^{\Omega}]$  apart from the material dependency are the same as in the scattered field formulation and are described in Appendix C.  $[\mathbf{P}^{\Gamma}]$  is the same as in Chapter 2 since the outer boundary is in the free space which surrounds the cylindrical structure. The entries for the matrix  $[\mathbf{O}^{\Gamma}]$  will be

$$\begin{aligned}
O_{ij}^k &= \int_{\Gamma^k} N_i^k(u) N_j^k(u) jk_0 \cos \phi d\Gamma = \int_{-1}^1 N_i^k(u) N_j^k(u) jk_0 \cos \phi J_s^k du \\
&= \int_{-1}^1 N_i^k(u) N_j^k(u) jk_0 \cos \left( \sin^{-1} \left( \frac{1}{\rho_a} \sum_{p=1}^3 N_p(u) y_p^k \right) \right) J_s^k du
\end{aligned} \tag{4.21}$$

All the parameters in (4.21) are the same as in Chapter 2. The integrations of (4.21) are performed numerically using the 5-point Gaussian quadrature formula [3 pp. 290-291], and its final form is given in Appendix C. The right hand side square matrix  $[\mathbf{M}^{\Omega, \Gamma}]$  in (4.19) is initially set to zero and subsequently assembled with the entries from  $[\mathbf{O}^\Gamma]$  and  $[\mathbf{P}^\Gamma]$ . The vector matrix  $\{\tilde{\Phi}^t\}$  is the unknown node field components and  $\{\tilde{\Phi}^{inc}\}$  is the incident field values and it has nonzero values only for the outer boundary nodes which are given by (4.14). Equation (4.20) is solved for the studied frequency using subroutine ME28 from the Harwell Subroutine Library. For the simulation of dielectrics, the appropriate values of  $p_r$  and  $q_r$  should be assigned for each element that constitutes the dielectric and thus find the correct values for matrices  $[\mathbf{S}_{p_r}^\Omega]$ ,  $[\mathbf{T}_{p_r}^\Omega]$ . At the interface between the two media the field satisfies the continuity conditions [9]. In case there is a perfectly electric or magnetic conductive part in TE or TM polarization respectively in the simulated structure, the total field at the corresponding nodes is set to zero and applied as a Dirichlet boundary condition [9] to (4.20).

### 4.3 FETD formulation and application of modal nonreflecting boundary condition

After the inversion to time domain was presented for the scattered field formulation, the inversion of the total field formulation is straightforward, so only some key equations and important points will be now highlighted.

In time domain the Helmholtz equation (4.1) will be written as

$$\nabla \cdot \frac{1}{p_r} \nabla \Phi' - \frac{q_r}{c^2} \frac{\partial^2 \Phi'}{\partial t^2} = 0 \quad (4.22)$$

Similarly the weighted residual formulation of (4.6) will be

$$R = \iint_{\Omega} \left( \nabla W \bullet \frac{1}{p_r} \nabla \Phi' + \frac{q_r}{c^2} W \frac{\partial^2 \Phi'}{\partial t^2} \right) d\Omega - \oint_{\Gamma_s} W \frac{\partial \Phi'}{\partial \rho} d\Gamma = 0 \quad (4.23)$$

the boundary integral of (4.23) includes the derivative of the incident field with respect to  $\rho$  (4.15). Equation (4.15) can be rewritten

$$\frac{\partial \tilde{\Phi}^{inc}}{\partial \rho} = \tilde{\Phi}^{inc} j k_0 \cos \phi = j \omega \tilde{\Phi}^{inc} \frac{\cos \phi}{c} \quad (4.24)$$

And in the time domain (4.24) will be

$$\frac{\partial \tilde{\Phi}^{inc}}{\partial \rho} = \frac{\partial \tilde{\Phi}^{inc}}{\partial t} \frac{\cos \phi}{c} \quad (4.25)$$

Now ILT can be applied to the boundary integral of (4.16), and it will be

$$\begin{aligned} \int_{\Gamma_s} W \frac{\partial \Phi'}{\partial \rho} d\Gamma \Big|_{\rho=\rho_a} &= \int_{\Gamma_s} W \frac{\partial \Phi^{inc}}{\partial t} \frac{\cos \phi}{c} d\Gamma \Big|_{\rho=\rho_a} \\ &+ \sum_{n=-\infty}^{\infty} \oint_{\Gamma_s} W e^{jn\phi} d\Gamma \left( g_n(t) * \oint_{\Gamma_s} \Phi'(t, \rho_a, \phi) e^{-jn\phi} d\Gamma \right) \\ &- \sum_{n=-\infty}^{\infty} \oint_{\Gamma_s} W e^{jn\phi} d\Gamma \left( g_n(t) * \oint_{\Gamma_s} \Phi^{inc}(t, \rho_a, \phi) e^{-jn\phi} d\Gamma \right) \end{aligned} \quad (4.26)$$

After the geometric discretisation the global matrix system will be

$$[\mathbf{S}_{p_r}^{\Omega}] \{\Phi'\} + \frac{1}{c^2} [\mathbf{T}_{q_r}^{\Omega}] \frac{d^2 \{\Phi'\}}{dt^2} + [\Psi^{\Gamma}(t)] * \{\Phi'\} = [\Psi^{\Gamma}(t)] * \{\Phi^{inc}\} + [\Pi^{\Gamma}] \frac{d \{\Phi^{inc}\}}{dt} \quad (4.27)$$

The entries of  $[\Psi^{\Gamma}]$  are given by (2.43). The entries of  $[\Pi^{\Gamma}]$  will be

$$\Pi_{ij}^k = \int_{\Gamma^k} N_i^k(u) N_j^k(u) \frac{\cos \phi}{c} d\Gamma \quad (4.28)$$

And will be calculated following the same procedure as for matrix  $[\mathbf{O}^{\Gamma}]$ . The convolution term for the total field component of (4.27) will be



$$[\Psi^\Gamma(t)] * \{\Phi^t\} = [\mathbf{Q}^\Gamma] \{\Phi^t\} + [\mathbf{V}^\Gamma] \frac{d\{\Phi^t\}}{dt} + \{\mathbf{D}^{\Gamma,t}(t)\} \quad (4.29)$$

And for the incident field component

$$[\Psi^\Gamma(t)] * \{\Phi^{inc}\} = [\mathbf{Q}^\Gamma] \{\Phi^{inc}\} + [\mathbf{V}^\Gamma] \frac{d\{\Phi^{inc}\}}{dt} + \{\mathbf{D}^{\Gamma,inc}(t)\} \quad (4.30)$$

Where the entries for  $[\mathbf{Q}^\Gamma]$ ,  $[\mathbf{V}^\Gamma]$  are given in (2.48), (2.49) and the entries for the  $\{\mathbf{D}^\Gamma(t)\}$  matrices will be

$$D_i^{kl,e,t}(t) = -\sum_j \sum_{n=-\infty}^{\infty} B_{n,i}^k C_{n,j}^l \sum_{m=1}^M R_{m,n,j}^t(t) \quad (4.31)$$

$$R_{m,n,j}^t(t) = r_{m,n} e^{a_{m,n}t} * \Phi_j^t(t) = \int_0^t r_{m,n} e^{a_{m,n}(t-\tau)} \Phi_j^t(\tau) d\tau \quad (4.32)$$

and

$$D_i^{kl,e,inc}(t) = -\sum_j \sum_{n=-\infty}^{\infty} B_{n,i}^k C_{n,j}^l \sum_{m=1}^M R_{m,n,j}^{inc}(t) \quad (4.33)$$

$$R_{m,n,j}^{inc}(t) = r_{m,n} e^{a_{m,n}t} * \Phi_j^{inc}(t) = \int_0^t r_{m,n} e^{a_{m,n}(t-\tau)} \Phi_j^{inc}(\tau) d\tau \quad (4.34)$$

Therefore (4.27) can be rewritten as

$$\begin{aligned} & [\mathbf{S}_{p_r}^\Omega + \mathbf{Q}^\Gamma] \{\Phi^t\} + [\mathbf{V}^\Gamma] \frac{d\{\Phi^t\}}{dt} + \frac{1}{c^2} [\mathbf{T}_{q_r}^\Omega] \frac{d^2\{\Phi^t\}}{dt^2} + \{\mathbf{D}^{\Gamma,t}(t)\} \\ & = [\mathbf{Q}^\Gamma] \{\Phi^{inc}\} + [\mathbf{V}^\Gamma + \mathbf{\Pi}^\Gamma] \frac{d\{\Phi^{inc}\}}{dt} + \{\mathbf{D}^{\Gamma,inc}(t)\} \end{aligned} \quad (4.35)$$

The next step is the time discretisation of (4.35) at  $t = q \Delta t$  where  $q$  is the current time step number. The derivatives of both fields of (4.35) are calculated by (2.54)-(2.56) and the convolutions are calculated recursively as in (2.51).

Following time discretisation (4.35) finally becomes

$$[\mathbf{K}^{\Omega,\Gamma}] \{\Phi^t\}^{q+1} = \{\mathbf{c}\} \quad (4.36)$$

where

$$\begin{aligned} \{\mathbf{c}\} = & [\mathbf{L}_1^{\Omega,\Gamma}] \{\Phi^t\}^q - [\mathbf{L}_2^{\Omega,\Gamma}] \{\Phi^t\}^{q-1} - \{\mathbf{D}^{\Gamma,t}\}^q \\ & + [\mathbf{N}_1^\Gamma] \{\Phi^{inc}\}^{q+1} + [\mathbf{N}_2^\Gamma] \{\Phi^{inc}\}^{q+1} + [\mathbf{N}_3^\Gamma] \{\Phi^{inc}\}^{q+1} + \{\mathbf{D}^{\Gamma,inc}\}^q \end{aligned} \quad (4.37)$$

and

$$[\mathbf{N}_1^\Gamma] = \frac{1}{2\Delta t} [\mathbf{V}^\Gamma] + \frac{1}{4} [\mathbf{Q}^\Gamma] + \frac{1}{2\Delta t} [\mathbf{\Pi}^\Gamma] \quad (4.38)$$

$$[\mathbf{N}_2^\Gamma] = \frac{1}{2} [\mathbf{Q}^\Gamma] \quad (4.39)$$

$$[\mathbf{N}_3^\Gamma] = -\frac{1}{2\Delta t} [\mathbf{V}^\Gamma] + \frac{1}{4} [\mathbf{Q}^\Gamma] - \frac{1}{2\Delta t} [\mathbf{\Pi}^\Gamma] \quad (4.40)$$

And  $[\mathbf{K}^{\Omega,\Gamma}]$ ,  $[\mathbf{L}_1^{\Omega,\Gamma}]$  and  $[\mathbf{L}_2^{\Omega,\Gamma}]$  are given by (2.59)-(2.61).

All the matrices are real. The matrices  $[\mathbf{K}^{\Omega,\Gamma}]$ ,  $[\mathbf{L}_1^{\Omega,\Gamma}]$ ,  $[\mathbf{L}_2^{\Omega,\Gamma}]$ ,  $[\mathbf{N}_1^\Gamma]$ ,  $[\mathbf{N}_2^\Gamma]$ ,  $[\mathbf{N}_3^\Gamma]$  are created once. The vectors  $\{\mathbf{D}^{\Gamma,t}\}^q$ ,  $\{\mathbf{D}^{\Gamma,inc}\}^q$ ,  $\{\Phi_z^t\}^q$ ,  $\{\Phi_z^t\}^{q-1}$ ,  $\{\Phi_z^{inc}\}^{q+1}$ ,  $\{\Phi_z^{inc}\}^q$ ,  $\{\Phi_z^{inc}\}^{q-1}$  are updated in each timestep. Again the matrix  $[\mathbf{K}^{\Omega,\Gamma}]$  is time invariant and (4.36) is solved in each timestep with subroutine MA28 from Harwell Subroutine Library. The time domain waveform of the incident field is a Gaussian modulated sinusoidal pulse. A sinusoidal signal modulated with a Gaussian pulse has the advantage that its width is limited in time domain and its bandwidth is limited in frequency domain [10,11]. The pulse used, at time step  $q$  is described by

$$\Phi^{inc}(q\Delta t) = \Phi_0 \exp\left[-\frac{(q - q_0 + \frac{x}{c\Delta t})^2}{2W^2}\right] \sin[2\pi f_c \Delta t (q - q_0 + \frac{x}{c\Delta t})] \quad (4.41)$$

This pulse covers a band of frequencies and not a single one, but after the application of Fourier Transform with the iterative algorithm of [12] the response at the specific frequency of interest will be found. It is easy from (4.41) to calculate the values of  $\{\Phi_z^{inc}\}^{q+1}$ ,  $\{\Phi_z^{inc}\}^q$ ,  $\{\Phi_z^{inc}\}^{q-1}$  for each timestep. As in the frequency domain formulation at the nodes that describe perfect electric or magnetic conductors the total field is set to zero and a Dirichlet boundary condition is applied.

#### 4.4 Numerical Results

This section presents the numerical results of the application of total field formulation to FEFD-MNRBC and FETD-MNRBC simulations. Five different cylindrical structures are considered. The cross-sections of these structures are (a) a PEC circular cylinder of radius  $0.5\lambda$  which was also simulated in the previous chapter, (b) a PEC circular cylinder of radius  $0.4\lambda$  which is surrounded by a dielectric layer of  $0.1\lambda$ , (c) a circular dielectric cylinder of radius  $0.5\lambda$ , (d) a square dielectric cylinder with side length  $d=0.25\lambda$  and (e) a square dielectric cylinder with side length  $d=0.5\lambda$ . For the first two structures TE polarization is considered and for the last three both TE and TM polarizations are considered. The material properties and all the important parameters for each structure are presented in Table 4.1.

The results are shown in terms of bistatic scattering width and (2.63) was used to calculate it. The terms  $A_n$  are found from (4.10) which means that the incident field must be subtracted from the total in order to find the needed terms for the bistatic scattering width. As previously, the iterative algorithm of [12 pp. 21-22] was used to transform the time domain fields to their frequency domain equivalents, and in all cases it was  $-N \leq n \leq N$ , where  $n$  is the order of the functions  $G_n$  and  $g_n$  used in the summations of (4.16) and (4.26) and  $N = 15$ . In this chapter, for the approximation of the boundary kernel, the Vector Fitting [13] approximation VFU was used which was described in the previous chapter. The input parameters used in VECTFIT were: (i)  $f_{max}=10\text{Hz}$ ; (ii) 4000 frequency samples; (iii) iter = 20 iterations; (iv) asympflag = 1 (as  $D_n = H_n = 0$ ) and (v)  $M=10$  poles.

**Table 4.1**

Simulation parameters

Parameters	Geometry (cross-section)				
	Circular	Circular	Circular	Square [6]	Square [7]
Material	PEC	PEC and dielectric	Dielectric	Dielectric	Dielectric
Relative permittivity $\epsilon_r$	-	2	2	2	4
Relative permeability $\mu_r$	-	2	1	1	1
Elements (nodes)	360 (1160)	280 (920)	300 (941)	132 (421)	340 (1061)
$\Delta s$ min. $^{*\dagger}$ (mm) Free space	27.778	39.26	39.26	20.833	25
$\Delta s$ min. $^{*\dagger}$ (mm) dielectric	-	25	39.26	20.833	25
$\Delta s$ max. $^{*\dagger}$ (mm) Free space	78.520	78.520	78.520	65.403	78.520
$\Delta s$ max. $^{*\dagger}$ (mm) dielectric	-	39.26	53.874	20.833	25
Courant limit $^\dagger$ (ps) free space	65.473	92.536	92.536	49.105	58.925
Courant limit $^\dagger$ (ps) dielectric	-	29.463	65.433	34.722	29.463
$f_{max}^+$ (GHz)	0.451	0.451	0.451	0.558	0.451
Nyquist criterion (ps) $^\S$	1109.6	1109.6	1109.6	895.763	1109.6
$\Delta t$ (ps)	40	20	40	10	20
$E_0$ (V/m)	1.0	1.0	1.0	1.0	1.0
$q_0$ ( $\Delta t$ )	700	1500	700	1500	1500
$W$ ( $\Delta t$ )	150	300	150	350	300

$\rho_\alpha(\lambda)^*$	1.0	1.0	1.0	0.5	1.0
$f_c$ (GHz)	0.3	0.3	0.3	0.3	0.3
Number of time steps	3000	6000	3000	8000	7000
Computing Time (s)**	901.546	1549.796	812.234	721.593	1969.625
<sup>+</sup> frequency ( $>f_c$ ) at which the incident field spectral amplitude is $10^{-7} \times$ (spectral amplitude at $f_c$ ); *at $\lambda = 1$ m; ** for the FETD-MNRBC method; <sup>§</sup> $\Delta t \leq 0.5/f_{max}$ ; <sup>‡</sup> $\Delta s$ = distance between consecutive nodes in a finite element, $\Delta s \leq 0.125c/f_{max} = 83.2\text{mm}$ ; <sup>†</sup> $\Delta t \leq \Delta s/(c\sqrt{2})$ adapted from [14].					

Fig. 4.1 shows the way the angle  $\theta$  is defined for the three circular cross-sections along with the meshes used. Angle  $\theta$  is defined as shown in Fig.4.1 in order to be able to compare the results of this work with the reference solutions of [5,6]. In [5,6] it is assumed that the incident wave is travelling along the  $+x$  direction while in this work it is assumed that the incident wave is travelling along the  $-x$  direction, as depicted in Fig.1.1. Fig. 4.2 displays the comparison for the PEC cylinder of the FEFD and FETD simulations with the analytical solution which was obtained from [5 607]. Figs 4.3 and 4.4 show the comparison for the other two circular cylinders. Again the comparison is held against the analytical which was obtained from [6 p.666] for the PEC cylinder surrounded with dielectric and [6 p.587] for the dielectric cylinder for TE excitation. For the TM excitation by using the duality of TE and TM modes [6 p.598] the analytical solution can be derived from the one for the TE modes by changing places between the permittivity and permeability and electric with magnetic field.

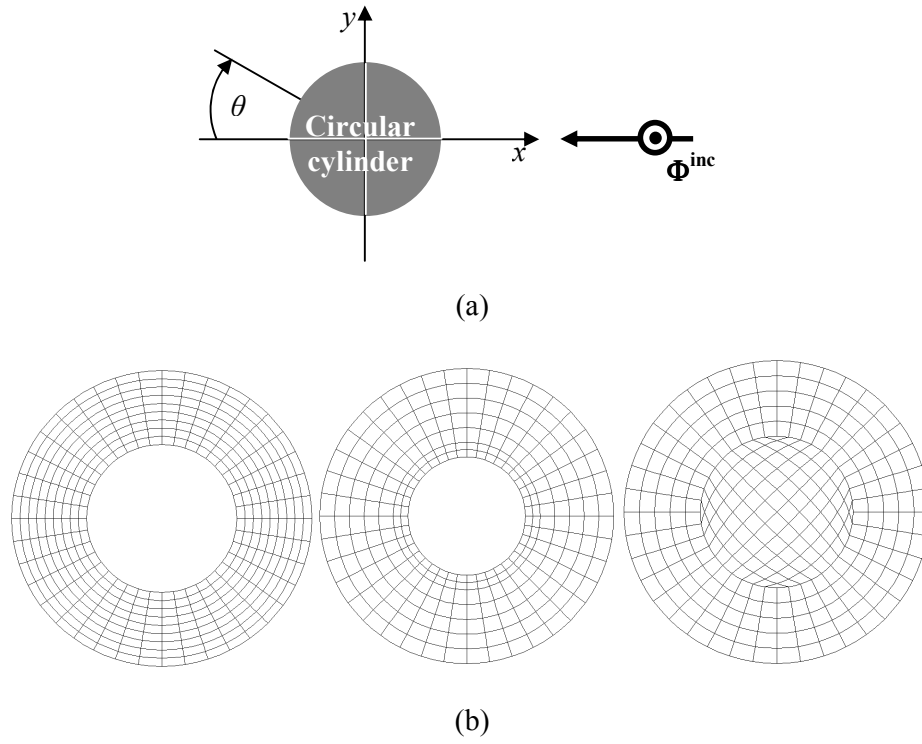


Fig. 4.1. (a) Circular cylinders geometry (b) FE meshes

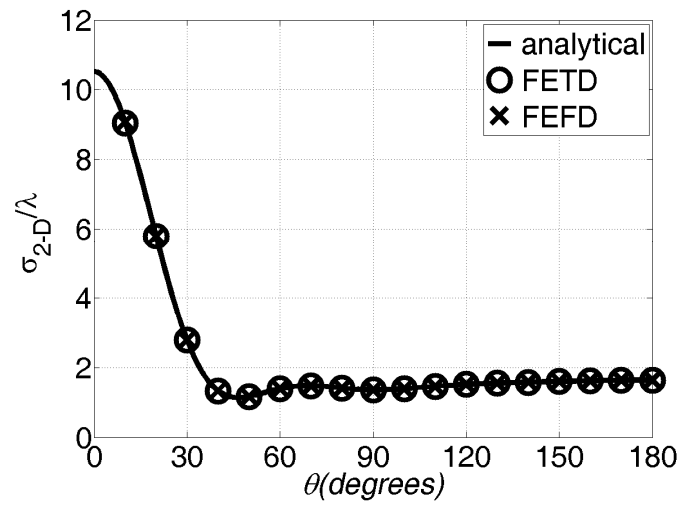


Fig. 4.2. Bistatic scattering width normalized with  $\lambda$  of the PEC circular scatterer,  $\theta = \pi - \phi$ .

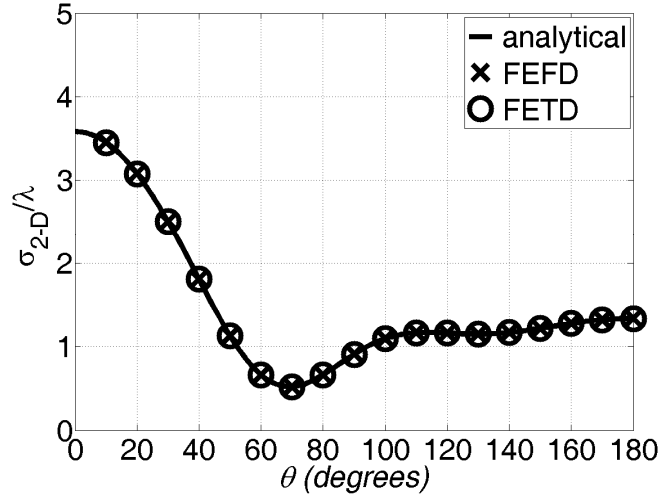


Fig. 4.3. Bistatic scattering width normalized with  $\lambda$  of the PEC circular scatterer surrounded with dielectric,  $\theta=\pi-\phi$ .

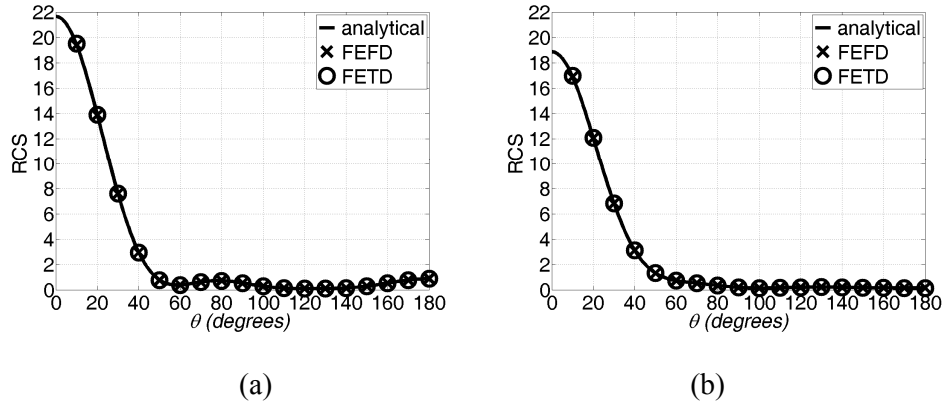


Fig. 4.4. Bistatic scattering width normalized with  $\lambda$  of the dielectric circular scatterer for TE (a) and TM (b) polarization,  $\theta=\pi-\phi$ .

The next part of the results is the square scatterers. Figure 4.5 shows the first square cylinder's geometry and its mesh. The FEFD and FETD results are compared with [6 p.570] and [6 p.611] for the TE and TM polarization respectively and this comparison is shown in Fig. 4.6. Lastly in Fig. 4.7 the geometry and the mesh for the second square cylinder is depicted. This scatterer is studied in [7, 8]. As a reference

for the comparison of Fig. 4.8 the results from the Boundary Value approach of [7] were used. In these case the FEFD-MNRBC and FETD-MNRBC results were practically indistinguishable.

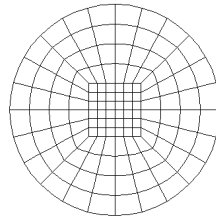
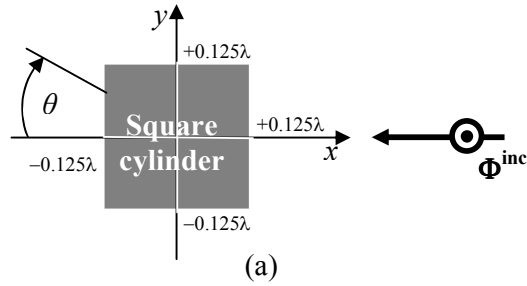


Fig. 4.5. (a) Square cylinder geometry (b) FE mesh

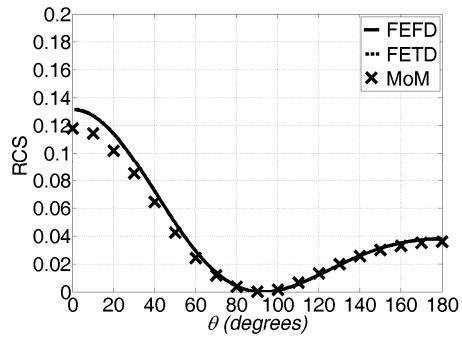
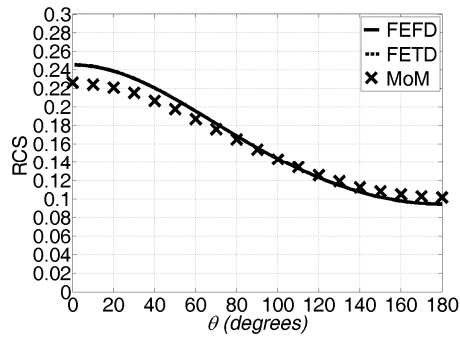
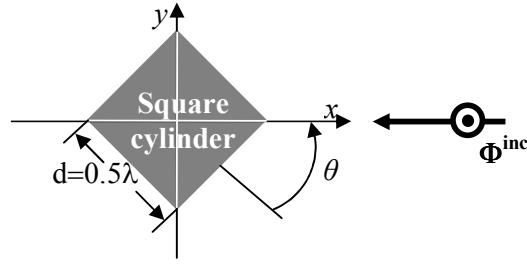
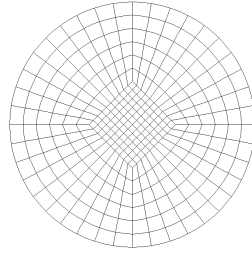


Fig. 4.6. Bistatic scattering width normalized with  $\lambda$  of the dielectric square scatterer [6] for TE (a) and TM (b) polarization,  $\theta = \pi - \phi$ .



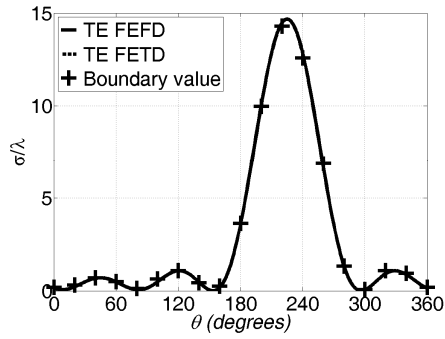


(a)

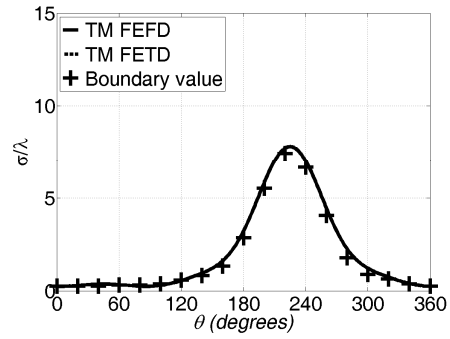


(b)

Fig. 4.7. (a) Square cylinder geometry (b) FE mesh



(a)



(b)

Fig. 4.8. Bistatic scattering width normalized with  $\lambda$  of the dielectric square scatterer [7] for TE (a) and TM (b) polarization,  $\theta = \phi + \pi/4$

## 4.5 Scientific contribution and future work

In this chapter for the first time the total field formulation was implemented to two dimensional FETD-MNRBC simulations. The method was applied to five structures with different material and the results were very good. In this chapter both

TE and TM excitations were considered and general formulations were derived. The application of the cylindrical boundary kernel was based on its generic form which increases its practicality, as discussed in Chapter 3.

The next step of this work is to extend the FETD-MNRBC to periodic structures. By incorporating the periodic boundary condition to the FEM codes, periodic structures [15] can be simulated accurately and much more time and resources efficiently. This is performed in the next chapter.

As future work one can consider the extension of the approach to three dimensional simulations and also extending the formulation for materials with more complicated behaviour such as frequency dependant ones.

## REFERENCES

- [1] I. Bardi, Z. Badics, and Z. J. Cendes, "Total and Scattered Field Formulations in the Transfinite Element Method", *IEEE Trans. on Magnetism*, vol. 44, no. 6, pp. 778-781, 2008.
- [2] A.F. Peterson and J. M. Jin, "A Two-Dimensional Time-domain Finite Element formulation for periodic structures.", *IEEE Transactions on Antennas Propag.*, vol. 53, no.4, pp. 1480-1488, 2005.
- [3] P.P. Silvester, and R.L. Ferrari, *Finite elements for electrical engineers*, 3rd ed., Cambridge University Press, Cambridge, 1996.
- [4] G. Dhatt, G. Touzot, *The Finite Element Method Displayed*, John Wiley & Sons, 1984.
- [5] C.A. Balanis, *Advanced Engineering Electromagnetics*, John Wiley & Sons, 1989.
- [6] K. Umashankar, A. Taflov, *Computational Electromagnetics*, Artech House, 1993.
- [7] A. Z. Elsherbeni and A. A. Kishk, "Modeling of cylindrical objects by circular dielectric and conducting cylinders," *IEEE Trans. Antennas Propag.*, vol. 40, pp. 96-99, Jan. 1992.
- [8] M. Lucido, G. Panariello and F. Schettino, "Scattering by Polygonal Cross-Section Dielectric Cylinders at Oblique Incidence", *IEEE Trans. Antennas Propag.*, vol. 58, no.2, Feb. 2010.
- [9] J. M. Jin, *The finite element method in electromagnetics*, Wiley-IEEE press, New York, 2002.

- [10] T. Loh, “An exact port boundary condition for the finite-element time-domain modelling of microwave devices” Ph.D. dissertation, University of Warwick, Coventry, UK, 2004.
- [11] Y. Cai, “Finite-Element Time-Domain Modelling of Periodic Structures with Floquet Modal Absorbing Boundary Condition” Ph.D. dissertation, University of Warwick, Coventry, UK, 2008.
- [12] D. M. Sullivan, *Electromagnetic Simulations Using the FDTD method*, Wiley-IEEE Press, 2000.
- [13] B. Gustavsen, and A. Semlyen, “Rational Approximation of Frequency Domain Responses by Vector Fitting”, *IEEE Trans. on Power Delivery*, vol. 14, no. 3, pp. 1052-1061, 1999.
- [14] A. Taflove, S. C. Hagness, *Computational Electrodynamics: The Finite-Difference-Time Domain Method*, 2nd ed., Boston, London, Artech House, 2000.
- [15] A. Freni, “On plane-wave scattering from an azimuthally periodic cylindrical structure”, *Microwave and Optical Technology Letters*, vol. 25, no. 4, pp. 255-257, 2000.

## CHAPTER 5

### Periodic FETD-MNRBC formulation

#### 5.1 Introduction

In this chapter the MNRBC in time domain is employed for the first time in unit-cell FETD-MNRBC formulations and applied to cylindrical structures with angular periodicity. When modelling plane wave scattering from cylindrical structures with angular periodicity one may take advantage of this periodicity to model only a single unit cell, a period of the structure, thus considerably reducing the computational resources required as shown in [1] for the finite element frequency domain method (FEFD) using the MNRBC.

The geometric discretisation of the unit-cell is performed using isoparametric surface (8-noded) and line (3-noded) elements, and both the scattered and total field formulations are derived and applied.

The approach used in this chapter has certain points that clearly differentiate it from the previous chapters. Firstly the Floquet theorem is used to express the phase difference (5.3) between the two ends of the unit cell [1, 2]. It is applied similarly to the frequency domain application of the Floquet theorem for periodic planar structures for FEFD simulations [3]. Moreover the incident field is decomposed as a summation of infinite cylindrical harmonics [1, 4] which are applied consecutively.

One advantage of time domain simulations over their frequency domain equivalents is that they allow the calculation of the response of non-linear systems [5-7.]. In this periodic time domain approach it is assumed that the problem is linear since the solution is based on the principle of superposition. The motivation for

developing this time-domain software is its originality, the innovative approach utilized and the potential of time efficiency as extrapolation is applicable to the transient response of linear problems.

This chapter begins with the frequency domain weighted residual formulation. The decomposition of the incident field and the Floquet harmonics are the first points described followed by the scattered and total field formulation for azimuthally periodic cylindrical structures. Since the scattered and total field formulations were described previously for the non-periodic case, here the emphasis is more on the concepts and issues related with the periodic implementation. After the presentation of the FEFD-MNRBC the chapter proceeds to the presentation of the FETD-MNRBC for both the scattered and total field formulations. A point of conceptual interest in the time domain implementation is the approach of the incident field components and the way they are, along with the boundary kernel, approximated with the use of Vector-Fitting. The chapter continues with the numerical results based on the derived formulations and finishes with the conclusion and possible future work.

## **5.2 Frequency domain formulation**

The concept of the approach is depicted in Fig. 5.1. If it is assumed that the cylinder has a square cross-section then it will have  $h=4$  periods and the angle of periodicity will be  $T_\phi=2\pi/h$ . Only the section of Fig. 5.1 (b) needs to be meshed and all the formulations will be applied to that.

### **5.2.1 Periodic cylindrical harmonics**

For the sake of simplicity and consistency with the previous chapters it is assumed that the incident field is moving along the  $-x$  direction. In this chapter the

incident field will be decomposed as a sum of harmonics. The incident field can be expressed as a sum of cylindrical harmonics [1, 4] as

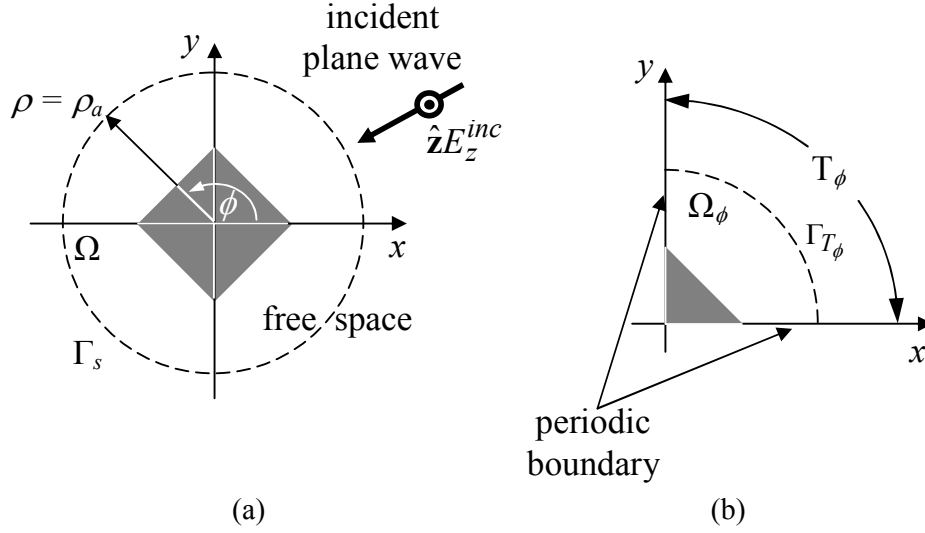


Fig. 5.1 (a) The physical geometry of the problem (b) the unit-cell

$$\tilde{\Phi}_z^{inc}(\rho, \phi) = \Phi_0^{(f)} e^{jkx} = \sum_{v_0=-\infty}^{\infty} \Phi_0^{(f)} j^{v_0} J_{v_0}(k_0 \rho) e^{jv_0 \phi} = \sum_{v_0=-\infty}^{\infty} \tilde{\Phi}_z^{inc, v_0} \quad (5.1)$$

where  $J_{v_0}$  is the Bessel function of the  $v_0$  order. Since the analysis is performed with the unit-cell, each one of the cylindrical harmonics of (5.1) is applied separately and solved as a different electromagnetic problem. The field values of the actual physical problem of Fig. 5.1 (a) will be the sum of the field values of the periodic simulation of Fig 5.1. (b) for all values of  $v_0$ . In this work it is assumed that  $-15 \leq v_0 \leq 15$  as considered in the previous chapters for the scattered field harmonics. Note that the summation of incident waves can be reduced from  $2v_0+1$  problems to  $2\pi/T_\phi$  problems as shown in [2]. The comparison for the real and the imaginary part of  $\Phi_0 e^{jkx}$  against

$\Phi_0^{(f)} \sum_{v_0=-15}^{15} j^{v_0} J_{v_0}(k_0 \rho) e^{jv_0 \phi}$  for  $\Phi_0^{(f)} = 1$  and  $\rho = 1$  is depicted in Fig. 5.2. In this figure

the error is also depicted. This is defined as  $10\log_{10}|e_{inc}|$  where  $e_{inc}$  is the difference between the two compared fields

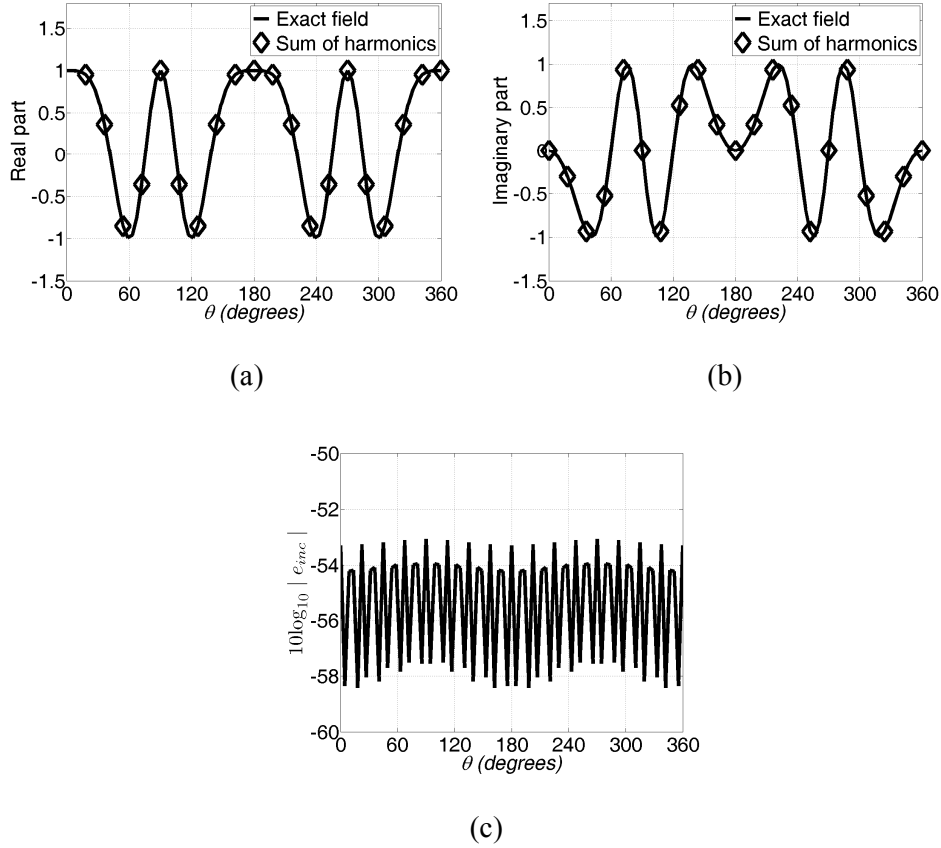


Fig. 5.2 Comparison of the exact incident field against the sum of harmonics

(a) Real part (b) Imaginary part (c) Error

Generally the scattered field from a cylinder can be expressed as [1,4]

$$\tilde{\Phi}_z^{sc}(\rho, \phi) = \sum_{v_m=-\infty}^{\infty} A_{v_m} H_{v_m}^{(2)}(k_0 \rho) e^{jv_m \phi} \quad (5.2)$$

For a given incident order  $v_0$ , the orders of the scattered field will be  $v_m$ . The field (incident, scattered and total) at the periodic boundaries satisfies the following periodic boundary condition [2]

$$\tilde{\Phi}_z^{v_0}(\rho, \phi + T_\phi) = \tilde{\Phi}_z^{v_0}(\rho, \phi) e^{jv_0 T_\phi} \quad (5.3)$$

where



$$v_m = \frac{2\pi}{T_\phi} m_0 + v_0, \quad m_0 = 0, \pm 1, \pm 2, \dots \quad (5.4)$$

Thus for the incident field component  $\tilde{\Phi}_z^{inc, v_0}$ , the corresponding scattered field

$\tilde{\Phi}_z^{sc, v_0}$  will be

$$\tilde{\Phi}_z^{sc, v_0}(\rho, \phi) = \sum_{m_0=-\infty}^{\infty} A_{v_m, v_0} H_{v_m}^{(2)}(k_0 \rho) e^{jv_m \phi} \quad (5.5)$$

As shown in Appendix E in this work the limits for  $m_0$  are

$$-\frac{15T_\phi}{\pi} \leq m_0 \leq \frac{15T_\phi}{\pi} \quad (5.6)$$

From orthogonality relations of the azimuthal exponential function it is obtained

$$A_{v_m, v_0} = \frac{1}{T_\phi} \frac{\int_0^{T_\phi} \tilde{\Phi}_z^{sc, v_0} e^{-jv_m \phi} d\phi}{H_{v_m}^{(2)}(k_0 \rho)} \quad (5.7)$$

or

$$A_{v_m, v_0} = \frac{1}{T_\phi} \frac{\int_0^{T_\phi} (\tilde{\Phi}_z^{t, v_0} - \tilde{\Phi}_z^{inc, v_0}) e^{-jv_m \phi} d\phi}{H_{v_m}^{(2)}(k_0 \rho)} \quad (5.8)$$

where  $\tilde{\Phi}_z^{t, v_0}$  denotes the total field (incident plus scattered field) when the incident

order  $v_0$  is applied.

$$\tilde{\Phi}_z^{t, v_0} = \tilde{\Phi}_z^{inc, v_0} + \tilde{\Phi}_z^{sc, v_0} \quad (5.9)$$

### 5.2.2 Scattered field formulation

The Helmholtz equation in the free space surrounding the cylinder for the scattered field will be

$$\nabla^2 \tilde{\Phi}_z^{sc, v_0} + k_0^2 \tilde{\Phi}_z^{sc, v_0} = 0 \quad (5.10)$$

where the field component  $\tilde{\Phi}_z^{sc, v_0}$  represents the total electric field component  $\tilde{E}_z^{sc, v_0}$  for TE modes and the total magnetic field component  $\tilde{H}_z^{sc, v_0}$  for TM modes.

The weak form weighted residual formulation can be written as

$$\iint_{\Omega_\phi} \left( \frac{\partial W}{\partial x} \frac{\partial \tilde{\Phi}_z^{sc, v_0}}{\partial x} + \frac{\partial W}{\partial y} \frac{\partial \tilde{\Phi}_z^{sc, v_0}}{\partial y} - k_0^2 W \tilde{\Phi}_z^{sc, v_0} \right) dx dy - \int_{\Gamma_{T_\phi}} W \frac{\partial \tilde{\Phi}_z^{sc, v_0}}{\partial \rho} d\Gamma = 0 \quad (5.11)$$

The boundary integral of (5.11) can be written by using (5.7) as

$$\int_0^{\Gamma_{T_\phi}} W \frac{\partial \tilde{\Phi}_z^{sc, v_0}}{\partial \rho} d\Gamma = \frac{2\pi}{T_\phi} \sum_{m_0=-\infty}^{\infty} G_{v_m}(\omega) \int_{\Gamma_{T_\phi}} W e^{jv_m \phi} d\Gamma \int_{\Gamma_{T_\phi}} \tilde{\Phi}_z^{sc, v_0} e^{-jv_m \phi} d\Gamma \quad (5.12)$$

Where  $G_{v_m}(\omega)$  is the same function as in (2.24). So (5.11) becomes

$$\begin{aligned} & \iint_{\Omega_\phi} \left( \frac{\partial W}{\partial x} \frac{\partial \tilde{\Phi}_z^{sc, v_0}}{\partial x} + \frac{\partial W}{\partial y} \frac{\partial \tilde{\Phi}_z^{sc, v_0}}{\partial y} - k_0^2 W \tilde{\Phi}_z^{sc, v_0} \right) dx dy \\ & - \frac{2\pi}{T_\phi} \sum_{m_0=-\infty}^{\infty} G_{v_m}(\omega) \int_{\Gamma_{T_\phi}} W e^{jv_m \phi} d\Gamma \int_{\Gamma_{T_\phi}} \tilde{\Phi}_z^{sc, v_0} e^{-jv_m \phi} d\Gamma = 0 \end{aligned} \quad (5.13)$$

Using finite element geometric discretisation the following matrix equation is obtained from (5.13)

$$[\mathbf{M}^{\Omega_\phi, \Gamma_{T_\phi}, v_0}] \{\tilde{\Phi}_z^{sc, v_0}\} = \{\mathbf{F}^{v_0}\} \quad (5.14)$$

The matrices of (5.14) are created from [8] as in the non-periodic case. The vector  $\{\mathbf{F}^{v_0}\}$  is initially zero and becomes non-zero when the incident field is applied as a Dirichlet boundary condition. Since the scattered field formulation derived is intended for PEC cylinders, the value of the scattered field at the cylinder surface will be

$$\tilde{\Phi}_z^{sc, \nu_0}(\rho, \phi) \Big|_{PEC} = -\tilde{\Phi}_z^{inc, \nu_0}(\rho, \phi) \Big|_{PEC} \quad (5.15)$$

At this stage there is a difference of the periodic formulation compared to the ones presented in the previous chapters. Equation (5.14) is modified by the application of the periodic boundary condition using an approach similar to [3]. This modification is performed in order to link the field values at the periodic boundaries with Floquet's theorem. Assuming that the weighting function  $W$  satisfies a similar periodic boundary condition as the field [9],

$$W(\rho, \phi + T_\phi) = W(\rho, \phi) e^{-j\nu_0 T_\phi} \quad (5.16)$$

and that subscripts 1 and 3 denote the two periodic boundaries and 2 the surface as depicted in Fig. 5.3, then (5.14) is modified similarly to [3] as

$$\begin{bmatrix} M_{11}^{\Omega_\phi, \Gamma_{T_\phi}, \nu_0} + M_{13}^{\Omega_\phi, \Gamma_{T_\phi}, \nu_0} \xi + M_{31}^{\Omega_\phi, \Gamma_{T_\phi}, \nu_0} \bar{\xi} + M_{33}^{\Omega_\phi, \Gamma_{T_\phi}, \nu_0} & M_{12}^{\Omega_\phi, \Gamma_{T_\phi}, \nu_0} + M_{32}^{\Omega_\phi, \Gamma_{T_\phi}, \nu_0} \bar{\xi} & 0 \\ M_{21}^{\Omega_\phi, \Gamma_{T_\phi}, \nu_0} + M_{23}^{\Omega_\phi, \Gamma_{T_\phi}, \nu_0} \xi & M_{22}^{\Omega_\phi, \Gamma_{T_\phi}, \nu_0} & 0 \\ -\xi & 0 & 1 \end{bmatrix} \begin{Bmatrix} \tilde{\Phi}_{z,1}^{sc, \nu_0} \\ \tilde{\Phi}_{z,2}^{sc, \nu_0} \\ \tilde{\Phi}_{z,3}^{sc, \nu_0} \end{Bmatrix} = \begin{Bmatrix} F_1^{\nu_0} + F_3^{\nu_0} \bar{\xi} \\ F_2^{\nu_0} \\ 0 \end{Bmatrix} \quad (5.17)$$

where

$$\xi = e^{j\nu_0 \phi} \quad \text{and} \quad \bar{\xi} = e^{-j\nu_0 \phi} \quad (5.18)$$

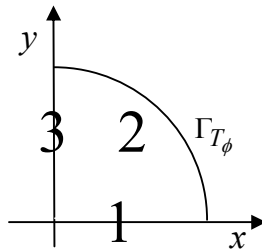


Fig. 5.3 Numbers of the geometric parts in the unit-cell

### 5.2.3 Total field formulation

The Helmholtz equation in the dielectric material and in the free space surrounding the cylinder for the total field component when the incident order  $v_0$  is applied will be

$$\nabla \cdot \frac{1}{p_r} \nabla \tilde{\Phi}_z^{t,v_0} + k_0^2 q_r \tilde{\Phi}_z^{t,v_0} = 0 \quad (5.19)$$

Where  $p_r = \mu_r$ ,  $q_r = \epsilon_r$   $\tilde{\Phi}_z^{t,v_0} = \tilde{E}_z^{t,v_0}$  for TE excitation and  $p_r = \epsilon_r$ ,  $q_r = \mu_r$ ,  $\tilde{\Phi}_z^{t,v_0} = \tilde{H}_z^{t,v_0}$  for TM excitation. Since the outer boundary is in free space the weak formulation of (5.19) is

$$\iint_{\Omega_\phi} \left( \frac{1}{p_r} \frac{\partial W}{\partial x} \frac{\partial \tilde{\Phi}_z^{t,v_0}}{\partial x} + \frac{1}{p_r} \frac{\partial W}{\partial y} \frac{\partial \tilde{\Phi}_z^{t,v_0}}{\partial y} - k_0^2 q_r W \tilde{\Phi}_z^{t,v_0} \right) dx dy - \int_{\Gamma_{T_\phi}} W \frac{\partial \tilde{\Phi}_z^{t,v_0}}{\partial \rho} d\Gamma = 0 \quad (5.20)$$

or

$$\begin{aligned} & \iint_{\Omega_\phi} \left( \frac{1}{p_r} \frac{\partial W}{\partial x} \frac{\partial \tilde{\Phi}_z^{t,v_0}}{\partial x} + \frac{1}{p_r} \frac{\partial W}{\partial y} \frac{\partial \tilde{\Phi}_z^{t,v_0}}{\partial y} - k_0^2 q_r W \tilde{\Phi}_z^{t,v_0} \right) dx dy - \\ & \int_{\Gamma_{T_\phi}} W \frac{\partial \tilde{\Phi}_z^{inc,v_0}}{\partial \rho} d\Gamma + \frac{2\pi}{T_\phi} \sum_{m_0=-\infty}^{\infty} G_{v_m}(k_0 \rho) \int_{\Gamma_{T_\phi}} W e^{jv_m \phi} d\Gamma \int_{\Gamma_{T_\phi}} \tilde{\Phi}_z^{inc,v_0} e^{-jv_m \phi} d\Gamma \\ & - \frac{2\pi}{T_\phi} \sum_{m_0=-\infty}^{\infty} G_{v_m}(k_0 \rho) \int_{\Gamma_{T_\phi}} W e^{jv_m \phi} d\Gamma \int_{\Gamma_{T_\phi}} \tilde{\Phi}_z^{t,v_0} e^{-jv_m \phi} d\Gamma = 0 \end{aligned} \quad (5.21)$$

After the total field components are separated to the LHS and the incident ones to the RHS, (5.21) becomes

$$\begin{aligned} & \iint_{\Omega_\phi} \left( \frac{1}{p_r} \frac{\partial W}{\partial x} \frac{\partial \tilde{\Phi}_z^{t,v_0}}{\partial x} + \frac{1}{p_r} \frac{\partial W}{\partial y} \frac{\partial \tilde{\Phi}_z^{t,v_0}}{\partial y} - k_0^2 q_r W \tilde{\Phi}_z^{t,v_0} \right) dx dy - \\ & \frac{2\pi}{T_\phi} \sum_{m_0=-\infty}^{\infty} G_{v_m}(k_0 \rho) \int_{\Gamma_{T_\phi}} W e^{jv_m \phi} d\Gamma \int_{\Gamma_{T_\phi}} \tilde{\Phi}_z^{t,v_0} e^{-jv_m \phi} d\Gamma \\ & = \int_{\Gamma_{T_\phi}} W \frac{\partial \tilde{\Phi}_z^{inc,v_0}}{\partial \rho} d\Gamma - \frac{2\pi}{T_\phi} \sum_{m_0=-\infty}^{\infty} G_{v_m}(k_0 \rho) \int_{\Gamma_{T_\phi}} W e^{jv_m \phi} d\Gamma \int_{\Gamma_{T_\phi}} \tilde{\Phi}_z^{inc,v_0} e^{-jv_m \phi} d\Gamma \end{aligned} \quad (5.22)$$

Equation (5.22) can be expressed in matrix form as

$$[\mathbf{M}^{\Omega_\varphi, \Gamma_{\tau_\varphi}, \mathbf{v}_0}] \{\tilde{\Phi}_z^{\text{inc}, \mathbf{v}_0}\} = [\mathbf{P}^{\Omega_\varphi, \Gamma_{\tau_\varphi}, \mathbf{v}_0}] \{\tilde{\Phi}_z^{\text{inc}, \mathbf{v}_0}\} + [\mathbf{O}^{\Omega_\varphi, \Gamma_{\tau_\varphi}, \mathbf{v}_0}] \left\{ \frac{\partial \tilde{\Phi}_z^{\text{inc}, \mathbf{v}_0}}{\partial \rho} \right\} \quad (5.23)$$

where  $[\mathbf{M}^{\Omega_\varphi, \Gamma_{\tau_\varphi}, \mathbf{v}_0}]$  is the same as in the scattered field formulation case only now is material dependent. The entries for matrices  $[\mathbf{P}^{\Omega_\varphi, \Gamma_{\tau_\varphi}, \mathbf{v}_0}]$  and  $[\mathbf{O}^{\Omega_\varphi, \Gamma_{\tau_\varphi}, \mathbf{v}_0}]$  are

$$P_{ij}^{kl,e} = - \sum_{m_0=-\infty}^{\infty} G_{\nu_m}(\omega) B_{\nu_m,i}^k C_{\nu_m,j}^l \quad (5.24)$$

$$O_{ij}^k = \int_{\Gamma^k} N_i^k(u) N_j^k(u) d\Gamma = \int_{-1}^1 N_i^k(u) N_j^k(u) J_s^k du = \int_{-1}^1 N_i^k(u) N_j^k(u) J_s^k du \quad (5.25)$$

The entries  $B_{\nu_m,i}^k$  and  $C_{\nu_m,i}^k$  can be found from (2.32) and (2.33) respectively. The vectors  $\{\tilde{\Phi}_z^{\text{inc}, \mathbf{v}_0}\}$  and  $\left\{ \frac{\partial \tilde{\Phi}_z^{\text{inc}, \mathbf{v}_0}}{\partial \rho} \right\}$  are initially zero and then the appropriate incident field values are added at the outer boundary. For the derivative of the incident field the following Bessel function identity was used [4]

$$\frac{\partial J_{\nu_0}(k_0 \rho)}{\partial \rho} = -k_0 J_{\nu_0+1}(k_0 \rho) + \frac{\nu_0}{\rho} J_{\nu_0}(k_0 \rho) \quad (5.26)$$

An alternative form for the RHS of (5.23) would be obtained if the matrices of the RHS of (5.23) were separated in terms of  $J_{\nu_0}(k_0 \rho)$  and  $J_{\nu_0+1}(k_0 \rho)$  instead of

$\tilde{\Phi}_z^{\text{inc}, \mathbf{v}_0}$  and  $\frac{\partial \tilde{\Phi}_z^{\text{inc}, \mathbf{v}_0}}{\partial \rho}$ . In this work the formulation of (5.23) was used.

At this stage the periodic boundary condition is applied by following (5.17).

### 5.3 Time domain formulation

The periodic time domain implementation of the MNRBC is not as straightforward as its non-periodic equivalents. One fundamental difficulty and also an interesting point is the application of the incident field. This is why it is presented before the finite element formulations. Another important aspect of the periodic

formulations is that the final matrix equations are complex which means that they have higher memory requirements compared to real ones. The final matrices are complex because both the incident field and the periodic boundary condition include complex terms.

### 5.3.1 Incident Field harmonics

The incident field in the FETD simulations, as described in the previous chapters, is a sine modulated by a Gaussian pulse

$$\Phi_z^{inc}(q\Delta t) = \Phi_0^{(t)} \exp\left[-\frac{(q - q_0 + \frac{x}{c\Delta t})^2}{2W^2}\right] \sin[2\pi f_c \Delta t (q - q_0 + \frac{x}{c\Delta t})] \quad (5.27)$$

where  $q$  is the timestep when (5.27) is calculated,  $q_0\Delta t$  is a deliberately introduced time delay,  $W\Delta t$  is the pulse width and  $f_c$  is a suitably chosen central frequency.

By applying the Fourier Transform on (5.27), as described in Appendix E, the frequency response is obtained which is

$$\tilde{\Phi}_z^{inc} = \Phi_0^{(t)} \frac{j}{2} \sqrt{2\pi} \cdot W\Delta t \left( e^{-(2\pi^2 (f+f_c)^2 W^2 \Delta t^2)} - e^{-(2\pi^2 (f-f_c)^2 W^2 \Delta t^2)} \right) e^{-j2\pi f q_0 \Delta t} e^{jkx} \quad (5.28)$$

At this point the  $e^{jkx}$  term is expanded as a sum of harmonics (5.1) and it is

$$\tilde{\Phi}_z^{inc} = \Phi_0^{(t)} \frac{j}{2} \sqrt{2\pi} \cdot W\Delta t \left( e^{-(2\pi^2 (f+f_c)^2 W^2 \Delta t^2)} - e^{-(2\pi^2 (f-f_c)^2 W^2 \Delta t^2)} \right) e^{-j2\pi f q_0 \Delta t} \sum_{v_0=-\infty}^{\infty} j^{v_0} J_{v_0}(k\rho) e^{jv_0\phi} \quad (5.29)$$

Thus each incident harmonic in frequency domain can be expressed as

$$\tilde{\Phi}_z^{inc, v_0} = \Phi_0^{(t)} \frac{j}{2} \sqrt{2\pi} \cdot W\Delta t \left( e^{-(2\pi^2 (f+f_c)^2 W^2 \Delta t^2)} - e^{-(2\pi^2 (f-f_c)^2 W^2 \Delta t^2)} \right) e^{-j2\pi f q_0 \Delta t} j^{v_0} J_{v_0}(k\rho) e^{jv_0\phi} \quad (5.30)$$

Or

$$\tilde{\Phi}_z^{inc, v_0} = \tilde{F}_{v_0}(f) e^{jv_0\phi} \quad (5.31)$$

where

$$\tilde{F}_{v_0}(f) = \Phi_0^{(t)} \frac{j}{2} \sqrt{2\pi} \cdot W \Delta t \left( e^{-\left(2\pi^2 (f+f_c)^2 W^2 \Delta t^2\right)} - e^{-\left(2\pi^2 (f-f_c)^2 W^2 \Delta t^2\right)} \right) e^{-j2\pi q_0 \Delta t} j^{v_0} J_{v_0}(k\rho) \quad (5.32)$$

By expanding (5.32) as a summation of partial fractions using vector fitting, one can obtain  $F(t)$ , the ILT of (5.32). The time domain form of the incident field will be

$$\Phi_z^{inc, v_0}(t) = F_{v_0}(t) e^{jv_0\phi} \quad (5.33)$$

This way the incident field components that are needed for the FETD implementation of the MNRBC are obtained. The field of (5.27) can be expressed as

$$\Phi_z^{inc}(q\Delta t) = \sum_{v_0=-\infty}^{\infty} \Phi_z^{inc, v_0} = \sum_{v_0=-\infty}^{\infty} F_{v_0}(t) e^{jv_0\phi} \quad (5.34)$$

The above procedure can be more easily understood if schematically seen in Fig. 5.4.

In this figure  $J_1, J_2 \dots J_{v_0}$  denote the incident field components which include Bessel

function. In Fig. 5.4, the relations between the depicted steps 1-6 with the above equations are 1. (5.27); 2. (5.28); 3. (5.30); 4. VF approximation of (5.30) 5. (5.33)

and 6. (5.34). At this point the accuracy of the above approximation will be shown.

The Vector-Fitting is applied to (5.32) for  $-15 \leq v_0 \leq 15$ . The VECTFIT (version 1)

input parameters for the partial fraction expansion of (5.32) are 4000 samples,

$f_{max} = 6\text{GHz}$ ,  $N = 30$  poles,  $asymflag=1$ . Moreover for the demonstrated comparison it

is  $\Phi_0^{(t)} = 1$ ,  $\phi = 0$  and  $\rho = 1$ . The pulse (5.27) characteristics and the timestep are

$W = 150$ ,  $q_0 = 700$  and  $\Delta t = 40\text{ps}$ . In Figs 5.5 and 5.6 the comparisons for

$v_0 = 0$  and  $v_0 = 15$  are shown. With regard to Fig. 5.4, the comparison between steps

3 and 4 along with error between them and the depiction of the field in step 5 can be

seen. The errors  $e_0$  and  $e_{15}$  are considered as the difference between the exact and the

approximated value and are depicted in terms of  $10\log_{10}|e_0|$  and  $10\log_{10}|e_{15}|$

respectively. In Fig. 5.7 the comparison for the whole incident field in frequency

domain can be seen. In this figure step 2 is compared with the summation of step 4 for all harmonics. In Fig. 5.8 the time domain comparison for the whole incident field is shown. The comparison is held between steps 1 and 6. In both cases the error is demonstrated next to the comparisons. It is  $e_f$  in frequency domain and  $e_t$  in time domain and depicted logarithmically as before.

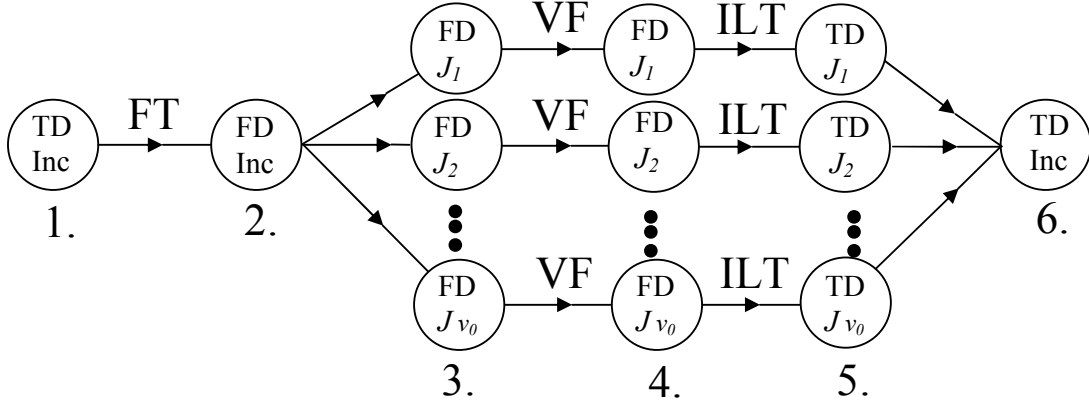


Fig. 5.4 Decomposition of the incident field harmonics

For the total field formulations the derivatives of (5.33) with respect to the radius are also needed. Each derivative of the incident harmonics in frequency domain with respect to radius can be expressed as

$$\frac{\partial \tilde{\Phi}_z^{inc, v_0}}{\partial \rho} = \Phi_0^{(t)} \frac{j}{2} \sqrt{2\pi} \cdot W \Delta t \left( e^{-\left(2\pi^2 (f+f_c)^2 W^2 \Delta t^2\right)} - e^{-\left(2\pi^2 (f-f_c)^2 W^2 \Delta t^2\right)} \right) e^{-j2\pi q_0 \Delta t} j^{v_0} \frac{\partial J_{v_0}(k\rho)}{\partial \rho} e^{jv_0 \phi} \quad (5.35)$$



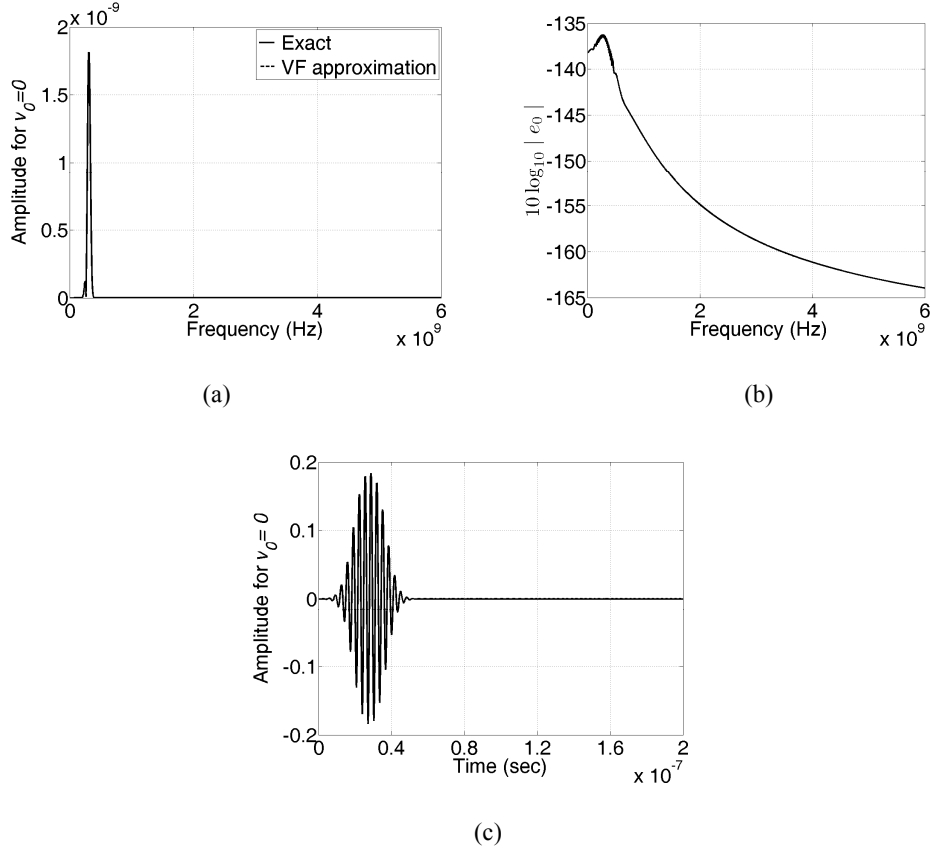


Fig. 5.5 For  $v_0 = 0$  (a) frequency domain comparison (b) absolute error (c) time domain function

Or

$$\frac{\partial \tilde{\Phi}_{z, v_0}^{inc}}{\partial \rho} = \tilde{F}'_{v_0}(f) e^{j v_0 \phi} \quad (5.36)$$

where

$$\tilde{F}'_{v_0}(f) = \Phi_0^{(t)} \frac{j}{2} \sqrt{2\pi} \cdot W \Delta t \left( e^{-\left(2\pi^2 (f+f_c)^2 W^2 \Delta t^2\right)} - e^{-\left(2\pi^2 (f-f_c)^2 W^2 \Delta t^2\right)} \right) e^{-j 2\pi q_0 \Delta t} j^{v_0} \frac{\partial J_{v_0}(k\rho)}{\partial \rho} \quad (5.37)$$

Or by using (5.26)

$$\begin{aligned} \tilde{F}'_{v_0}(f) = & \Phi_0^{(t)} \frac{j}{2} \sqrt{2\pi} \cdot W \Delta t \left( e^{-\left(2\pi^2 (f+f_c)^2 W^2 \Delta t^2\right)} - e^{-\left(2\pi^2 (f-f_c)^2 W^2 \Delta t^2\right)} \right) e^{-j 2\pi q_0 \Delta t} j^{v_0} \left( -k_0 J_{v_0+1}(k_0 \rho) + \frac{v_0}{\rho} J_{v_0}(k_0 \rho) \right) \end{aligned} \quad (5.38)$$

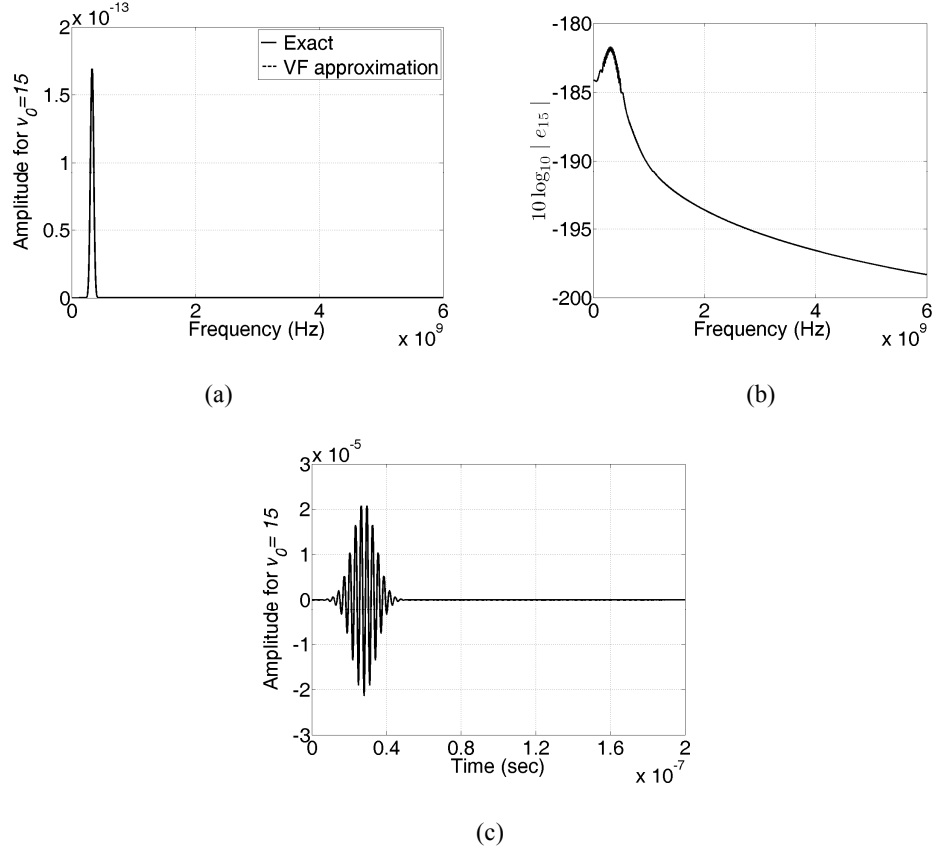


Fig. 5.6 For  $v_0 = 15$  (a) frequency domain comparison (b) absolute error (c) time domain function

Again Vector-Fitting is applied to (5.38) terms and the derivative of the incident field components can be expressed as

$$\frac{\partial \Phi_z^{inc, v_0}(t)}{\partial \rho} = F'_{v_0}(t) e^{jv_0 \phi} \quad (5.39)$$

For the VF approximation of (5.38) the same parameters are used as for (5.32). The accuracy of the approximation of (5.38) is similar to the accuracy of the approximation of (5.32) and is included in Appendix E.

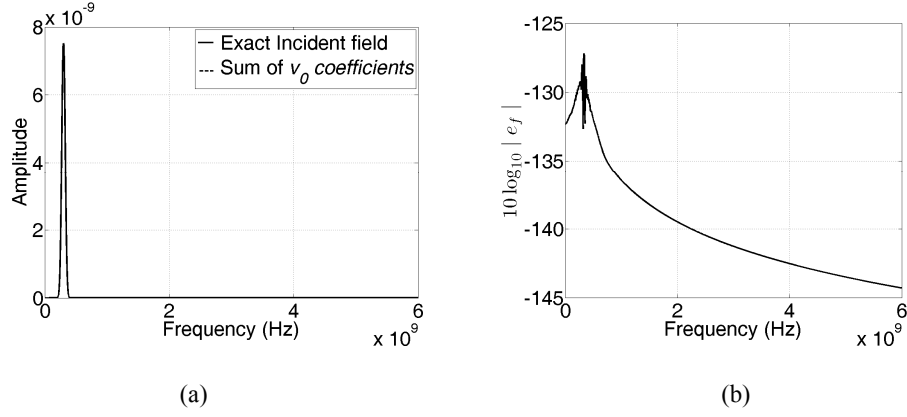


Fig. 5.7 (a) Frequency domain comparison (b) absolute error

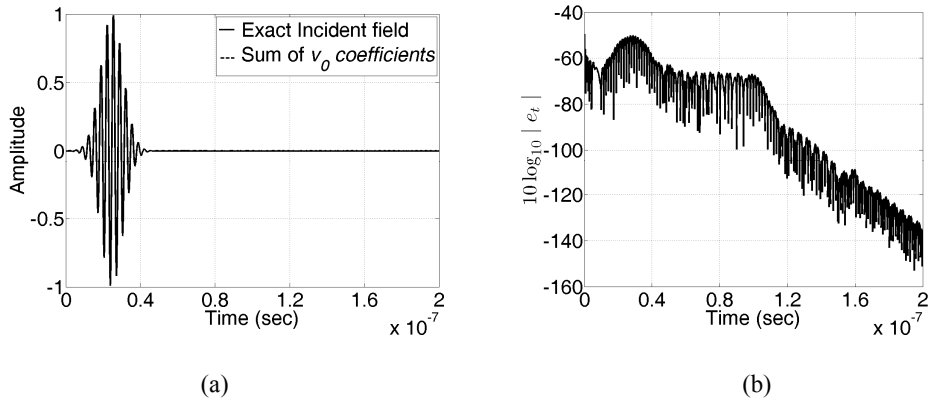


Fig. 5.8 (a) Time domain comparison (b) absolute error

Before proceeding to the scattered and total field formulation there are some things that should be pointed out. Firstly, as can be seen from (5.33), the incident field components are complex numbers. Their summation, though described by (5.27), is a real number. The other important point is that the functions of (5.32) are dependant upon the pulse characteristics, the radius and the timestep. These cannot be scaled in a way to obtain a generic form for the incident field components. This means that for each set of these parameters a different VF approximation should be found for (5.32). Lastly the effect of the delay of the pulse  $q_0\Delta t$  to the accuracy of the VF approximation is investigated in Appendix F.

### 5.3.2 Scattered field formulation

Now that the analysis of the incident field is completed, the next step is to proceed with the FETD formulations. Again, as in the non-periodic case, the scattered field formulation which is simpler will be presented firstly.

By applying ILT to (5.13) it is obtained

$$\iint_{\Omega_\phi} \left( \frac{\partial W}{\partial x} \frac{\partial \Phi_z^{sc, v_0}}{\partial x} + \frac{\partial W}{\partial y} \frac{\partial \Phi_z^{sc, v_0}}{\partial y} + \frac{1}{c^2} W \frac{\partial^2 \Phi_z^{sc, v_0}}{\partial t^2} \right) dx dy - \frac{2\pi}{T_\phi} \sum_{m_0=-\infty}^{\infty} g_{v_m}(t) * \int_{\Gamma_{T_\phi}} W e^{jv_m \phi} d\Gamma \int_{\Gamma_{T_\phi}} \Phi_z^{sc, v_0} e^{-jv_m \phi} d\Gamma = 0 \quad (5.40)$$

After geometric discretization is applied to (5.40) the global matrix equation is obtained

$$[\mathbf{S}^{\Omega_\phi}] \{\Phi_z^{sc, v_0}\} + \frac{1}{c^2} [\mathbf{T}^{\Omega_\phi}] \frac{d^2 \{\Phi_z^{sc, v_0}\}}{dt^2} + [\Psi^{\Gamma_{T_\phi}, v_0}(\mathbf{t})] * \{\Phi_z^{sc, v_0}\} = \{\mathbf{0}\} \quad (5.41)$$

The matrices  $[\mathbf{S}^{\Omega_\phi}]$ ,  $[\mathbf{T}^{\Omega_\phi}]$  are defined in (C.3), (C.4) and [8] and the elemental entries of matrix  $[\Psi^{\Gamma_{T_\phi}, v_0}(\mathbf{t})]$  are

$$\Psi_{ij}^{kl, v_0, e} = -\frac{2\pi}{T_\phi} \sum_{m_0=-\infty}^{\infty} g_{v_m}(t) B_{v_m, i}^k C_{v_m, j}^l \quad (5.42)$$

where  $B_{v_m, i}^k$  and  $C_{v_m, j}^l$  are given in (2.32) and (2.33). Here, the elemental entries

$\Psi_{ij}^{kl, e}$  differ from those in the non periodic case by a factor  $2\pi/T_\phi$ . The time function  $g_{v_m}(t)$ , the ILT of  $G_{v_m}(\omega)$ , is obtained in the same way as in Chapter 2 using the publicly available Vector Fitting [10] software VECTFIT. This means that the unit-cell FETD-MNRBC formulation is similar to the one for the FETD non-periodic case although now the summation is performed for  $m_0$  which is linked to  $v_m$  and the matrices/vectors assembled from boundary elemental contributions are

multiplied by the factor  $2\pi/T_\phi$ . Following time discretisation, as in the non-periodic case, the following matrix equation is obtained

$$[\mathbf{K}^{\Omega_\phi, \Gamma_{T_\phi}, \nu_0}] \{\Phi_z^{\text{sc}, \nu_0}\}^{q+1} = \{\mathbf{b}^{\nu_0}\} \quad (5.43)$$

where  $q$  is the current time step ( $t = q\Delta t$ ). The matrix  $[\mathbf{K}^{\Omega_\phi, \Gamma_{T_\phi}, \nu_0}]$  and vector  $\{\mathbf{b}^{\nu_0}\}$  are defined in equations (2.59) and (2.58) of Chapter 2 respectively. The superscript  $\nu_0$  in all the above matrices and vectors indicates that they are different for each incident field component of order  $\nu_0$ . The Dirichlet boundary condition is applied to (5.43) and hence the vector  $\{\mathbf{b}^{\nu_0}\}$  is updated with entries equal to “minus the incident field” at time step number  $q+1$ . For each order  $\nu_0$  the incident field component will be given by (5.33). As in (5.17), the matrix equation is modified by the application of the periodic boundary condition as follows

$$\begin{aligned} & \begin{bmatrix} K_{11}^{\Omega_\phi, \Gamma_{T_\phi}, \nu_0} + K_{13}^{\Omega_\phi, \Gamma_{T_\phi}, \nu_0} \xi + K_{31}^{\Omega_\phi, \Gamma_{T_\phi}, \nu_0} \bar{\xi} + K_{33}^{\Omega_\phi, \Gamma_{T_\phi}, \nu_0} & K_{12}^{\Omega_\phi, \Gamma_{T_\phi}, \nu_0} + K_{32}^{\Omega_\phi, \Gamma_{T_\phi}, \nu_0} \bar{\xi} & 0 \\ & K_{21}^{\Omega_\phi, \Gamma_{T_\phi}, \nu_0} + K_{23}^{\Omega_\phi, \Gamma_{T_\phi}, \nu_0} \xi & K_{22}^{\Omega_\phi, \Gamma_{T_\phi}, \nu_0} \\ & -\xi & 0 \end{bmatrix} \begin{Bmatrix} \Phi_{z,1}^{\text{sc}, \nu_0} \\ \Phi_{z,2}^{\text{sc}, \nu_0} \\ \Phi_{z,3}^{\text{sc}, \nu_0} \end{Bmatrix} \\ & = \begin{Bmatrix} b_1^{\nu_0} + b_3^{\nu_0} \bar{\xi} \\ b_2^{\nu_0} \\ 0 \end{Bmatrix} \end{aligned} \quad (5.44)$$

Note that with this formulation the final matrix equation to be solved is complex.

### 5.3.3 Total field formulation

The application of the total field formulation is straightforward. The ILT of (5.22) is

$$\begin{aligned}
& \iint_{\Omega_\phi} \left( \frac{1}{p_r} \frac{\partial W}{\partial x} \frac{\partial \tilde{\Phi}_z^{t,v_0}}{\partial x} + \frac{1}{p_r} \frac{\partial W}{\partial y} \frac{\partial \tilde{\Phi}_z^{t,v_0}}{\partial y} - k_0^2 q_r W \tilde{\Phi}_z^{t,v_0} \right) dx dy - \\
& \frac{2\pi}{T_\phi} \sum_{m_0=-\infty}^{\infty} G_{v_m}(k_0 \rho) \int_{\Gamma_{T_\phi}} W e^{jv_m \phi} d\Gamma \int_{\Gamma_{T_\phi}} \tilde{\Phi}_z^{t,v_0} e^{-jv_m \phi} d\Gamma \\
& = \int_{\Gamma_{T_\phi}} W \frac{\partial \tilde{\Phi}_z^{inc,v_0}}{\partial \rho} d\Gamma - \frac{2\pi}{T_\phi} \sum_{m_0=-\infty}^{\infty} G_{v_m}(k_0 \rho) \int_{\Gamma_{T_\phi}} W e^{jv_m \phi} d\Gamma \int_{\Gamma_{T_\phi}} \tilde{\Phi}_z^{inc,v_0} e^{-jv_m \phi} d\Gamma
\end{aligned} \tag{5.45}$$

Or it matrix form

$$[\mathbf{S}_{p_r}^{\Omega_\phi}] \{\Phi_z^{t,v_0}\} + \frac{1}{c^2} [\mathbf{T}_{q_r}^{\Omega_\phi}] \frac{d\{\Phi_z^{t,v_0}\}}{dt^2} + [\Psi^{\Gamma_{T_\phi}}(\mathbf{t})] * \{\Phi_z^{t,v_0}\} = [\Psi^{\Gamma_{T_\phi}}(\mathbf{t})] * \{\Phi_z^{inc,v_0}\} + [\mathbf{O}^{\Omega_\phi, \Gamma_{T_\phi}, v_0}] \left[ \frac{\partial \{\Phi_z^{t,v_0}\}}{\partial \rho} \right] \tag{5.46}$$

And finally

$$[\mathbf{K}^{\Omega_\phi, \Gamma_{T_\phi}}] \{\Phi_z^{t,v_0}\}^{q+1} = \{\mathbf{d}^{v_0}\} \tag{5.47}$$

Where following the Newmark-beta discretisation scheme for  $\beta=0.25$ , it is

$$\begin{aligned}
\{\mathbf{d}^{v_0}\} &= [\mathbf{L}_1^{\Omega_\phi, \Gamma_{T_\phi}}] \{\Phi_z^{t,v_0}\}^q - [\mathbf{L}_2^{\Omega_\phi, \Gamma_{T_\phi}}] \{\Phi_z^{t,v_0}\}^{q-1} - \{\mathbf{D}^{\Gamma_{T_\phi}, t}\}^q \\
&+ [\mathbf{N}_1^{\Gamma_{T_\phi}}] \{\Phi_z^{inc,v_0}\}^{q+1} + [\mathbf{N}_2^{\Gamma_{T_\phi}}] \{\Phi_z^{inc,v_0}\}^{q+1} + [\mathbf{N}_3^{\Gamma_{T_\phi}}] \{\Phi_z^{inc,v_0}\}^{q+1} + \{\mathbf{D}^{\Gamma_{T_\phi}, inc}\}^q \\
&+ [\mathbf{O}^{\Omega_\phi, \Gamma_{T_\phi}, v_0}] \cdot \left\{ \frac{1}{4} \left\{ \frac{\partial \Phi_z^{inc,v_0}}{\partial \rho} \right\}^{q+1} + \frac{1}{2} \left\{ \frac{\partial \Phi_z^{inc,v_0}}{\partial \rho} \right\}^q + \frac{1}{4} \left\{ \frac{\partial \Phi_z^{inc,v_0}}{\partial \rho} \right\}^{q-1} \right\}
\end{aligned} \tag{5.48}$$

and

$$[\mathbf{N}_1^{\Gamma_{T_\phi}}] = \frac{1}{2\Delta t} [\mathbf{V}^{\Gamma_{T_\phi}}] + \frac{1}{4} [\mathbf{Q}^{\Gamma_{T_\phi}}] \tag{5.49}$$

$$[\mathbf{N}_2^{\Gamma_{T_\phi}}] = \frac{1}{2} [\mathbf{Q}^{\Gamma_{T_\phi}}] \tag{5.50}$$

$$[\mathbf{N}_3^{\Gamma_{T_\phi}}] = -\frac{1}{2\Delta t} [\mathbf{V}^{\Gamma_{T_\phi}}] + \frac{1}{4} [\mathbf{Q}^{\Gamma_{T_\phi}}] \tag{5.51}$$

The entries for  $[\mathbf{O}^{\Omega_\phi, \Gamma_{T_\phi}, v_0}]$  are given in (5.25). The entries for  $\{\tilde{\Phi}_z^{inc,v_0}\}$  and

$\left\{ \frac{\partial \tilde{\Phi}_z^{inc,v_0}}{\partial \rho} \right\}$  matrices for timesteps  $q-1$ ,  $q$ ,  $q+1$  are calculated at the appropriate

timestep using the VF approximations of (5.33) and (5.36). The matrix  $[\mathbf{K}^{\Omega_\phi, \Gamma_{T_\phi}, v_0}]$  is

created as in the scattered field formulation. The difference is that now it is material dependent. The rest of the matrices were defined in Chapter 4. The last step is the application of the periodic boundary condition following (5.44).

## 5.4 Numerical Results

The accuracy of the formulations described in this chapter is validated through comparison for the BSW of cylindrical periodic structures. For the calculation of the BSW there are two differences with the procedure used so far.

The first difference has to do with the way the time domain results of the FETD-MNRBC are transformed to frequency domain. Again the approach is based on [11]. This time it has the form of (2.66) so it will be

$$\tilde{E}_z^{sc}(\rho_a, \theta, f_c) = \sum_{q=0}^{q_{\max}} E_z^{sc}(\rho_a, \theta, q\Delta t) \exp(-j2\pi f_c q\Delta t) \quad (5.52)$$

Or in computer code similarly to [11] and (2.69)-(2.70) it can be expressed as

$$\tilde{E}_z^{sc}(\rho_a, \theta, f_c) = \tilde{E}_z^{sc}(\rho_a, \theta, f_c) + E_z^{sc}(\rho_a, \theta, (q+1)\Delta t) \exp[-j2\pi f_c (q+1)\Delta t] \quad (5.53)$$

where  $\tilde{E}_z^{sc}(\rho_a, \theta, f_c)$  and  $E_z^{sc}(\rho_a, \theta, q\Delta t)$  represent the frequency and time domain versions of the scattered field. The variable  $f_c$  represents the frequency at which the BSW is calculated, here chosen to be the carrier frequency. The values of the field are subsequently normalized with the frequency domain amplitude of the incident field. The latter is found by applying (5.52) to (5.27) for  $x=0$ .

The second difference has to do with the way to go from the  $A_{v_m, v_0}$  coefficients of (5.7) to the  $A_{v_m}$  coefficients needed for the calculation of BSW (2.63). The relation is

$$A_{v_m} = \sum_{v_0=-\infty}^{\infty} A_{v_m, v_0} \quad (5.54)$$

The physical meaning of (5.54) is that all the contributions of all incident orders  $v_0$  are added in order to find the whole scattered field components  $v_m$ .

The next step is to proceed to the presentation of the three simulated structures. These are structures that were also simulated in the previous chapters but now only one unit-cell of them is used as grid.

The first structure is the PEC circular cylinder depicted in Fig. 3.3. Since this structure is circular a value for period can be chosen arbitrarily. It was chosen  $T_\phi = \pi/2$ . In Fig. 5.9 (a) there is the mesh for the whole structure that was used previously and in Fig. (5.9) (b) the mesh used here. This structure is approached with both scattered and total field formulations.

The second structure is the PEC square scatterer of Fig. 3.6. This structure has a natural periodicity of  $T_\phi = \pi/2$  or 4 periods. In Fig. 5.10 (a) there is the mesh for the whole structure that was used previously and in Fig. 5.10 (b) the mesh used here. This structure simulated using total field formulation.

Lastly the circular PEC cylinder surrounded with dielectric from Fig. 4.1 was simulated. Since this is a circular cylinder it was chosen  $T_\phi = \pi/4$ . Fig. 5.11 displays the meshes. This structure simulated using total field formulation. Table 5.1 presents the details for the parameters for each structure. In all cases the periodic meshes are a fraction of their non-periodic equivalents.



**Table 5.1**

Simulation parameters

Parameters	Geometry (cross-section)		
	Circular	Square	Circular
Material	PEC	PEC	PEC and dielectric
Relative permittivity $\epsilon_r$	-	-	2
Relative permeability $\mu_r$	-	-	2
Elements (nodes)	90 (309)	90 (309)	35 (130)
$\Delta s$ min. $^{*\dagger}$ (mm) Free space	27.778	15.910	39.26
$\Delta s$ min. $^{*\dagger}$ (mm) dielectric	-	-	25
$\Delta s$ max. $^{*\dagger}$ (mm) Free space	78.520	78.520	78.520
$\Delta s$ max. $^{*\dagger}$ (mm) dielectric	-	-	39.26
Courant limit $^{\dagger}$ (ps) free space	65.473	37.5	92.536
Courant limit $^{\dagger}$ (ps) dielectric	-	-	29.463

$f_{max}^+$ (GHz)	0.451	0.451	0.451
Nyquist criterion (ps) <sup>§</sup>	1109.6	1109.6	1109.6
$\Delta t$ (ps)	40	25	20
$\Phi_0$ (V/m)	1.0	1.0	1.0
$q_0$ ( $\Delta t$ )	700	1200	1500
$W$ ( $\Delta t$ )	150	240	300
$\rho_\alpha(\lambda)^*$	1.0	1.0	1.0
$f_c$ (GHz)	0.3	0.3	0.3
Number of time steps	3000	5000	6000
Scattered field Computing Time (s)**	722.250	-	-
Total field Computing Time (s)**	1486.531	2474.671	470.187
<sup>+</sup> frequency ( $>f_c$ ) at which the incident field spectral amplitude is $10^{-7} \times$ (spectral amplitude at $f_c$ ); <sup>*</sup> at $\lambda = 1$ m; <sup>**</sup> for the FETD-MNRBC method; <sup>§</sup> $\Delta t \leq 0.5/f_{max}$ ; <sup>†</sup> $\Delta s$ = distance between consecutive nodes in a finite element, $\Delta s \leq 0.125c/f_{max} = 83.2\text{mm}$ ; <sup>‡</sup> $\Delta t \leq \Delta s/(c\sqrt{2})$ adapted from [12].			

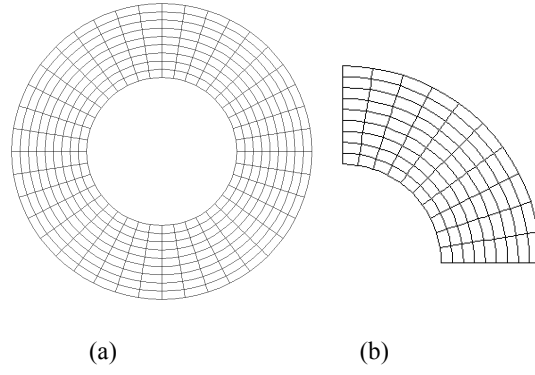


Fig. 5.9. Circular PEC cylinder (a) Full mesh (b) Unit-cell

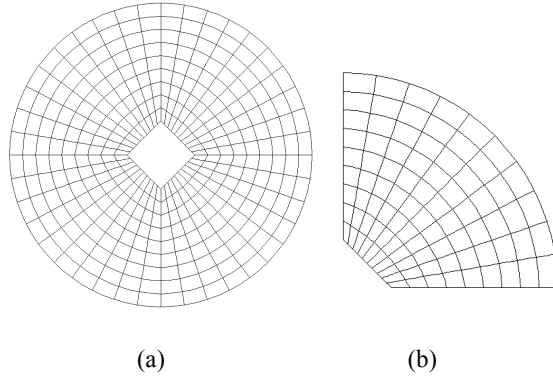


Fig. 5.10. Square PEC cylinder (a) Full mesh (b) Unit-cell

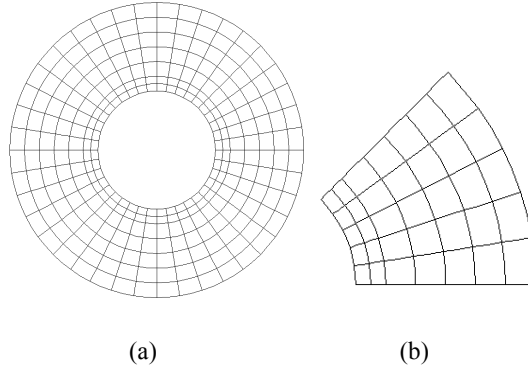


Fig. 5.11. Circular PEC cylinder surrounded by dielectric (a) Full mesh (b) Unit-cell

For the VF approximation of the boundary kernel the parameters derived for Chapter 2 were used (VFG). For the VF approximation of the incident components the VF parameters were 4000 samples,  $f_{max} = 6\text{GHz}$ ,  $N = 30$  poles and  $asymflag=1$ .

Before proceeding with the results there is an important aspect that should be pointed out. For the total field formulation the entries for the incident column vectors

$\{\tilde{\Phi}_z^{\text{inc},v_0}\}$  and  $\{\frac{\partial \tilde{\Phi}_z^{\text{inc},v_0}}{\partial \rho}\}$  calculated at the outer boundary are needed. This boundary

has the same radius in all points as depicted in Fig. 5.1 (b). This means that VF must be applied once for each order of functions (5.32) and (5.37). In the scattered field formulation only (5.32) is needed but the incident field is applied on the PEC boundary. This means that for each point on the PEC boundary that has different radial distance for the centre of the cylinder a different set of VF coefficients is needed. In other words for each point with different radial distance, a different VF approximation of (5.32) must be calculated and saved which makes the formulation impractical for PEC cylinders of non circular cross-section. This is why the scattered field formulation is applied only to the circular PEC cylinder and the total to all structures.

The numerical results for the circular PEC cylinder using scattered and total field formulation are Figs. 5.12 and 5.13 respectively. The simulation results are compared with the analytical [4]. Fig. 5.14 shows the square cylinder's BSW comparison. The reference solution results were obtained from [13]. In Fig 5.15 there is the BSW comparison for the PEC circular cylinder surrounded with dielectric against the analytical solution [13]. In all cases TE polarization was considered and the FEFD-MNRBC and FETD-MNRBC are indistinguishable.

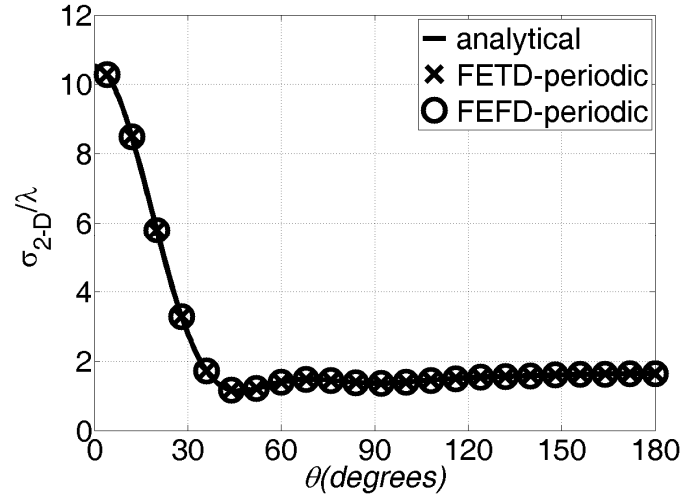


Fig. 5.12. BSW normalized with  $\lambda$  of the circular PEC scatterer for scattered field formulation

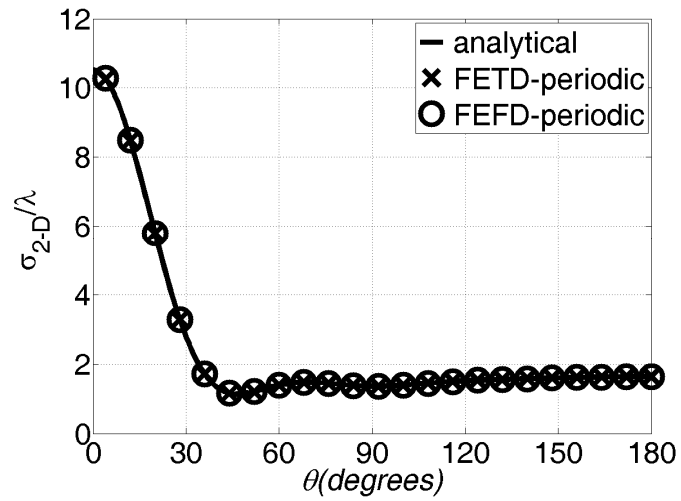


Fig. 5.13. BSW normalized with  $\lambda$  of the circular PEC scatterer for total field formulation

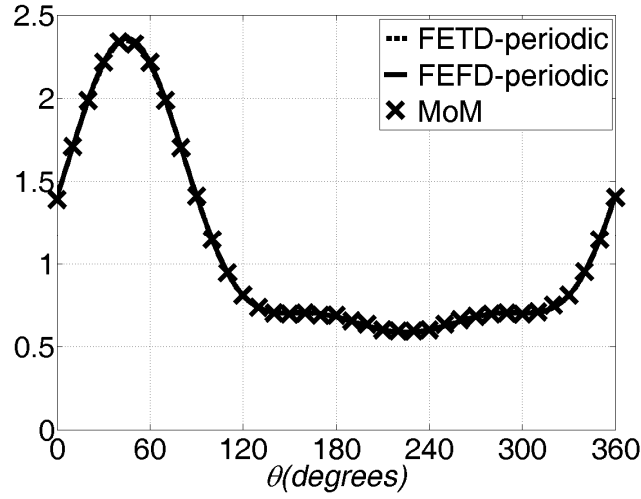


Fig. 5.14. BSW normalized with  $\lambda$  of the square PEC scatterer for total field formulation

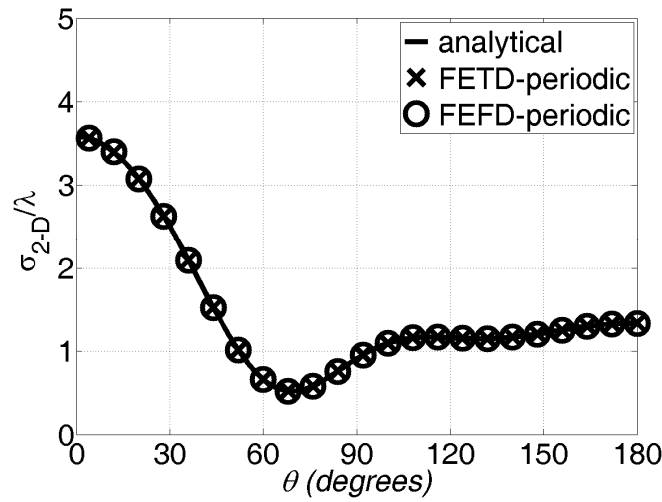


Fig. 5.15. BSW normalized with  $\lambda$  of the PEC circular scatterer with dielectric for total field formulation

## 5.5 Scientific contribution and future work

In this Chapter, for the first time, unit-cell FETD-MNRBC formulations were derived and applied to azimuthally periodic cylindrical structures. A very important part of this formulation is the application of the incident field, which was applied as a

sum of incident components with the use of the Vector Fitting approximation. The method was validated with accurate numerical results.

The derivation of unit-cell FETD-MNRBC formulations is important since it adds to the completeness of the study of cylindrical structures. Furthermore as it was shown throughout this chapter, vital concepts of cylinder were extensively used and thus it strongly supports the comprehension of plane wave scattering from cylinders. One another point is that the mathematical elegance of the approach could be found interesting and useful also for people working in other areas of research and who use mathematically similar models.

The approach is based on the decomposition of the incident field in harmonics which are then approximated with VF. Use of the Floquet theorem allows the modelling of only one period of the structures which is more memory efficient. The disadvantages of the method are that a complex matrix system is solved in time domain and that the problem must be linear, since superposition is used for the decomposition of the incident harmonics since each incident harmonic is applied separately and the resulting scattered field is summed in order to find the BSW.

The method has the potential of better time efficiency by using the approach of [1] which results to solving a number of electromagnetic problems equal to the number of periods of the structures and not equal to the number of the harmonics used as here. Moreover extrapolation [14] is applicable to the time domain transient response which can further optimize the method.

The method could also be extended and applied to 3D structures where memory and time constraints are more important. Another interesting extension that could be investigated is the application of other types of incident excitations using cylindrical function expansions.

## REFERENCES

- [1] A. Freni, "On plane-wave scattering from an azimuthally periodic cylindrical structure", *Microwave and Optical Technology Letters*, vol. 25, no. 4, pp. 255-257, 2000.
- [2] T. Cwik, "Coupling into and Scattering from Cylindrical Structures Covered Periodically with Metallic Patches", *IEEE Trans. Antennas Propag.* vol. 38, no. 2, pp.220-226, Feb. 1990.
- [3] C. Mias, "Finite Element Modelling of the electromagnetic behaviour of spatially periodic structures", PhD dissertation, Cambridge University, Cambridge, UK, 1995.
- [4] C.A. Balanis, *Advanced Engineering Electromagnetics*, John Wiley & Sons, 1989.
- [5] E.K. Miller, "Time-domain modeling in electromagnetics", *Journal of electromagnetic Waves and Applications*, vol.8, no. 9/10, pp.1125-1172,1994.
- [6] F.L. Teixeira, "Time-Domain Finite-Difference and Finite-Element Methods for Maxwell Equations in Complex Media", *IEEE Trans. Antennas Propag.* vol. 56, no8, pp.2150-2166, Aug. 2008.
- [7] A. Taflove, S. C. Hagness, *Computational Electrodynamics: The Finite-Difference-Time Domain Method*, 2nd ed., Boston, London, Artech House, 2000.
- [8] P.P. Silvester, and R.L. Ferrari, *Finite elements for electrical engineers*, 3rd ed., Cambridge University Press, Cambridge, 1996.
- [9] Ferrari, R.L.: 'Finite element solution of time-harmonic modal fields in periodic structures', *Electronics Letters*, 1991, vol. 27, no. 1, pp. 33-34



- [10] B. Gustavsen, and A. Semlyen, "Rational Approximation of Frequency Domain Responses by Vector Fitting", *IEEE Trans. on Power Delivery*, vol. 14, no. 3, pp. 1052-1061, 1999.
- [11] D. M. Sullivan, *Electromagnetic Simulations Using the FDTD method*, Wiley-IEEE Press, 2000.
- [12] A. Taflove, S. C. Hagness, *Computational Electrodynamics: The Finite-Difference-Time Domain Method*, 2nd ed., Boston, London, Artech House, 2000.
- [13] K. Umashankar, A. Taflove, *Computational Electromagnetics*, Artech House, 1993.
- [14] Y. Cai, "Finite-Element Time-Domain Modelling of Periodic Structures with Floquet Modal Absorbing Boundary Condition" Ph.D. dissertation, University of Warwick, Coventry, UK, 2008.

## CHAPTER 6

### Sparse-FETD-MNRBC formulation

#### 6.1 Introduction

The focus of this chapter is on a novel sparse matrix FETD-MNRBC scattered field formulation. This improves the efficiency of the MNRBC by avoiding the presence of the double integral in the boundary. The cost on the accuracy of the BSW calculations is investigated.

The FETD-MNRBC that was presented in the previous chapters has the disadvantage that the modal non-reflecting boundary condition is a non-local boundary condition as can be seen in equation (2.41). Unlike local boundary conditions and other finite element region truncation methodologies such as the perfectly matched layer, this non-local boundary condition, due to the presence of a time consuming double boundary integral, does not lead to a fully sparse finite element matrix but a partially sparse/partially fully dense matrix that increases the computation time and memory resources required during simulation. The proposed sparse-FETD-MNRBC method alleviates this problem.

The sparse-FETD-MNRBC is derived for scattered field formulation and for reasons of uniformity with the standard-FETD-MNRBC scattered field formulation presented in Chapter 2 it will be derived for TE polarization. The same PEC structures of Chapter 2 are simulated with the new formulation, which allows direct accuracy comparisons.

Another secondary extension to the scattered field formulation which is considered in the first part of this chapter has to do with the use of the scattered field

formulation for the simulation of scattering from dielectric cylinders. The formulations derived previously for total field FETD-MNRBC can be applied to both dielectric and PEC cylinders of arbitrary cross-section while the formulations derived for scattered field FETD-MNRBC were designed for PEC cylinders of arbitrary cross-section. Nevertheless in the literature it is shown that scattered field formulation can be appropriately extended and applied to dielectrics [1,2]. Therefore it is important to check this possibility as well.

The scattered field FETD-MNRBC is extended for TE problems with varying relative permittivity but relative permeability equal to unity in all cases. This is done because the objective of this presentation is to show the potential of the scattered field formulation rather than to show all possible formulations.

A total-scattered field decomposition is a scheme widely used in FDTD [3, 4] and introduced in FETD methods as well [5]. This is unnecessary to be considered in this work since the boundary condition used here can be put close to the scatterer and thus there is no need for more distance for the scattered field as with analytical boundary conditions [6,7].

This chapter begins by presenting the formulations for the scattered field formulation for dielectrics. Then the numerical results for this formulation are shown. The next big step is the presentation of the sparse-FETD-MNRBC formulation. After that the numerical results for the BSW of the PEC cylinders of Chapter 2 are considered. Along these there is also an error and efficiency investigation for this formulation, which concludes the results of this thesis.

## 6.2 Scattered field FETD-MNRBC for dielectrics

The formulation presented is based on [1] but now for simplicity only the relative permittivity changes with position in the mesh.

### 6.2.1 Formulation

Assuming that the relative permeability is equal to unity everywhere, the Helmholtz equation in terms of the total field for TE polarization can be written as

$$\nabla^2 \tilde{E}_z^t + k_0^2 \varepsilon_r \tilde{E}_z^t = 0 \quad (6.1)$$

The total field can be written as a summation of the scattered plus the incident

$$\tilde{E}_z^t = \tilde{E}_z^{sc} + \tilde{E}_z^{inc} \quad (6.2)$$

By inserting (6.2) in (6.1) it becomes

$$\nabla^2 (\tilde{E}_z^{sc} + \tilde{E}_z^{inc}) + k_0^2 \varepsilon_r (\tilde{E}_z^{sc} + \tilde{E}_z^{inc}) = 0 \quad (6.3)$$

$$\nabla^2 \tilde{E}_z^{sc} + k_0^2 \varepsilon_r \tilde{E}_z^{sc} = -\nabla^2 \tilde{E}_z^{inc} - k_0^2 \varepsilon_r \tilde{E}_z^{inc} \quad (6.4)$$

The incident field satisfies the Helmholtz equation in free space

$$\nabla^2 \tilde{E}_z^{inc} + k_0^2 \tilde{E}_z^{inc} = 0 \quad (6.5)$$

And by substituting (6.5) in (6.4) it is

$$\nabla^2 \tilde{E}_z^{sc} + k_0^2 \varepsilon_r \tilde{E}_z^{sc} = k_0^2 \tilde{E}_z^{inc} - k_0^2 \varepsilon_r \tilde{E}_z^{inc} \quad (6.6)$$

$$\nabla^2 \tilde{E}_z^{sc} + k_0^2 \varepsilon_r \tilde{E}_z^{sc} + k_0^2 (\varepsilon_r - 1) \tilde{E}_z^{inc} = 0 \quad (6.7)$$

The weak formulation of (6.7) is

$$\begin{aligned} R = & \iint_{\Omega} (\nabla W \bullet \nabla \tilde{E}_z^{sc} - k_0^2 \varepsilon_r W \tilde{E}_z^{sc}) d\Omega - \oint_{\Gamma_s} W \frac{\partial \tilde{E}_z^{sc}}{\partial \rho} d\Gamma \\ & - \iint_{\Omega} k_0^2 (\varepsilon_r - 1) W \tilde{E}_z^{inc} d\Omega = 0 \end{aligned} \quad (6.8)$$

The global matrix formulation of (6.8) is

$$\underbrace{[\mathbf{S}^\Omega] - k_0^2[\mathbf{T}_{\varepsilon_r}^\Omega] + [\mathbf{P}^\Gamma]}_{[\mathbf{M}^{\Omega,\Gamma}]} \{\tilde{\mathbf{E}}_z^{sc}\} = [k_0^2[\mathbf{T}_{\varepsilon_r-1}^\Omega]]\{\tilde{\mathbf{E}}_z^{inc}\} \quad (6.9)$$

The matrices  $[\mathbf{S}^\Omega]$  and  $[\mathbf{T}^\Omega]$  can be found in [8]. Matrices  $[\mathbf{T}_{\varepsilon_r}^\Omega]$  and  $[\mathbf{T}_{\varepsilon_r-1}^\Omega]$  are calculated as  $[\mathbf{T}^\Omega]$  only the elemental entries are scaled by  $\varepsilon_r$  and  $\varepsilon_r-1$  respectively before they are added to the global ones. This is the same that was applied in chapter 4 for the total field formulation.

The ILT of (6.8) is

$$\begin{aligned} R = & \iint_{\Omega} \left( \nabla W \bullet \nabla E_z^{sc} + \frac{\varepsilon_r}{c^2} W \frac{d^2 E_z^{sc}}{dt^2} \right) d\Omega - \oint_{\Gamma_s} W \frac{\partial E_z^{sc}}{\partial \rho} d\Gamma \\ & + \iint_{\Omega} \left( \frac{\varepsilon_r - 1}{c^2} W \frac{d^2 E_z^{inc}}{dt^2} \right) d\Omega = 0 \end{aligned} \quad (6.10)$$

Using the Newmark-beta discretisation scheme for  $\beta=0.25$  the time derivative of the incident field is

$$\frac{d^2 \{E_z^{inc}(t)\}}{dt^2} = \frac{1}{\Delta t^2} (\{E_z^{inc}\}^{q+1} - 2\{E_z^{inc}\}^q + \{E_z^{inc}\}^{q-1}) \quad (6.11)$$

In matrix form (6.10) becomes

$$\begin{aligned} & [\mathbf{S}^\Omega + \mathbf{Q}^\Gamma] \{\mathbf{E}_z^{sc}\} + [\mathbf{V}^\Gamma] \frac{d\{\mathbf{E}_z^{sc}\}}{dt} + \frac{1}{c^2} [\mathbf{T}_{\varepsilon_r}^\Omega] \frac{d^2 \{\mathbf{E}_z^{sc}\}}{dt^2} + \{\mathbf{D}^\Gamma(t)\} \\ & + \frac{1}{c^2} [\mathbf{T}_{\varepsilon_r-1}^\Omega] \frac{d^2 \{\mathbf{E}_z^{inc}\}}{dt^2} = \{\mathbf{0}\} \end{aligned} \quad (6.12)$$

And finally

$$[\mathbf{K}^{\Omega,\Gamma}] \{\mathbf{E}_z^{sc}\}^{q+1} = \underbrace{[\mathbf{L}_1^{\Omega,\Gamma}] \{\mathbf{E}_z^{sc}\}^q - [\mathbf{L}_2^{\Omega,\Gamma}] \{\mathbf{E}_z^{sc}\}^{q-1} - \{\mathbf{D}^\Gamma\}^q + [\mathbf{L}_3^\Omega] \{\mathbf{E}_z^{inc}\}^q}_{\{\mathbf{b}\}} \quad (6.13)$$

where

$$[\mathbf{K}^{\Omega,\Gamma}] = \frac{1}{c^2 \Delta t^2} [\mathbf{T}_{\varepsilon_r}^\Omega] + \frac{1}{4} [\mathbf{S}^\Omega] + \frac{1}{2\Delta t} [\mathbf{V}^\Gamma] + \frac{1}{4} [\mathbf{Q}^\Gamma] \quad (6.14)$$

$$[\mathbf{L}_1^{\Omega,\Gamma}] = \frac{2}{c^2 \Delta t^2} [\mathbf{T}_{\varepsilon_r}^\Omega] - \frac{1}{2} [\mathbf{S}^\Omega] - \frac{1}{2} [\mathbf{Q}^\Gamma] \quad (6.15)$$

$$[\mathbf{L}_2^{\Omega, \Gamma}] = \frac{1}{c^2 \Delta t^2} [\mathbf{T}_{\varepsilon_r}^{\Omega}] + \frac{1}{4} [\mathbf{S}^{\Omega}] - \frac{1}{2 \Delta t} [\mathbf{V}^{\Gamma}] + \frac{1}{4} [\mathbf{Q}^{\Gamma}] \quad (6.16)$$

$$[\mathbf{L}_3^{\Omega}] = -\frac{1}{c^2 \Delta t^2} [\mathbf{T}_{\varepsilon_r-1}^{\Omega}] \quad (6.17)$$

$$\{\mathbf{E}_z^{inc}\}^{\bar{q}} = \{\mathbf{E}_z^{inc}\}^{q+1} - 2\{\mathbf{E}_z^{inc}\}^q + \{\mathbf{E}_z^{inc}\}^{q-1} \quad (6.18)$$

It is clear when (6.13)-(6.18) is compared with the respective relations of scattered (2.57)-(2.61) and total field (4.36)-(4.40) formulation that this formulation is closer to the simplicity of the scattered field formulation with having the advantage of simulating dielectrics as well. The disadvantage of the formulation described here is that only the permittivity can change in the mesh but not the permeability, which is assumed equal to unity everywhere in the simulated area.

### 6.2.2 Numerical results

The formulation is applied to two structures; the square dielectric cylinder of [9] and a circular dielectric cylinder, with an analytical solution obtained from [10]. Both of the structures were also simulated with total field formulation in Chapter 4. The square has side length of 0.5 and relative permittivity 4, the circular radius 0.5 and relative permittivity 2. The computing times for the two structures are 1671.140s and 695.046s respectively. The VFU approach was used and all the rest of the parameters are as in total field formulation. The results for the BSW are shown in Figs 6.1 and 6.2. Both simulations were run for  $10^5$  timesteps and there was no instability.

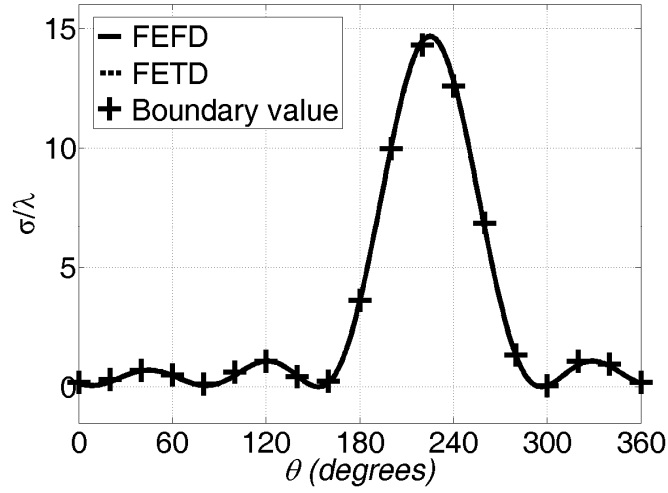


Fig. 6.1. Bistatic scattering width normalized with  $\lambda$  of the dielectric square scatterer [9] for TE

polarization,  $\theta = \phi + \pi/4$

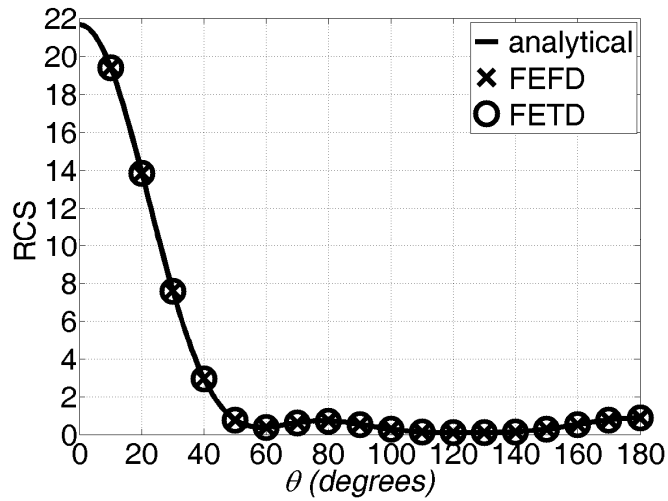


Fig. 6.2. Bistatic scattering width normalized with  $\lambda$  of the dielectric circular scatterer [10] for TE

polarization,  $\theta = \pi - \phi$ .

### 6.3 Sparse-FETD-MNRBC

The Sparse-FETD-MNRBC formulation has many things in common with the Standard-FETD-MNRBC, presented in Chapter 2; therefore the focus will be here on the differences which make it more efficient. The key differences are in the calculation of the boundary integral and its time discretisation.

The boundary integral can be efficiently calculated using the approach explained below. One important aspect of this approach is that backward difference is used for the time discretisation of the boundary integral. Thus the discretisation results to boundary terms for timesteps  $q$  and  $q-1$  but not  $q+1$  (6.35). This way the finite element matrix is sparse (6.32) unlike the standard case in Chapter 2 (2.59). The detailed formulations, the obtained results and the comparisons with the standard case are presented in the next sections.

### 6.3.1 Formulation

The weak formulation for the scattered field formulation (2.38) is

$$R = \iint_{\Omega} \left( \nabla W \bullet \nabla E_z^{sc} + \frac{1}{c^2} W \frac{\partial^2 E_z^{sc}}{\partial t^2} \right) d\Omega - \oint_{\Gamma_s} W \frac{\partial E_z^{sc}}{\partial \rho} d\Gamma = 0 \quad (6.19)$$

The time domain version of the MNRBC is

$$\left. \frac{\partial E_z^{sc}}{\partial \rho} \right|_{\rho=\rho_a} = \sum_{n=-\infty}^{\infty} e^{jn\phi} g_n(t) * \oint_{\Gamma_s} E_z^{sc}(t, \rho_a, \phi) e^{-jn\phi} d\Gamma \quad (6.20)$$

Equation (6.20) can be expressed as

$$\left. \frac{\partial E_z^{sc}}{\partial \rho} \right|_{\rho=\rho_a} = \sum_{n=-\infty}^{\infty} \psi_n(t) e^{jn\phi} \quad (6.21)$$

where

$$\psi_n(t) = g_n(t) * \oint_{\Gamma_s} E_z^{sc}(t, \rho_a, \phi) e^{-jn\phi} d\Gamma \quad (6.22)$$

When (6.21) is substituted in (6.19), one obtains

$$\iint_{\Omega} \left( \nabla W \bullet \nabla E_z^{sc} + \frac{1}{c^2} W \frac{\partial^2 E_z^{sc}}{\partial t^2} \right) d\Omega = \sum_{n=-\infty}^{\infty} \psi_n(t) \oint_{\Gamma_s} W e^{jn\phi} d\Gamma \quad (6.23)$$



Following finite element geometric discretisation of the weighted residual formulation using the Galerkin procedure, (6.33) leads to the following global matrix equation (before the inhomogeneous Dirichlet boundary condition is accounted for)

$$[\mathbf{S}^\Omega] \{\mathbf{E}_z^{sc}\} + \frac{1}{c^2} [\mathbf{T}^\Omega] \frac{d\{\mathbf{E}_z^{sc}\}}{dt^2} = \sum_{n=-\infty}^{\infty} \psi_n(t) \{\mathbf{B}^\Gamma\}_n \quad (6.24)$$

Matrices  $[\mathbf{S}^\Omega]$ ,  $[\mathbf{T}^\Omega]$  are obtained from surface elemental matrix entries and are sparse and symmetric. Their entries are identical to those of the FEFD method and can be found in [8]. Vectors  $\{\mathbf{B}^\Gamma\}_n$  are filled with entries from (2.32). Following the evaluation of (6.24) for a given set of parameter values  $(k, n, i)$  (defined in (2.32)) the result is inserted at the appropriate position in the global vectors  $\{\mathbf{B}^\Gamma\}_n$  that corresponds to the global node number of the element node number  $i$ . The assembly is similar to the assembly of row entries of matrix  $[\mathbf{P}^\Gamma]$  of the standard-FETD-MNRBC but whereas that was a matrix now it is only a vector. Using the FE geometric discretisation the integral in (6.22) can be evaluated as follows

$$\begin{aligned} \oint_{\Gamma_s} E_z^{sc}(t, \rho_a, \phi) e^{-jn\phi} d\Gamma &= \sum_{l \in \Gamma_s} \int_{\Gamma^l} \sum_{j \in \Gamma^l} N_j E_{z,j}^{sc,l} e^{-jn\phi} d\Gamma \\ &= \sum_{l \in \Gamma_s} \sum_{j \in \Gamma^l} C_{n,j}^l E_{z,j}^{sc,l} \\ &= \langle \mathbf{C}^\Gamma \rangle_n \{\mathbf{E}_z^{sc}\} \end{aligned} \quad (6.25)$$

where the entries for  $\langle \mathbf{C}^\Gamma \rangle_n$  are given from (2.33). Following the evaluation of (6.25) for a given set of parameter values  $(l, n, j)$  (defined in (2.33)) the result is multiplied with the corresponding electric field degree of freedom value.

Using a vector fitting (VF) partial fraction expansion of  $G_n(\omega)$ , for  $g_n(t)$  (2.45) and using (6.25), (6.22) leads to

$$\begin{aligned}
\psi_n(t) &= [d_n \delta(t) + h_n \delta'(t) + \sum_{m=1}^M r_{m,n} e^{a_{m,n} t}] * \sum_{l \in \Gamma_s} \sum_{j \in \Gamma^l} C_{n,j}^l E_{z,j}^{sc,l} \\
&= \sum_{l \in \Gamma_s} \sum_{j \in \Gamma^l} [d_n \delta(t) C_{n,j}^l + h_n \delta'(t) C_{n,j}^l \\
&\quad + \sum_{m=1}^M r_{m,n} e^{a_{m,n} t} C_{n,j}^l] * E_{z,j}^{sc,l}
\end{aligned} \tag{6.26}$$

Which can be rewritten as

$$\begin{aligned}
\psi_n(t) &= \sum_{l \in \Gamma_s} \sum_{j \in \Gamma^l} [d_n C_{n,j}^l E_{z,j}^{sc,l} + h_n C_{n,j}^l \frac{dE_{z,j}^{sc,l}}{dt} \\
&\quad + C_{n,j}^l \sum_{m=1}^M R_{m,n,j}(t)] \\
&= \langle \mathbf{Q}^\Gamma \rangle_n \{ \mathbf{E}_z^{sc}(t) \} + \langle \mathbf{V}^\Gamma \rangle_n \frac{d\{ \mathbf{E}_z^{sc}(t) \}}{dt} + D_n^\Gamma(t)
\end{aligned} \tag{6.27}$$

where  $R_{m,n,j}(t)$  is the same as (2.51) and the rest matrices are

$$D_n^\Gamma(t) = \sum_{l \in \Gamma_s} \sum_{j \in \Gamma^l} C_{n,j}^l \sum_{m=1}^M R_{m,n,j}(t) \tag{6.28}$$

$$Q_{n,j}^l = d_n C_{n,j}^l \tag{6.29}$$

$$V_{n,j}^l = h_n C_{n,j}^l \tag{6.30}$$

The next step is to use time discretisation in (6.24) and (6.27). Let the current time be  $t = q \Delta t$  where  $q$  is the current time step number and  $\Delta t$  is the time step interval. Newmark-beta formulation is applied in the left hand side of (6.24) while the right hand side of (6.24) is evaluated at time step  $q$ . Hence (6.24) becomes after time discretisation

$$[\mathbf{K}^\Omega] \{ \mathbf{E}_z^{sc} \}^{q+1} = \underbrace{[\mathbf{L}_1^\Omega] \{ \mathbf{E}_z^{sc} \}^q - [\mathbf{L}_2^\Omega] \{ \mathbf{E}_z^{sc} \}^{q-1} + \sum_{n=-\infty}^{\infty} \psi_n^q \{ \mathbf{B} \}_n}_{\{ \mathbf{b} \}} \tag{6.31}$$

where

$$[\mathbf{K}^\Omega] = \frac{1}{c^2 \Delta t^2} [\mathbf{T}^\Omega] + \frac{1}{4} [\mathbf{S}^\Omega] \tag{6.32}$$

$$[\mathbf{L}_1^\Omega] = \frac{2}{c^2 \Delta t^2} [\mathbf{T}^\Omega] - \frac{1}{2} [\mathbf{S}^\Omega] \quad (6.33)$$

$$[\mathbf{L}_2^\Omega] = \frac{1}{c^2 \Delta t^2} [\mathbf{T}^\Omega] + \frac{1}{4} [\mathbf{S}^\Omega] \quad (6.34)$$

Note that  $\psi_n^0 = 0$  for every  $n$ .

The global matrices  $[\mathbf{K}^\Omega]$ ,  $[\mathbf{L}_1^\Omega]$ ,  $[\mathbf{L}_2^\Omega]$  are real and are created once. They are initially assembled ignoring the inhomogeneous Dirichlet boundary condition for the incident field. Subsequently, this boundary condition is imposed following a procedure outlined in [7] by suitably modifying  $[\mathbf{K}^\Omega]$  and filling appropriate positions of  $\{\mathbf{b}\}$ , the right hand side vector of (6.31), with entries based on the incident field. These entries equal to “minus the incident field” at time step number  $q+1$ . Also updated at each time step are the function values  $\psi_n^q$  and column vectors  $\{\mathbf{E}_z^{sc}\}^q$  and  $\{\mathbf{E}_z^{sc}\}^{q-1}$ . The matrix equation (6.31) is solved using the direct matrix solver MA28 from the Harwell Subroutine Library. Note that matrix  $[\mathbf{K}^\Omega]$  is time invariant and needs to be factorized only once. When equation (6.31) is solved it provides the updated  $\{\mathbf{E}_z^{sc}\}^{q+1}$  values everywhere in the FEM region including the boundary  $\Gamma_s$ . It is these updated values of the scattered electric field on the boundary  $\Gamma_s$  that are used subsequently to obtain an updated value for each of the functions  $\psi$ , i.e.  $\psi_n^{q+1}$ , which will then be employed to calculate, by solving (6.31), the newly updated scattered field  $\{\mathbf{E}_z^{sc}\}^{q+2}$  values and so forth.

To find  $\psi_n^q$  backward difference is applied to the time derivative (6.27). Backward difference, unlike central difference, is only first order accurate [7]. Hence,

$$\begin{aligned} \psi_n^q &= \langle \mathbf{Q}^\Gamma \rangle_n \{\mathbf{E}_z^{sc}\}^q + \langle \mathbf{V}^\Gamma \rangle_n \frac{\{\mathbf{E}_z^{sc}\}^q - \{\mathbf{E}_z^{sc}\}^{q-1}}{\Delta t} + D_n^{\Gamma,q} \\ &= \left( \langle \mathbf{Q}^\Gamma \rangle_n + \frac{\langle \mathbf{V}^\Gamma \rangle_n}{\Delta t} \right) \{\mathbf{E}_z^{sc}\}^q - \frac{\langle \mathbf{V}^\Gamma \rangle_n}{\Delta t} \{\mathbf{E}_z^{sc}\}^{q-1} + D_n^{\Gamma,q} \end{aligned} \quad (6.35)$$

where  $\{\mathbf{D}^\Gamma\}^q = \{\mathbf{D}^\Gamma(t=q\Delta t)\}$  and

$$D_n^{\Gamma,q} = \sum_{l \in \Gamma_s} \sum_{j \in \Gamma^l} C_{n,j}^l \sum_{m=1}^M R_{m,n,j}^q \quad (6.36)$$

Thus, summarizing, at each time step in the Sparse-FETD-MNRBC, (6.31) is solved to find the updated  $E_z^{sc}(t)$  and obtain the updated values of  $(2N+1)$  recursive convolution functions  $\psi_n(t)$ . This updating process, alternating between equations (6.31) and (6.35) reminds of the FDTD updating process.

### 6.3.2 Numerical results

The sparse-FETD-MNRBC is applied to all three structures to which the standard-FETD-MNRBC was applied in Chapter 2. The VFG approach was used and all the parameters are as in the standard scattered field formulation. Again the results are demonstrated in terms of BSW.

Since the sparse-FETD-MNRBC uses backward differencing so that matrix  $[\mathbf{K}^\Omega]$  (6.32) remains sparse, it is expected to be less accurate for the same timestep when compared to standard-FETD-MNRBC. The circular PEC will be used to check the accuracy of the simulations for various timesteps. This is because for this structure the analytical solution is available [11].

In Fig. 6. 3 there are the BSW comparison for the PEC circle for timesteps (a) 40; (b) 10ps; (c) 5ps and (d) 1ps. In Fig.6.4 there is the error and relative error for these cases. In Fig. 6.5 there is the error and relative comparison of the standard-FETD-MNRBC for timesteps 40ps against the FEFD simulation. The error in time domain is  $e_{BSW}$  and is the difference between the analytical and the FEM solution. The relative error  $e_{rel}$  is  $e_{BSW}$  divided with the analytical solution. They are depicted as  $10\log_{10}|e_{BSW}|$  and  $10\log_{10}|e_{rel}|$  respectively. As can be seen smaller timesteps are

needed for the sparse-FETD-MNRBC to achieve the same accuracy as with the standard-FETD-MNRBC.

The advantage of the sparse approach is with the memory requirements and the time efficiency. For the standard FETD the matrices  $[\mathbf{K}^{\Omega,\Gamma}]$ ,  $[\mathbf{L}_1^{\Omega,\Gamma}]$ ,  $[\mathbf{L}_2^{\Omega,\Gamma}]$  have 23320 non-zero terms. After the application of the Dirichlet boundary,  $[\mathbf{K}^{\Omega,\Gamma}]$  has 22560 non-zero entries. For the sparse FETD these numbers are 17240 and 16480 respectively. The dimensions of the matrices are  $1160 \times 1160$  in both cases. Moreover in Table 6.1 the computing times for all the above timesteps are displayed. In all cases the total computational time is 120 ns which is the number of timesteps multiplied with the timestep.

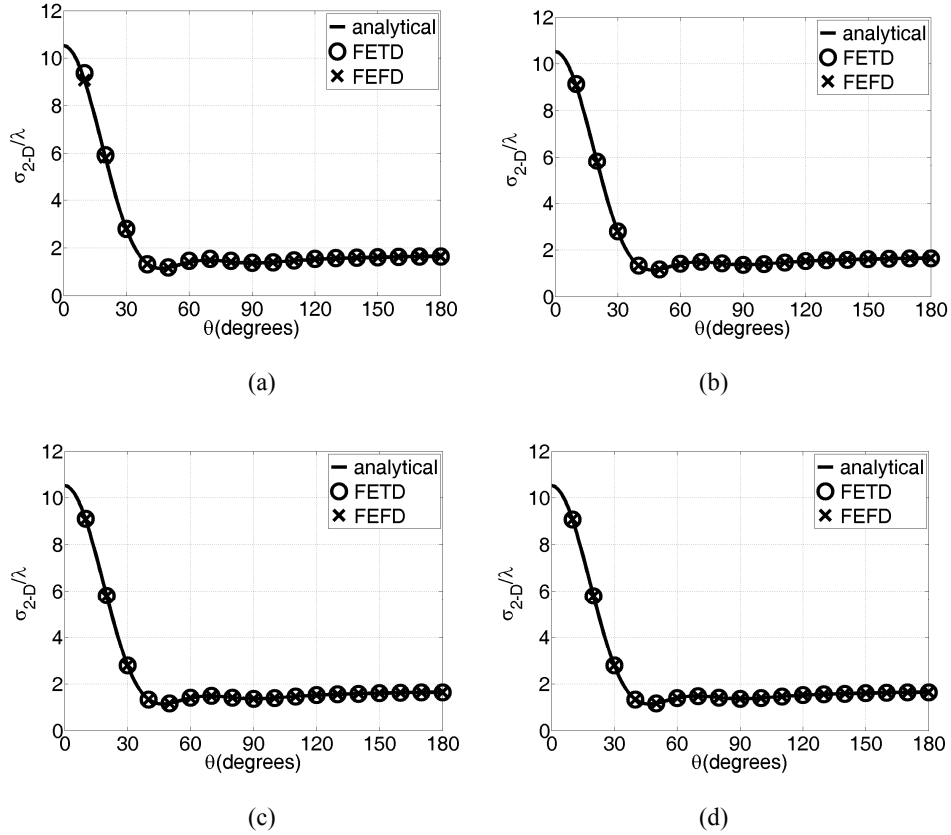


Fig. 6.3. Bistatic scattering width normalized with  $\lambda$  of the circular scatterer,  $\theta=\pi-\phi$  for (a) 40ps; (b) 10ps; (c) 5ps and (d) 1ps.

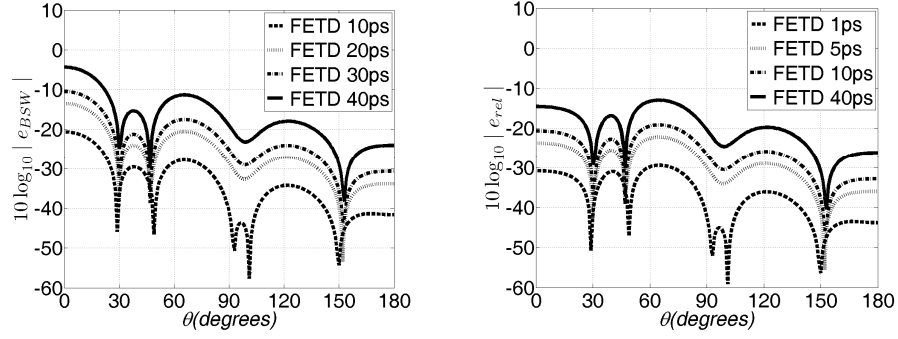


Fig. 6.4. Error and relative error of Bistatic scattering width for Sparse-FETD

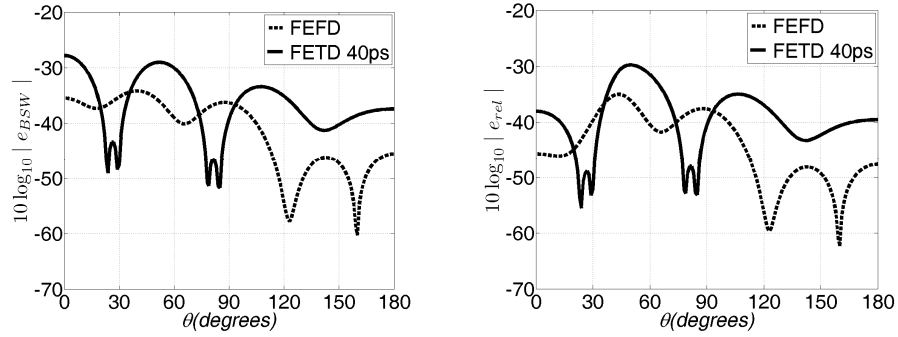


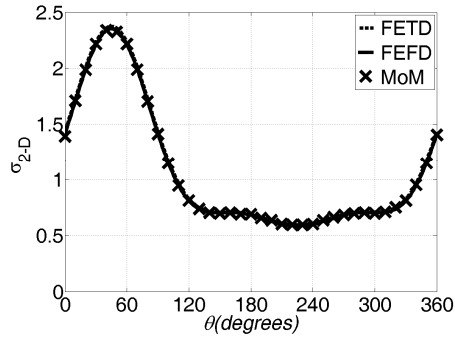
Fig. 6.5. Error and relative error of Bistatic scattering width for Standard-FETD

In Fig. 6.6 there is the BSW comparison for the PEC square scatterer, described in Fig.2.6, for timesteps (a) 25ps and (b) 5 ps. The computing times for these timesteps are 201.421s and 992.968s respectively. The comparison is held against the FEFD simulation outlined in Chapter 2 and a reference solution [10]. In Fig. 6.7 there is the BSW comparison for the PEC triangular, described in Fig.2.8, scatterer for timesteps (a) 40ps and (b) 10 ps. The computing times for these timesteps are 1098.687s and 4360.484s respectively. Again the comparison is held against the FEFD simulation and a reference solution [12]. All the rest of the parameters for all three structures are the same as in Table 2.1. The simulations for all structures were run for the largest timestep used for  $10^5$  timesteps and there was no instability.

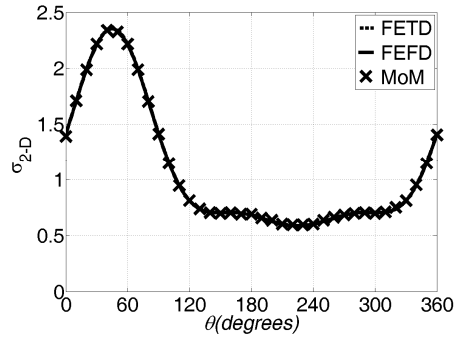
**Table 6.1**

Computing Time Comparisons

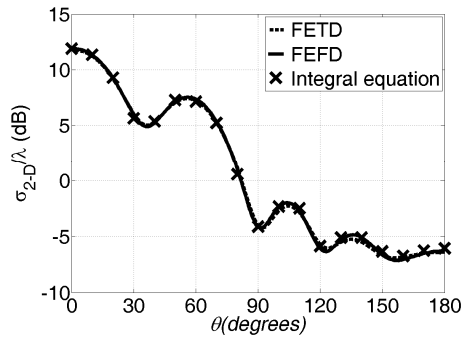
Method	$\Delta t$ (ps)	Running Time (s)
Standard-FETD	40	692.546875
Sparse-FETD	40	120.03125
Sparse-FETD	10	475.984375
Sparse-FETD	5	950.5625
Sparse-FETD	1	4834.109375



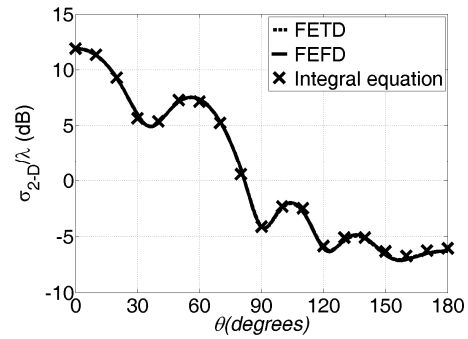
(a)



(b)

Fig. 6.6. Bistatic scattering width of the square scatterer,  $\theta=\phi-3\pi/4$ . for (a) 25ps; (b) 5ps.

(a)



(b)

Fig. 6.7. Bistatic scattering width normalized with  $\lambda$  of the triangular scatterer in dB,  $\theta=\phi-\pi$ 

for (a) 40ps; (b) 10ps.

## 6.4 Scientific contribution and future work

In this chapter the scattered field FETD-MNRBC formulation presented previously was extended for use of dielectric scatterers. Moreover for the first time a sparse-FETD-MNRBC formulation was derived and applied. This way the MNRBC was expressed with fully sparse finite element matrix and with a partially sparse/partially fully dense matrix as the standard-FETD-MNRBC.

The scattered field FETD-MNRBC formulation for dielectrics with varying permittivity showed that it is a very straightforward method in conception and application. The numerical results verified the accuracy of this approach. Therefore it is a simpler equivalent to total field formulation for specific problems. As an extension one could consider the approach of [1] in order to incorporate the continuity of the relative permeability as well. This would require the addition of an integral to the interface between the dielectric and free space. This way the approach would become more complicated and would lose the advantage of easiness against total field formulation.

The most important achievement of this chapter is the sparse-FETD-MNRBC formulation. This approach is not more difficult to apply than the standard-FETD-MNRBC. Between these two approaches there is a trade-off of efficiency and accuracy which is due to the use of backwards differencing instead of Newmark-beta for the field components. The sparse-FETD-MNRBC formulation is faster than the standard approach with less computer requirements and without much loss of accuracy.

The sparse-FETD-MNRBC was derived for scattered field cylindrical formulation. Its concept can be extended for other formulations not only from this work but for general FETD use.



## REFERENCES

- [1] I. Bardi, Z. Badics, and Z. J. Cendes, "Total and Scattered Field Formulations in the Transfinite Element Method", *IEEE Trans. on Magnetics*, vol. 44, no. 6, pp. 778-781, 2008.
- [2] A.F. Peterson and J. M. Jin, "A Two-Dimensional Time-domain Finite Element formulation for periodic structures.", *IEEE Transactions on Antennas Propag.*, vol. 53, no.4, pp. 1480-1488, 2005.
- [3] A. Taflove, S. C. Hagness, *Computational Electrodynamics: The Finite-Difference-Time Domain Method*, 2nd ed., Boston, London, Artech House, 2000.
- [4] D. M. Sullivan, *Electromagnetic Simulations Using the FDTD method*, Wiley-IEEE Press, 2000.
- [5] D.J. Riley, J.M. Jin, Z. Lou, L.E.R. Petersson, "Total and scattered field decomposition technique for the Finite-element Time-domain Method", *IEEE Transactions on Antennas Propag.*, vol. 54, no.1, pp. 35-41, 2006.
- [6] J.L. Volakis, A. Chatterjee, L.C. Kempel, *Finite Element Method for Electromagnetics, Antennas, Microwave circuits and scattering applications*, IEEE press, 1998.
- [7] J. M. Jin, *The Finite Element Method in Electromagnetics*, 2nd ed., Wiley-IEEE Press, New York, 2002.
- [8] P.P. Silvester, and R.L. Ferrari, *Finite elements for electrical engineers*, 3rd ed., Cambridge University Press, Cambridge, 1996.
- [9] A. Z. Elsherbeni and A. A. Kishk, "Modeling of cylindrical objects by circular dielectric and conducting cylinders," *IEEE Trans. Antennas Propag.*, vol. 40, pp. 96-99, Jan. 1992.

- [10] K. Umashankar, A. Taflove, *Computational Electromagnetics*, Artech House, 1993.
- [11] C.A. Balanis, *Advanced Engineering Electromagnetics*, John Wiley & Sons, 1989.
- [12] A.F. Peterson and S.P. Castillo, "A Frequency-Domain Differential Equation Formulation for Electromagnetic Scattering from Inhomogeneous Cylinders" , *IEEE Transactions on Antennas Propag.*, vol. 37, no.5, pp. 601-607, 1989.

## CHAPTER 7

### Conclusions and Future work

The main achievements of this work include the derivation and application of 2D Galerkin weighted residual FETD formulations using a cylindrical modal non-reflecting boundary condition. The formulations model plane wave scattering from cylindrical structures of arbitrary cross-sections and various materials which are surrounded by free space. The accuracy of the proposed formulations was investigated and validated in all cases through BSW comparisons of the studied structures.

Chapter 1 commenced this work by presenting its motivation and objectives. The fundamental concepts regarding cylindrical structures and their mathematical background were described here. Moreover key points of the FEM were outlined with focus on the Galerkin weighted residual procedure. The chapter closed with the presentation of possible applications of cylindrical structures.

Chapter 2 presented a novel 2D FETD-MNRBC Galerkin weighted residual scattered field formulation for TE polarisation. The formulation was aimed for PEC scatterers of arbitrary cross-section. The formulation was based on a VF approximation of the cylindrical kernel. It did not show any sign of instability. Numerical results validated the correct functioning of the formulation. The results of the FETD implementation of the method were compared with their FEFD equivalents and results from the literature or analytical ones. In all cases the results were compared in terms of BSW.

Chapter 3 elaborated on the VF approximation of the cylindrical boundary kernel. As it was shown there are two approaches to the approximation the VFG and

VFU. The VGU is the generic form of the VFG. Both were proven accurate with the VFU being more versatile. Furthermore this chapter experimented on the various parameters that affect the accuracy of the VF approximation and compared the VF approximation results with approximation results from the literature.

Chapter 4 proceeds to a novel total field implementation of the 2D FETD-MNRBC Galerkin weighted residual formulation. Here the VFU approximation approach is used. The formulations for both TE and TM polarisations are derived. The studied scatterers here include both PEC and dielectric ones. Again the comparisons of the BSW of FETD results is held against FEFD ones and results from the literature and analytical ones. This formulation is proven accurate as well.

Chapter 5 presented for the first time a periodic 2D FETD-MNRBC formulation for cylindrical scatterers with azimuthal periodicity. This formulation required the use of the Floquet theorem along with a decomposition of the incident field in modal harmonics. This approach allows the simulations to be applied to a single unit-cell, one period of the structure and not the whole cross-section. Some key points of this approach are the fact that the incident field harmonics are approximated with VF and that the final matrix system solved was complex. This method is an elegant and sophisticated way to simulate angular periodic structures and its accuracy was validated though BSW comparisons.

Chapter 6 presented scattered field formulation for dielectrics and a sparse FETD-MNRBC formulation. The scattered field formulation considered in the previous chapters has the limitation that can be applied to PEC cylinders only. Based on the recent literature this disadvantage can be overcome. A scattered field formulation for cylinders or varying permittivity utilized the MNRBC is demonstrated. Furthermore in this chapter an important aspect of the FETD-MNRBC is investigated.

The FETD-MNRBC described in the previous chapters has the disadvantage that it requires fully dense submatrices for the boundary integral. This was alleviated with the use of the proposed sparse FETD-MNRBC algorithm. This algorithm requires smaller timestep but is more memory and time efficient. The proposed methodology is validated through BSW numerical results and comparisons.

Chapter 7 concludes the dissertation and summarizes the main achievements of this research work.

Future work should focus on generalisation to 3D Galerkin weighted residual FETD formulations using a modal non-reflecting boundary condition. To this direction the formulations derived in this dissertation and also the analysis and discussion on time efficiency and the unit-cell approach would be significant. An interesting aspect of 3D study is the simulation of plane wave scattering from axially periodic structures using a unit-cell approach [1] for the FETD method. This unit-cell approach could be further extended for structures that have both azimuthal and axial periodicity [2].

## REFERENCES

- [1] A. Freni, C. Mias, R.L. Ferrari, "Hybrid Finite-Element analysis of Electromagnetic Plane Wave Scattering from Axially Periodic Cylindrical Structures", *IEEE Trans. Antennas Propag.* vol. 46, no. 12, pp.1859-1866, Dec. 1998.
- [2] T. Cwik, "Coupling into and Scattering from Cylindrical Structures Covered Periodically with Metallic Patches", *IEEE Trans. Antennas Propag.* vol. 38, no. 2, pp.220-226, Feb. 1990.

## Appendix A

### Scattered field harmonics

The Helmholtz equation in the free space surrounding the cylinder for the scattered field component will be

$$\nabla \cdot \frac{1}{p_r} \nabla \tilde{\Phi}^{sc} + k_0^2 q_r \tilde{\Phi}^{sc} = 0 \quad (\text{A.1})$$

Where  $p_r = \epsilon_r$ ,  $q_r = \mu_r$  for TE excitation and  $p_r = \epsilon_r$ ,  $q_r = \mu_r$  for TM excitation. The field component  $\Phi^{sc}$  represents the scattered electric field component  $E_z$  for TE modes and the scattered magnetic field component  $H_z$  for TM modes. The field component  $\Phi^{inc}$  represents incident field component. The ‘ $\sim$ ’ denotes that the variable is in the frequency domain. The parameter  $k_0 = \omega/c$  is the wavenumber in free space,  $\omega$  is the angular frequency and  $c$  is the speed of light in free space. Equation (A.1) will be solved for the area surrounding the cylindrical structure which is free space, thus (A.1) reduces for both polarizations to

$$\nabla^2 \tilde{\Phi}^{sc} + k_0^2 \tilde{\Phi}^{sc} = 0 \quad (\text{A.2})$$

For two dimensional analysis, equation (A.2) can be written in polar coordinates as

$$\frac{1}{\rho} \frac{\partial}{\partial \rho} \left( \rho \frac{\partial \tilde{\Phi}^{sc}}{\partial \rho} \right) + \frac{1}{\rho^2} \frac{\partial^2 \tilde{\Phi}^{sc}}{\partial \phi^2} + k_0^2 \tilde{\Phi}^{sc} = 0 \quad (\text{A.3})$$

Or

$$\frac{\partial^2 \tilde{\Phi}^{sc}}{\partial \rho^2} + \frac{1}{\rho} \frac{\partial \tilde{\Phi}^{sc}}{\partial \rho} + \frac{1}{\rho^2} \frac{\partial^2 \tilde{\Phi}^{sc}}{\partial \phi^2} + k_0^2 \tilde{\Phi}^{sc} = 0 \quad (\text{A.4})$$

where  $\rho$  is the radial distance from the centre and  $\phi$  the azimuthal angle as depicted in Fig. 1.2.

Equation (A.4) will be solved with the method of separation of variables. Assuming that the solution can be written as

$$\tilde{\Phi}^{sc}(\rho, \phi) = R(\rho)F(\phi) \quad (\text{A.5})$$

By replacing (A.5) into (A.4) and dividing by  $R \cdot F$  it is obtained

$$\frac{R''}{R} + \frac{1}{\rho} \frac{R'}{R} + \frac{1}{\rho^2} \frac{F''}{F} + k_0^2 = 0 \quad (\text{A.6})$$

And by multiplying (A.6) with  $\rho^2$  it is

$$\rho^2 \frac{R''}{R} + \rho \frac{R'}{R} + k_0^2 \rho^2 + \frac{F''}{F} = 0 \quad (\text{A.7})$$

The first three terms of (A.7) are function only of  $\rho$  and the last one only of  $\phi$  thus it can be written that

$$\frac{F''}{F} = c_F \quad (\text{A.8})$$

where  $c_F$  is a constant. The phase is allowed to vary linearly around the cylinder as in [1]. This means than  $F(\phi)$  should include a term  $\exp(jv_m\phi)$  multiplied by a constant. Thus it is set

$$c = (jv_m)^2 \quad (\text{A.9})$$

So the solution of (A.8) will be

$$F = M_{v_m} e^{jv_m\phi} + N_{v_m} e^{-jv_m\phi} \quad (\text{A.10})$$

And because it must have the exponential form described above it reduces to

$$F = F_{v_m} e^{jv_m\phi} \quad (\text{A.11})$$

All cylindrical structures are by default periodic with period  $2\pi$  thus  $v_m$  should be an integer [2 p.119] so that the solution satisfies

$$\tilde{\Phi}^{sc}(\rho, \phi) = \tilde{\Phi}^{sc}(\rho, \phi \pm 2v_m\pi) \quad (\text{A.12})$$

By replacing (A.9) and (A.8) to (A.7), it becomes



$$\rho^2 \frac{R''}{R} + \rho \frac{R'}{R} + k_0^2 \rho^2 - v_m^2 = 0 \quad (\text{A.13})$$

Or

$$R'' + \frac{1}{\rho} R' + \left( k_0^2 - \frac{v_m^2}{\rho^2} \right) R = 0 \quad (\text{A.14})$$

This is the Bessel equation and the solution will have the form [3 p. 119]

$$R(\rho) = C_{v_m} J_{v_m}(k_0 \rho) + D_{v_m} Y_{v_m}(k_0 \rho) \quad (\text{A.15})$$

or

$$R(\rho) = C_{v_m} H_{v_m}^{(1)}(k_0 \rho) + D_{v_m} H_{v_m}^{(2)}(k_0 \rho) \quad (\text{A.16})$$

where  $J_{v_m}$  and  $Y_{v_m}$  represent the Bessel and the modified Bessel functions of order  $v_m$  respectively and  $H_{v_m}^{(1)}$ ,  $H_{v_m}^{(2)}$  the Hankel functions of the first and the second kind respectively. Equation (A.1) is solved for the area surrounding the cylinder, where the scattered field will travel from the cylinder to infinity. So there will be travelling waves in the free space and the solution that describes travelling waves is (A.16) [3 p.120 ]. Moreover these travelling waves, since they represent the scattered field will have direction towards  $+\rho$  travel, so the solution will require only the second order Hankel [3 p. 121].

Thus

$$R(\rho) = D_{v_m} H_{v_m}^{(2)}(k_0 \rho) \quad (\text{A.17})$$

So the solution will be:

$$R(\rho)F(\phi) = M_{v_m} D_{v_m} H_{v_m}^{(2)}(k_0 \rho) e^{iv_m \phi} \quad (\text{A.18})$$

or

$$R \cdot F = A_{v_m} H_{v_m}^{(2)}(k_0 \rho) e^{iv_m \phi} \quad (\text{A.19})$$

This is a particular solution. The general solution will be a summation for all values of  $v_m$ . So it will be

$$\tilde{\Phi}^{sc}(\rho, \phi) = \sum_{v_m=-\infty}^{\infty} A_{v_m} H_{v_m}^{(2)}(k_0 \rho) e^{jv_m \phi} \quad (\text{A.20})$$

Use of (A.20) is made in the main text where the modal nonreflecting boundary condition is derived and applied to finite element simulations.

## REFERENCES

- [1] T. Cwik, "Coupling into and Scattering from Cylindrical Structures Covered Periodically with Metallic Patches", *IEEE Trans. Antennas Propag.* vol. 38, no. 2, pp.220-226, Feb. 1990.
- [2] D. M. Pozar, *Microwave engineering*, 3<sup>rd</sup>, John Wiley & Sons, 2006.
- [3] C.A. Balanis, *Advanced Engineering Electromagnetics*, John Wiley & Sons, 1989.

## Appendix B

### First order absorbing boundary condition derivation

This appendix shows how the first order boundary condition [1,2] can be derived from the scattered field pattern. As shown in [3] the scattered field from a cylindrical structure is given by

$$\tilde{\Phi}^{sc}(\rho, \phi) = \sum_{v_m=-\infty}^{\infty} A_{v_m} H_{v_m}^{(2)}(k_0 \rho) e^{j v_m \phi} \quad (\text{B.1})$$

By replacing the Hankel function of the second kind with its large argument approximation of [3 p. 935]

$$H_{v_m}^{(2)}(k_0 \rho) \approx \sqrt{\frac{2}{\pi k_0 \rho}} e^{-j[k_0 \rho - v_m(\pi/2) - \pi/4]}, k_0 \rho \rightarrow \infty \quad (\text{B.2})$$

Equation (B.1) becomes for  $k_0 \rho \rightarrow \infty$

$$\tilde{\Phi}^{sc}(\rho, \phi) \approx \sum_{v_m=-\infty}^{\infty} A_{v_m} \sqrt{\frac{2}{\pi k_0 \rho}} e^{-j[k_0 \rho - v_m(\pi/2) - \pi/4]} e^{j v_m \phi} \quad (\text{B.3})$$

The derivative of the scattered field with respect to the radius  $\rho$  will be

$$\frac{\partial \tilde{\Phi}^{sc}(\rho, \phi)}{\partial \rho} \approx \sum_{v_m=-\infty}^{\infty} A_{v_m} \frac{\partial \left( \sqrt{\frac{2}{\pi k_0 \rho}} e^{-j[k_0 \rho - v_m(\pi/2) - \pi/4]} \right)}{\partial \rho} e^{j v_m \phi} \quad (\text{B.4})$$

It is

$$\frac{\partial \left( \sqrt{\frac{2}{\pi k_0 \rho}} e^{-j[k_0 \rho - v_m(\pi/2) - \pi/4]} \right)}{\partial \rho} = \left( -\frac{1}{2\rho} - j k_0 \right) \sqrt{\frac{2}{\pi k_0 \rho}} e^{-j[k_0 \rho - v_m(\pi/2) - \pi/4]} \quad (\text{B.5})$$

So (B.4) becomes

$$\frac{\partial \tilde{\Phi}^{sc}(\rho, \phi)}{\partial \rho} \approx \sum_{v_m=-\infty}^{\infty} A_{v_m} \left( -\frac{1}{2\rho} - j k_0 \right) \sqrt{\frac{2}{\pi k_0 \rho}} e^{-j[k_0 \rho - v_m(\pi/2) - \pi/4]} e^{j v_m \phi} \quad (\text{B.6})$$

Or

$$\frac{\partial \tilde{\Phi}^{sc}(\rho, \phi)}{\partial \rho} \approx \left( -\frac{1}{2\rho} - jk_0 \right) \sum_{v_m=-\infty}^{\infty} A_{v_m} \sqrt{\frac{2}{\pi k_0 \rho}} e^{-j[k_0 \rho - v_m(\pi/2) - \pi/4]} e^{jv_m \phi} \quad (\text{B.7})$$

and finally

$$\frac{\partial \tilde{\Phi}^{sc}(\rho, \phi)}{\partial \rho} \approx \left( -\frac{1}{2\rho} - jk_0 \right) \tilde{\Phi}^{sc}(\rho, \phi) \quad (\text{B.8})$$

which is the first order absorbing boundary condition.

## REFERENCES

- [1] J. M. Jin, *The Finite Element Method in Electromagnetics*, 2nd ed., Wiley-IEEE Press, New York, 2002.
- [2] J.L. Volakis, A. Chatterjee, L.C. Kempel, *Finite Element Method for Electromagnetics, Antennas, Microwave circuits and scattering applications*, IEEE press, 1998.
- [3] C.A. Balanis, *Advanced Engineering Electromagnetics*, John Wiley & Sons, 1989.

## Appendix C

### Matrices entries

This appendix shows the final form of the matrices used in Chapters 2 and 4 after the 5-point Gaussian quadrature formula is applied. As shown in (2.29) the global matrix equation for the scattered field formulation is

$$\underbrace{[[\mathbf{S}^\Omega] - k_0^2[\mathbf{T}^\Omega] + [\mathbf{P}^\Gamma]]}_{[\mathbf{M}^{\Omega,\Gamma}]} \{\tilde{\mathbf{E}}_z^{sc}\} = \{\mathbf{F}\} \quad (\text{C.1})$$

And for the total field formulation (4.19)

$$\underbrace{[[\mathbf{S}_{p_r}^\Omega] - k_0^2[\mathbf{T}_{p_r}^\Omega] + [\mathbf{P}^\Gamma]]}_{[\mathbf{M}_{p_r,q_r}^{\Omega,\Gamma}]} \{\tilde{\Phi}^t\} = \underbrace{[[\mathbf{O}^\Gamma] - [\mathbf{P}^\Gamma]]}_{[\mathbf{M}^{\Omega,\Gamma}]} \{\tilde{\Phi}^{inc}\} \quad (\text{C.2})$$

The entries of the surface elemental matrices that constitute  $[\mathbf{S}^\Omega]$  and  $[\mathbf{T}^\Omega]$  are [1 pp.288-289]

$$\begin{aligned} S_{ij}^{\Omega^e} &= \iint_{\Omega^e} \nabla N_i(u, v) \cdot \nabla N_j(u, v) d\Omega = \\ &= \int_{-1}^1 \int_{-1}^1 \left( \frac{\partial N_i}{\partial x} \frac{\partial N_j}{\partial x} + \frac{\partial N_i}{\partial y} \frac{\partial N_j}{\partial y} \right) \det(\mathbf{J}) du dv \\ &= \int_{-1}^1 \int_{-1}^1 \left\{ \left( \frac{\partial N_i}{\partial u} \frac{\partial u}{\partial x} + \frac{\partial N_i}{\partial v} \frac{\partial v}{\partial x} \right) \times \left( \frac{\partial N_j}{\partial u} \frac{\partial u}{\partial x} + \frac{\partial N_j}{\partial v} \frac{\partial v}{\partial x} \right) + \right. \\ &\quad \left. + \left( \frac{\partial N_i}{\partial u} \frac{\partial u}{\partial y} + \frac{\partial N_i}{\partial v} \frac{\partial v}{\partial y} \right) \times \left( \frac{\partial N_j}{\partial u} \frac{\partial u}{\partial y} + \frac{\partial N_j}{\partial v} \frac{\partial v}{\partial y} \right) \right\} \det(\mathbf{J}) du dv \\ &= \int_{-1}^1 \int_{-1}^1 (\mathbf{D}_{uv} N_i)^T \mathbf{J}^{-T} \mathbf{J}^{-1} (\mathbf{D}_{uv} N_j) \det(\mathbf{J}) du dv \end{aligned} \quad (\text{C.3})$$

$$T_{ij}^{\Omega^e} = \iint_{\Omega^e} N_i(u, v) N_j(u, v) d\Omega = \int_{-1}^1 \int_{-1}^1 N_i N_j \det(\mathbf{J}) du dv \quad (\text{C.4})$$

where  $\Omega^e$  is the surface area region of each curvilinear surface element and  $\det(\mathbf{J})$  is the determinant of the Jacobian matrix  $\mathbf{J}$ . The superscript ‘T’ denotes the transpose and ‘-T’ the inverse transpose. The Jacobian matrix  $\mathbf{J}$ , its inverse  $\mathbf{J}^{-1}$  and the operator  $\mathbf{D}_{uv}$  are defined as, [1 p.280 and p.289],

$$\mathbf{J} = \begin{bmatrix} \frac{\partial x}{\partial u} & \frac{\partial y}{\partial u} \\ \frac{\partial x}{\partial v} & \frac{\partial y}{\partial v} \end{bmatrix}, \quad \mathbf{J}^{-1} = \begin{bmatrix} \frac{\partial u}{\partial x} & \frac{\partial v}{\partial x} \\ \frac{\partial u}{\partial y} & \frac{\partial v}{\partial y} \end{bmatrix}, \quad \mathbf{D}_{uv} = \begin{bmatrix} \frac{\partial}{\partial u} \\ \frac{\partial}{\partial v} \end{bmatrix} \quad (\text{C.5})$$

The determinant of the Jacobian matrix is evaluated, for a given element, by making use of equation (2.25). Note that a unique relation between the  $x$ - $y$  and  $u$ - $v$  coordinate systems must exist i.e. the elements must not be much distorted.

The entries of the surface elemental matrices that constitute  $[\mathbf{S}_p^\Omega]$  and  $[\mathbf{T}_q^\Omega]$  for the total field formulation will be related with  $[\mathbf{S}^\Omega]$  and  $[\mathbf{T}^\Omega]$  with

$$S_{p,ij}^{\Omega^e} = \frac{1}{p_r^e} S_{ij}^{\Omega^e} \quad (\text{C.6})$$

$$T_{q,ij}^{\Omega^e} = q_r^e T_{ij}^{\Omega^e} \quad (\text{C.7})$$

where  $p_r^e$  and  $q_r^e$  denote the values of the elemental  $p$  and  $q$  parameters.

In this work the integrations of (C.3), (C.4), (2.32), (2.33) and (4.21) are evaluated numerically with the use of a 5-point Gaussian quadrature formula [1 pp.290-291] as follows

$$S_{ij}^{\Omega^e} = \sum_{\xi=1}^5 \sum_{\eta=1}^5 w_\xi w_\eta [\mathbf{D}_{uv} N_i(u_\xi, v_\eta)]^T \mathbf{J}^{-T}(u_\xi, v_\eta) \times \mathbf{J}^{-1}(u_\xi, v_\eta) [\mathbf{D}_{uv} N_j(u_\xi, v_\eta)] \det[\mathbf{J}(u_\xi, v_\eta)] \quad (\text{C.8})$$

$$T_{ij}^{\Omega^e} = \sum_{\xi=1}^5 \sum_{\eta=1}^5 w_\xi w_\eta N_i(u_\xi, v_\eta) N_j(u_\xi, v_\eta) \det[\mathbf{J}(u_\xi, v_\eta)] \quad (\text{C.9})$$

$$B_{n,i}^k = \sum_{\xi=1}^5 w_\xi N_i^k(u_\xi) \exp \left[ jn \times \sin^{-1} \left( \frac{\sum_{p=1}^3 N_p(u_\xi) y_p}{\rho_a} \right) \right] J_s(u_\xi) \quad (\text{C.10})$$

$$C_{n,j}^l = \sum_{\xi=1}^5 w_\xi N_j^l(u_\xi) \exp \left[ -jn \times \sin^{-1} \left( \frac{\sum_{p=1}^3 N_p(u_\xi) y_p}{\rho_a} \right) \right] J_s(u_\xi) \quad (\text{C.11})$$

$$O_{ij}^k = \sum_{\xi=1}^5 w_\xi N_i^k(u_\xi) N_j^k(u_\xi) jk_0 \cos \left( \sin^{-1} \left( \frac{\sum_{p=1}^3 N_p(u_\xi) y_p}{\rho_a} \right) \right) J_s(u_\xi) \quad (\text{C.12})$$

The Gaussian quadrature weights  $w_{\xi,\eta}$  and points  $u_{\xi,\eta}$  are tabulated in [1 p.292]. After the values of the above matrices are calculated are then appropriately assembled to the global matrix (C.1) or (C.2).

## REFERENCES

- [1] P.P. Silvester, and R.L. Ferrari, *Finite elements for electrical engineers*, 3rd ed., Cambridge University Press, Cambridge, 1996.

## Appendix D

### Limits of functions $U_n$ and $G_n$

Firstly the asymptotic value of  $U_n(s)$  (3.8) as  $s \rightarrow 0$  will be found. It is

$$U_n(s) = s + \frac{1}{2} + s \frac{\frac{\partial K_n(s)}{\partial s}}{K_n(s)} \quad (\text{D.1})$$

$$U_n(s) = s + \frac{1}{2} - s \frac{K_{n+1}(s)}{K_n(s)} + n \quad (\text{D.2})$$

For  $n > 0$  the small argument approximation is [1 p.375]

$$K_n(s) \approx \frac{1}{2} \Gamma(n) \left( \frac{1}{2} s \right)^{-n} \quad (\text{D.3})$$

In this case  $n$  is integer so Gamma function will be

$$\Gamma(n+1) = n! \text{ and } \Gamma(n) = (n-1)!$$

So

$$\frac{\Gamma(n+1)}{\Gamma(n)} = n \quad (\text{D.4})$$

Thus the limit will be

$$\lim_{s \rightarrow 0} (u_n(s)) = \lim_{s \rightarrow 0} \left( s + \frac{1}{2} - s \frac{\frac{1}{2} \Gamma(n+1) \left( \frac{1}{2} s \right)^{-n-1}}{\frac{1}{2} \Gamma(n) \left( \frac{1}{2} s \right)^{-n}} + n \right) = \frac{1}{2} - n \quad (\text{D.5})$$

For  $n = 0$  the small argument approximation is [1 p.375]

$$K_0(s) \approx -\ln(s) \quad (\text{D.6})$$



$$\lim_{s \rightarrow 0}(U_0(s)) = \lim_{s \rightarrow 0} \left( s + \frac{1}{2} - s \frac{\frac{1}{2} \Gamma(1) \left( \frac{1}{2} s \right)^{-1}}{-\ln(s)} + 0 \right) \quad (\text{D.7})$$

$$\lim_{s \rightarrow 0}(U_0(s)) = \lim_{s \rightarrow 0} \left( s + \frac{1}{2} + \frac{1}{\ln(s)} \right) \quad (\text{D.8})$$

And because

$$\lim_{s \rightarrow 0}(1/\ln(s)) = 0 \quad \text{since} \quad \lim_{s \rightarrow 0}(\ln(s)) = -\infty \quad (\text{D.9})$$

$$\lim_{s \rightarrow 0}(U_0(s)) = \frac{1}{2} \quad (\text{D.10})$$

Again from [1 p.375] it is

$$K_{-n}(s) = K_n(s) \quad (\text{D.11})$$

So for  $n < 0$

$$K_n(s) = K_{-|n|}(s) = K_{|n|}(s) \quad (\text{D.12})$$

and

$$\frac{\partial K_n(s)}{\partial s} = \frac{\partial K_{|n|}(s)}{\partial s} \quad (\text{D.13})$$

So it will be

$$\lim_{s \rightarrow 0}(U_n(s)) = \lim_{s \rightarrow 0}(U_{|n|}(s)) = \frac{1}{2} - |n| \quad (\text{D.14})$$

and because for  $n > 0$  it is  $n = |n|$  and for  $n = 0$  it is  $|n| = 0$ , it can be said that for every  $n$  it is

$$\lim_{s \rightarrow 0}(U_n(s)) = \frac{1}{2} - |n| \quad (\text{D.15})$$

Now the large argument approximation of  $U_n(s)$  will be found.

From [2 p. 937], for  $s \rightarrow \infty$  it is

$$K_n(s) \approx \sqrt{\frac{\pi}{2s}} e^{-s} \quad (\text{D.16})$$

The derivative will be

$$\frac{\partial K_n(s)}{\partial s} \approx \left( \sqrt{\frac{\pi}{2s}} e^{-s} \right)' = -\frac{1}{2s} \sqrt{\frac{\pi}{2s}} e^{-s} - \sqrt{\frac{\pi}{2s}} e^{-s} \quad (\text{D.17})$$

So the limit of  $U_n$  will be

$$\lim_{s \rightarrow \infty} (U_n(s)) = \lim_{s \rightarrow \infty} \left( s + \frac{1}{2} + s \left( \frac{-\frac{1}{2s} \sqrt{\frac{\pi}{2s}} e^{-s} - \sqrt{\frac{\pi}{2s}} e^{-s}}{\sqrt{\frac{\pi}{2s}} e^{-s}} \right) \right) \quad (\text{D.18})$$

$$\lim_{s \rightarrow \infty} (U_n(s)) = \lim_{s \rightarrow \infty} \left( s + \frac{1}{2} + s \left( -\frac{1}{2s} - 1 \right) \right) \quad (\text{D.19})$$

$$\lim_{s \rightarrow \infty} (U_n(s)) = \lim_{s \rightarrow \infty} \left( s + \frac{1}{2} - \frac{1}{2} - s \right) \quad (\text{D.20})$$

$$\lim_{s \rightarrow \infty} (U_n(s)) = 0 \quad (\text{D.21})$$

The limits for the  $G_n$  coefficients (2.24) can be found in a similar way. From [1 p.360], for  $k_0 \rho \rightarrow 0$  it is

$$jH_n^{(2)}(k_0 \rho) \approx \left( -\frac{1}{\pi} \right) \Gamma(n) \left( \frac{1}{2} k_0 \rho \right)^{-n} \quad (\text{D.22})$$

Firstly when  $n > 0$

$$\lim_{\omega \rightarrow 0} (G_n(\omega)) = \lim_{\omega \rightarrow 0} \left( \frac{-k_0}{2\pi\rho} \cdot \frac{j\left(\frac{1}{\pi}\right)\Gamma(n+1)\left(\frac{1}{2}k_0\rho\right)^{-n-1}}{j(1/\pi)\Gamma(n)\left(\frac{1}{2}k_0\rho\right)^{-n}} + \frac{n}{2\pi\rho^2} \right) \quad (\text{D.23})$$

Equation (D.23) will become

$$\lim_{\omega \rightarrow 0} (G_n(\omega)) = \lim_{\omega \rightarrow 0} \left( \frac{-k_0}{2\pi\rho} \cdot \frac{n}{\frac{1}{2}k_0\rho} + \frac{n}{2\pi\rho^2} \right) \quad (\text{D.24})$$

$$\lim_{\omega \rightarrow 0} (G_n(\omega)) = \lim_{\omega \rightarrow 0} \left( -\frac{n}{\pi \rho^2} + \frac{n}{2\pi \rho^2} \right) \quad (\text{D.25})$$

And finally

$$\lim_{k_0 \rho_a \rightarrow 0} (G_n(\omega)) = -\frac{n}{2\pi \rho} \quad (\text{D.26})$$

Now when  $n = 0$  from [1], for  $k_0 \rho \rightarrow 0$  it is

$$\text{j}H_0^{(2)}(k_0 \rho) \approx \left( \frac{2}{\pi} \right) \ln(k_0 \rho) \quad (\text{D.27})$$

$$\lim_{\omega \rightarrow 0} (G_0(\omega)) = \lim_{\omega \rightarrow 0} \left( \frac{-k_0}{2\pi \rho} \cdot \frac{\text{j} \left( \frac{1}{\sqrt{\pi}} \right) \Gamma(1) \left( \frac{1}{2} k_0 \rho \right)^{-1}}{\left( -\text{j} \frac{2}{\pi} \right) \ln(k_0 \rho)} \right) \quad (\text{D.28})$$

$$\lim_{\omega \rightarrow 0} (G_0(\omega)) = \lim_{\omega \rightarrow 0} \left( \frac{k_0}{2\pi \rho} \cdot \frac{1}{2 \frac{1}{2} k_0 \rho_a \ln(k_0 \rho)} \right) \quad (\text{D.29})$$

$$\lim_{\omega \rightarrow 0} (G_0(\omega)) = \lim_{\omega \rightarrow 0} \left( \frac{1}{2\pi \rho^2 \ln(k_0 \rho)} \right) \quad (\text{D.30})$$

$$\lim_{k_0 \rho_a \rightarrow 0} (G_0(k_0 \rho)) = 0 \quad (\text{D.31})$$

And when  $n < 0$  from [1 p.358] equation 9.1.6 it is

$$H_n^{(2)}(k_0 \rho) = H_{-|n|}^{(2)}(k_0 \rho) = e^{-\text{j}|n|\pi} H_{|n|}^{(2)}(k_0 \rho) \quad (\text{D.32})$$

And by taking the derivative of (D.32) over  $\rho$

$$\frac{\partial H_n^{(2)}(k_0 \rho)}{\partial \rho} = e^{-\text{j}|n|\pi} \frac{H_{|n|}^{(2)}(k_0 \rho)}{\partial \rho} \quad (\text{D.33})$$

Therefore it is

$$G_n(\omega) = \frac{1}{2\pi\rho} \frac{e^{-j|n|\pi} \left( \frac{\partial H_{|n|}^{(2)}(k_0\rho)}{\partial \rho} \right)}{e^{-j|n|\pi} H_{|n|}^{(2)}(k_0\rho)} = G_{|n|}(\omega) \quad (\text{D.34})$$

One important conclusion from (D.34) which is used in the main text is that

$$G_n(\omega) = G_{-n}(\omega) \quad (\text{C.35})$$

By combining (D.26),(D.31) and (D.34) we can say that for every  $n$  it is

$$\lim_{\omega \rightarrow 0} (G_n(\omega)) = -\frac{|n|}{2\pi\rho} \quad (\text{D.36})$$

The large argument approximation for the Hankel function of the second kind is [2 p.606]

$$H_n^{(2)}(k_0\rho) \approx \sqrt{\frac{2j}{\pi k_0\rho}} j^n e^{-jk_0\rho} \quad (\text{D.37})$$

Thus it will be

$$\frac{\partial H_n^{(2)}(k_0\rho)}{\partial \rho} \approx \left( -\frac{1}{2}\rho - jk_0 \right) \sqrt{\frac{2j}{\pi k_0\rho}} j^n e^{-jk_0\rho} = \left( -\frac{1}{2}\rho - jk_0 \right) H_n^{(2)}(k_0\rho) \quad (\text{D.38})$$

So the large argument approximation of  $G_n$  will be

$$G_n(\omega) = \frac{1}{2\pi\rho} \frac{\frac{\partial H_n^{(2)}(k_0\rho)}{\partial \rho}}{H_n^{(2)}(k_0\rho)} = \frac{1}{2\pi\rho} \left( -\frac{1}{2}\rho - jk_0 \right) = -\frac{jk_0}{2\pi\rho} - \frac{1}{4\pi\rho^2} \quad (\text{D.39})$$

or

$$G_n(\omega) = -\frac{s}{2\pi\rho c} - \frac{1}{4\pi\rho^2} \quad (\text{D.40})$$

## REFERENCES

- [1] M. Abramowitz and I.A. Stegun, Handbook of Mathematical Functions: With Formulas, Graphs, and Mathematical Tables, Dover Publications, New York, 1965.
- [2] C.A. Balanis, *Advanced Engineering Electromagnetics*, John Wiley & Sons, 1989

## Appendix E

### Mathematical details of periodic formulations

This appendix includes the mathematical details regarding the periodic FEFD-MNRBC and FETD-MNRBC formulations.

The orders of the incident ( $v_0$ ) and scattered ( $v_m$ ) field harmonics are connected with (5.4)

$$v_m = \frac{2\pi}{T_\phi} m_0 + v_0, \quad m_0 = 0, \pm 1, \pm 2, \dots \quad (\text{E.1})$$

This is obtained from the cylindrical periodic condition. This is (5.3)

$$\tilde{\Phi}_z^{v_0}(\rho, \phi + T_\phi) = \tilde{\Phi}_z^{v_0}(\rho, \phi) e^{jv_0 T_\phi} \quad (\text{E.2})$$

By applying (E.2) to any order of the scattered field (5.2) it is obtained

$$A_{v_m} H_{v_m}^{(2)}(k_0 \rho) e^{jv_m(\phi + T_\phi)} = A_{v_m} H_{v_m}^{(2)}(k_0 \rho) e^{jv_m \phi} e^{jv_0 T_\phi} \quad (\text{E.3})$$

$$e^{jv_m(\phi + T_\phi)} = e^{j(v_m \phi + v_0 T_\phi)} \quad (\text{E.4})$$

$$e^{j(v_m T_\phi - v_0 T_\phi)} = 1 \quad (\text{E.5})$$

So it will be:

$$v_m T_\phi - v_0 T_\phi = m_0 2\pi \quad (\text{E.6})$$

And finally:

$$v_m = \frac{2\pi}{T_\phi} m_0 + v_0 \quad (\text{E.7})$$

Where  $m_0 = 0, \pm 1, \pm 2, \dots$

The next point of interest is the limit values for  $m_0$  that can be used in practice.

In this work it is used

$$-15 \leq v_0 \leq 15 \quad (\text{E.8})$$

and

$$-15 \leq v_m \leq 15 \quad (\text{E.9})$$

It is:

$$v_m \leq 15 \text{ or } \frac{2\pi}{T_\phi} m_0 + v_0 \leq 15 \quad (\text{E.10})$$

$$v_0 \geq -15 \text{ or } -v_0 \leq 15 \quad (\text{E.11})$$

By adding (E.10) and (E.11) it is obtained that:

$$\frac{2\pi}{T_\phi} m_0 \leq 30 \quad (\text{E.12})$$

$$\text{Or } m_0 \leq \frac{15T_\phi}{\pi} \quad (\text{E.13})$$

Similarly

$$v_m \geq -15 \text{ or } \frac{2\pi}{T_\phi} m_0 + v_0 \geq -15 \text{ or } -\frac{2\pi}{T_\phi} m_0 - v_0 \leq 15 \quad (\text{E.14})$$

$$v_0 \leq 15 \quad (\text{E.15})$$

By adding (E.14) and (E.15) the result is that:

$$-\frac{2\pi}{T_\phi} m_0 \leq 30 \quad (\text{E.16})$$

$$\text{Or } m_0 \geq -\frac{15T_\phi}{\pi} \quad (\text{E.17})$$

So finally

$$-\frac{15T_\phi}{\pi} \leq m_0 \leq \frac{15T_\phi}{\pi} \quad (\text{E.18})$$

The next point that will be described here is the application of Fourier Transform to (5.27) in order to obtain (5.28). Equation (5.27) in terms of time can be expressed as

$$\Phi_z^{inc}(t) = \Phi_0^{(t)} \exp\left[-\frac{(t - q_0\Delta t + \frac{x}{c})^2}{2W^2\Delta t^2}\right] \sin[2\pi f_c(t - q_0\Delta t + \frac{x}{c})] \quad (\text{E.19})$$

The Fourier transform properties needed are:

$$FT(x(t)) = X(f) \quad (\text{E.20})$$

$$FT(e^{-a^2 t^2}) = \frac{\sqrt{\pi}}{a} e^{-\pi^2 f^2 / a^2} \quad (\text{E.21})$$

$$FT(x(t - t_0)) = X(f) e^{-j\omega t_0} \quad (\text{E.22})$$

$$FT(\sin(2\pi f_c t)) = \frac{j}{2} (\delta(f + f_c) - \delta(f - f_c)) \quad (\text{E.23})$$

$$FT(x_1 \cdot x_2) = X_1 * X_2 \quad (\text{E.24})$$

And the property of convolution of Dirac function needed

$$f(t) * \delta(t - T) = f(t - T) \quad (\text{E.25})$$

Now it is

$$FT\left(e^{-\left(\frac{t}{\sqrt{2W\Delta t}}\right)^2}\right) = \sqrt{\pi} \cdot \sqrt{2W\Delta t} \cdot e^{-(2\pi^2 f^2 W^2 \Delta t^2)} \quad (\text{E.26})$$

And

$$FT(\sin(2\pi f_c t)) = \frac{j}{2} (\delta(f + f_c) - \delta(f - f_c)) \quad (\text{E.27})$$

The convolution of (E.26) with (E.27) will be simple since (E.26) has only Dirac functions so



$$\begin{aligned} & \left( \sqrt{\pi} \cdot \sqrt{2W\Delta t} \cdot e^{-(2\pi^2 f^2 W^2 \Delta t^2)} \right) * \left( \frac{j}{2} (\delta(f + f_c) - \delta(f - f_c)) \right) = \\ & \frac{j}{2} \sqrt{\pi} \cdot \sqrt{2W\Delta t} \cdot \left( e^{-(2\pi^2 (f+f_c)^2 W^2 \Delta t^2)} - e^{-(2\pi^2 (f-f_c)^2 W^2 \Delta t^2)} \right) \end{aligned} \quad (\text{E.28})$$

Now if the amplitude  $\Phi_0$  and time delay  $q_0\Delta t - \frac{x}{c}$  of (E.19) are taken into account,

the final FT of (E.19) can be obtained from (E.28), which is

$$FT(\Phi_z^{inc}) = \Phi_0^{(t)} \frac{j}{2} \sqrt{2\pi} \cdot W\Delta t \cdot \left( e^{-(2\pi^2 (f+f_c)^2 W^2 \Delta t^2)} - e^{-(2\pi^2 (f-f_c)^2 W^2 \Delta t^2)} \right) e^{-j2\pi f q_0 \Delta t} e^{j2\pi f \frac{x}{c}} \quad (\text{E.29})$$

And thus the final form of (5.28) is obtained

$$\tilde{\Phi}_z^{inc} = \Phi_0^{(t)} \frac{j}{2} \sqrt{2\pi} \cdot W\Delta t \left( e^{-(2\pi^2 (f+f_c)^2 W^2 \Delta t^2)} - e^{-(2\pi^2 (f-f_c)^2 W^2 \Delta t^2)} \right) e^{-j2\pi f q_0 \Delta t} e^{jkx} \quad (\text{E.30})$$

The last part of this appendix demonstrates the accuracy of the VF approximation of the  $\tilde{F}_{v_0}^i$  coefficients which are described by (5.37). The derivative of the incident field in time domain of (5.27) in terms of time will be

$$\begin{aligned} \frac{\partial \Phi_z^{inc}(t)}{\partial \rho} &= \Phi_0^{(t)} \exp \left[ -\frac{(t - q_0\Delta t + \frac{x}{c})^2}{2W^2\Delta t^2} \right] \sin \left[ 2\pi f_c \left( t - q_0\Delta t + \frac{x}{c} \right) \right] \left( \frac{-2(t - q_0\Delta t + \frac{x}{c}) \frac{\cos \phi}{c}}{2W^2\Delta t^2} \right) \\ &+ \Phi_0^{(t)} \exp \left[ -\frac{(t - q_0\Delta t + \frac{x}{c})^2}{2W^2\Delta t^2} \right] \cos \left[ 2\pi f_c \left( t - q_0\Delta t + \frac{x}{c} \right) \right] \left( 2\pi f_c \frac{\cos \phi}{c} \right) \end{aligned} \quad (\text{E.31})$$

In frequency domain it will be the derivative of (5.28) which is

$$\frac{\partial \tilde{\Phi}_z^{inc}}{\partial \rho} = \Phi_0^{(t)} \frac{j}{2} \sqrt{2\pi} \cdot W\Delta t \left( e^{-(2\pi^2 (f+f_c)^2 W^2 \Delta t^2)} - e^{-(2\pi^2 (f-f_c)^2 W^2 \Delta t^2)} \right) e^{-j2\pi f q_0 \Delta t} e^{jkx} (jk \cos \phi) \quad (\text{E.32})$$

Each one of the derivatives of the incident field components will be described by (5.36) and (5.39) in frequency and time domain respectively. The field of (E.31) can be expressed as

$$\frac{\partial \Phi_z^{inc}(t)}{\partial \rho} = \sum_{v_0=-\infty}^{\infty} \frac{\partial \Phi_z^{inc, v_0}}{\partial \rho} = \sum_{v_0=-\infty}^{\infty} F'_{v_0}(t) e^{jv_0 \phi} \quad (E.33)$$

The comparison procedure is depicted in Fig. E.1

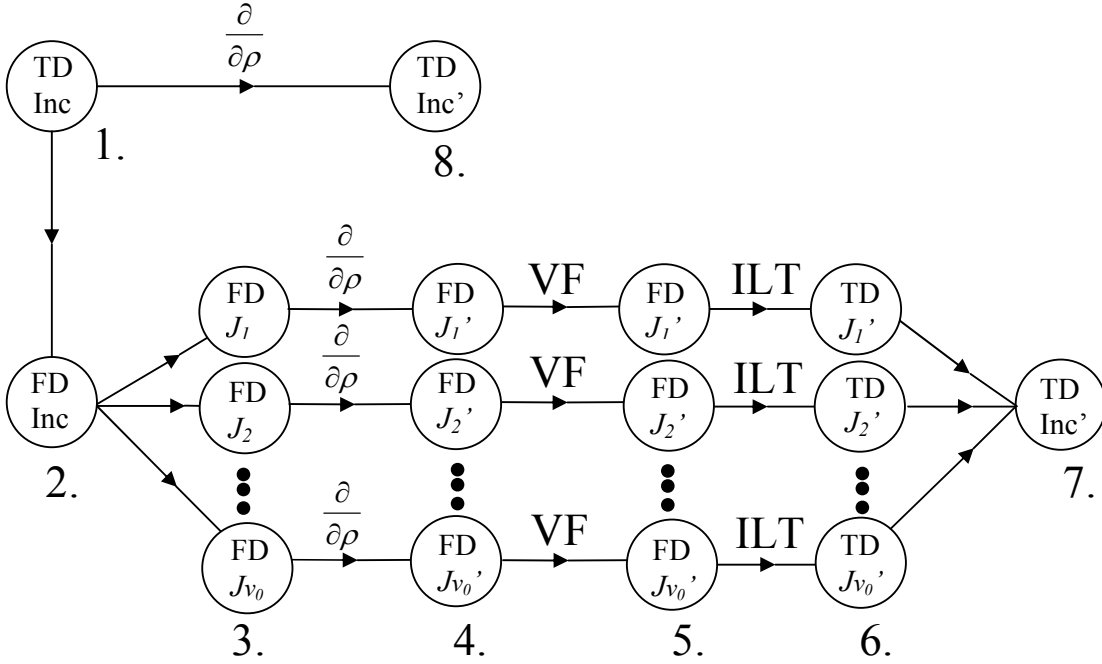
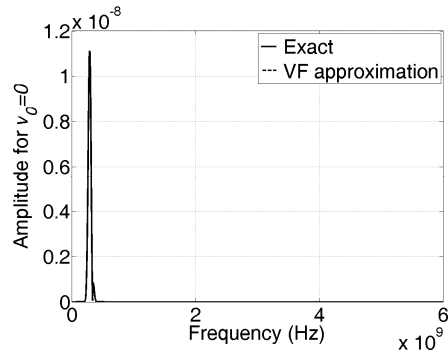
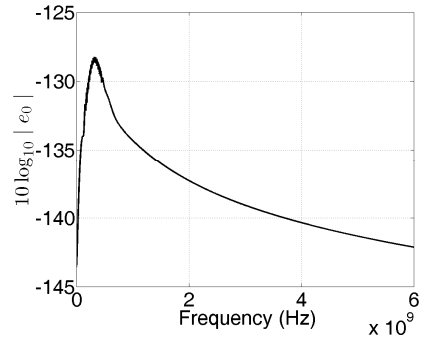


Fig. E.1 Decomposition of the derivative of the incident field harmonics

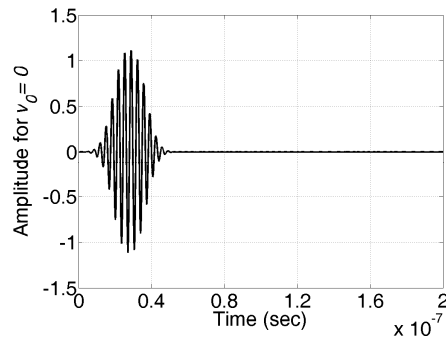
The relation between equations and steps in Fig. E.1 are: 1. (E.19); 2. (5.28); 3. (5.30); 4. (5.35); 5. VF approximation of (5.35); 6. (5.39); 7. (E.33) and 8. (E.31). In Figs E.2 and E.3 the comparisons for  $v_0 = 0$  and  $v_0 = 15$  can be seen. With regard to Fig. E.1, the comparison between steps 4 and 5 along with absolute error between them and the depiction of the field in step 6 can be seen. In Fig. E.4 the comparison for the derivative of the incident field in frequency domain is shown. In this figure (E.32) is compared with the summation of step 5 for all harmonics. In Fig. E.5 the time domain comparison for the whole incident field is shown. The comparison is held between steps 7 and 8. In both cases the absolute error is demonstrated next to the comparisons.



(a)



(b)



(c)

Fig. E.2 For  $v_0 = 0$  (a) frequency domain comparison (b) absolute error (c) time domain function

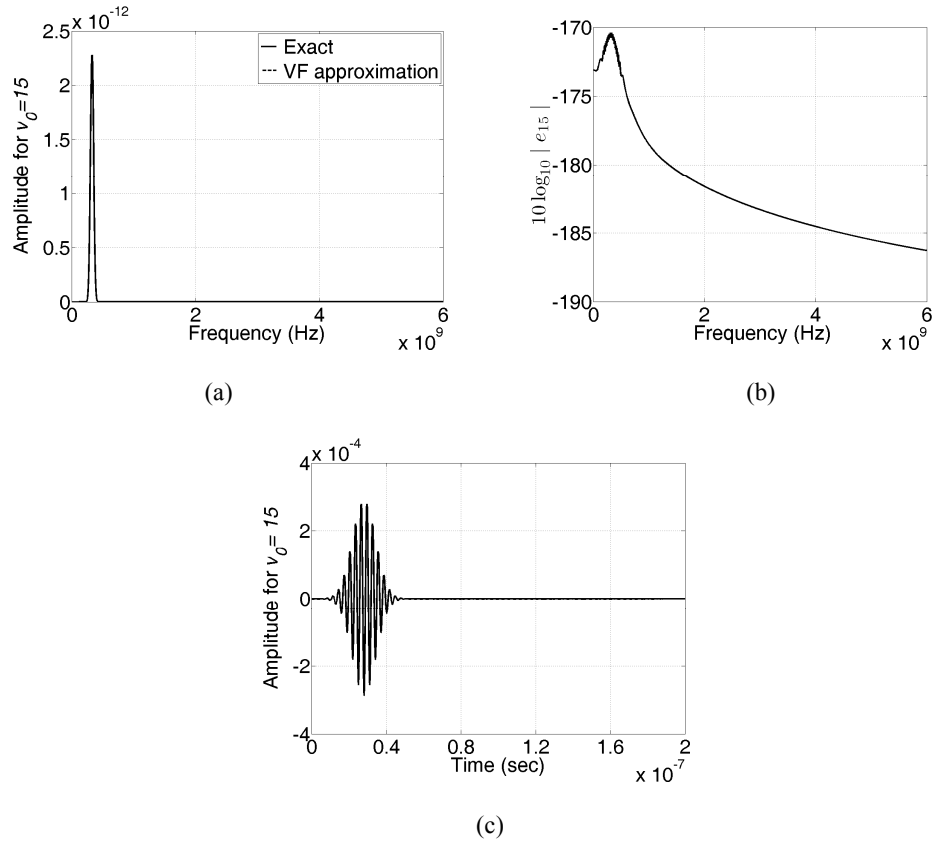


Fig. E.3 For  $v_0 = 15$  (a) frequency domain comparison (b) absolute error (c) time domain function

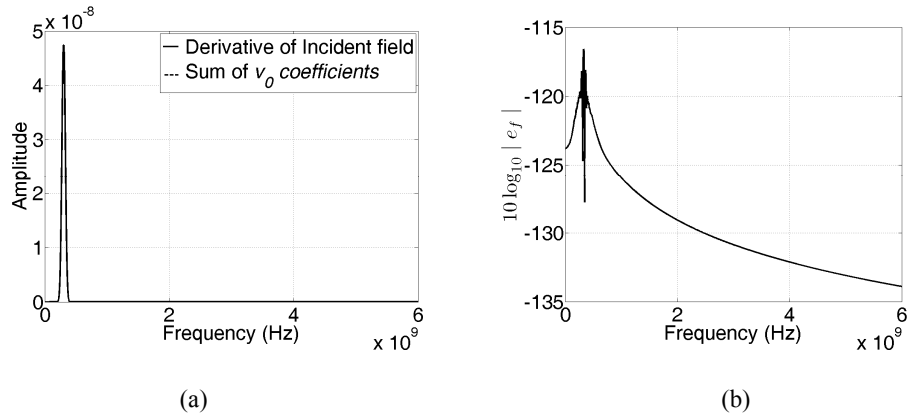


Fig. E.4 (a) Frequency domain comparison (b) absolute error

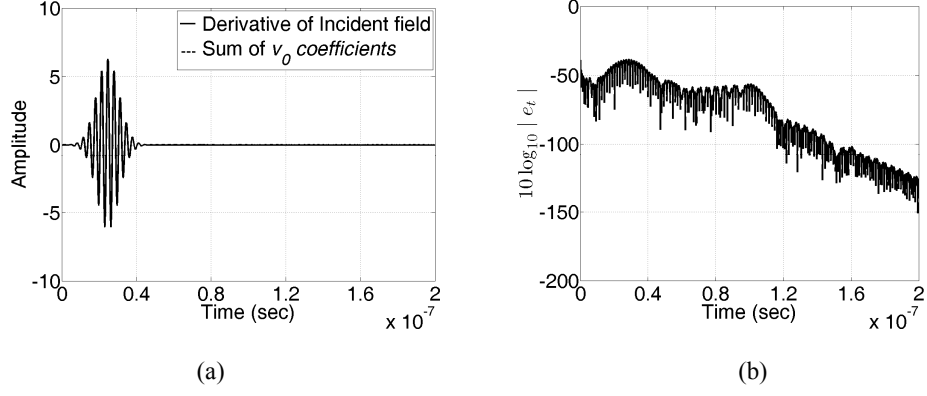


Fig. E.5 (a) Time domain comparison (b) absolute error

The VECTFIT (version 1) input parameters are 4000 samples,  $f_{max} = 6\text{GHz}$ ,  $N = 30$  poles,  $asymflag=1$ . Moreover for the demonstrated comparisons it is  $\Phi_0^{(t)} = 1$ ,  $\phi = 0$  and  $\rho = 1$ . The pulse characteristics and the timestep are  $W = 150$ ,  $q_0 = 700$  and  $\Delta t = 40\text{ps}$

## Appendix F

### Effect of time delay to the Vector Fitting approximation of the incident field components

This appendix investigates the effect of the time delay  $q_0\Delta t$  of the incident pulse to the VF approximation of the pulse and its derivatives. The incident field harmonics are described by (5.30).

The VECTFIT (version 1) input parameters for the partial fraction expansion of (5.32) are 4000 samples,  $f_{max} = 6\text{GHz}$ ,  $N = 30$  poles,  $asymflag=1$ . Moreover for the demonstrated comparison it is  $\Phi_0^{(t)} = 1$ ,  $\phi = 0$  and  $\rho = 1$ . The pulse width and the timestep are  $W = 150$  and  $\Delta t = 40\text{ps}$ . Now the experimentation for different values of delay (a)  $q_0 = 700$ , (b)  $q_0 = 1000$ , (c)  $q_0 = 1500$  and (d)  $q_0 = 2000$  timesteps will be shown. In Figs. F.1-F.4 the VF results for these four delays respectively are depicted. In all figures the frequency domain and time domain comparison for the whole incident field and the absolute error are shown. For the frequency domain comparison (5.28) was used as the reference solution and the VF approximated summation of (5.29) was investigated. For the time domain comparison (5.27) was used as a reference and (5.34) was investigated.

As can be seen for the first two cases the results are comparable but then they become worse. It is worth investigating whether the results would improve if the time delay was considered to be zero ( $q_0 = 0$ ) and the time domain functions were shifted to introduce the desired delay (e.g. by 700 timesteps). In Fig. F.5 the same frequency and time domain comparisons as in the previous figures for  $q_0 = 0$  are shown. As can

be seen, the fact that the function used is not causal had a negative effect on the VF approximation. In Fig F.7 the frequency domain comparison of the incident orders 0, 5, 10, 15 is depicted.

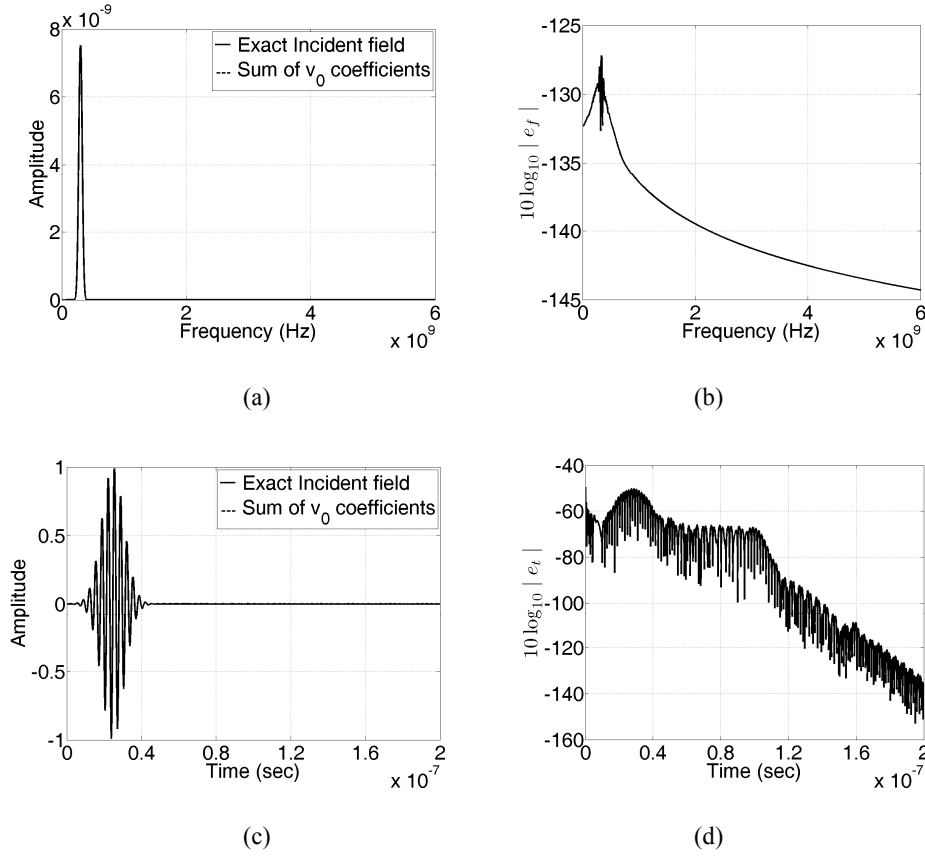


Fig. F.1. Delay 700 timesteps (a) frequency domain comparison (b) frequency domain error  
(c) time domain comparison (d) time domain error

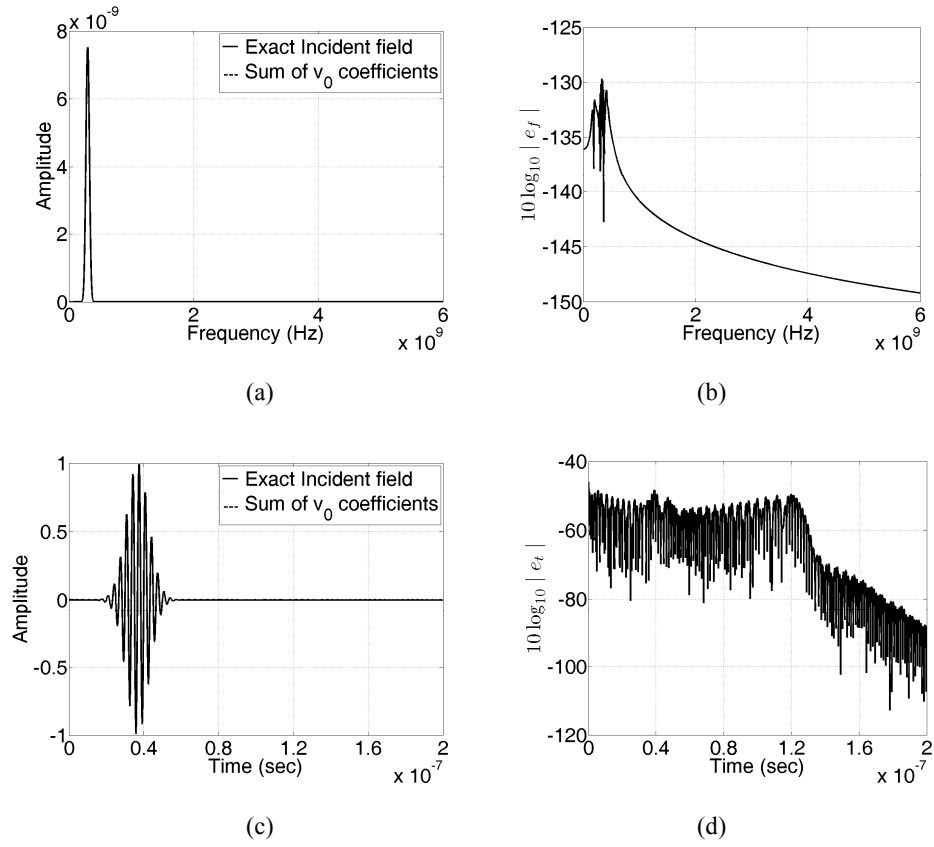
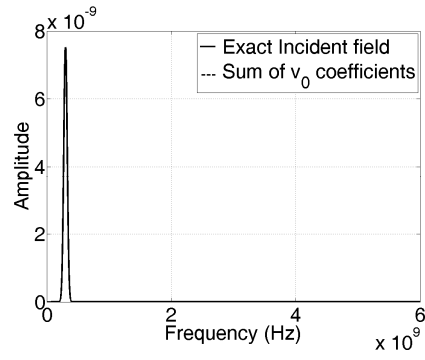
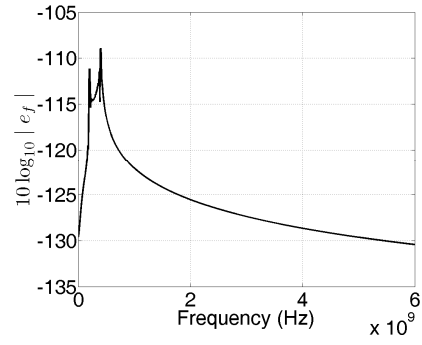


Fig. F.2. Delay 1000 timesteps (a) frequency domain comparison (b) frequency domain error  
(c) time domain comparison (d) time domain error

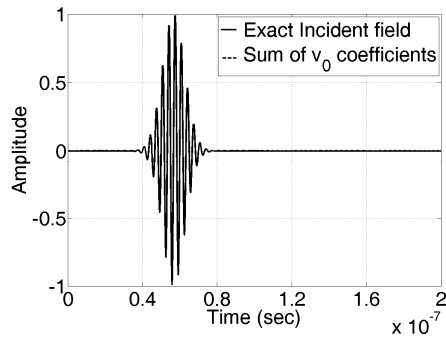




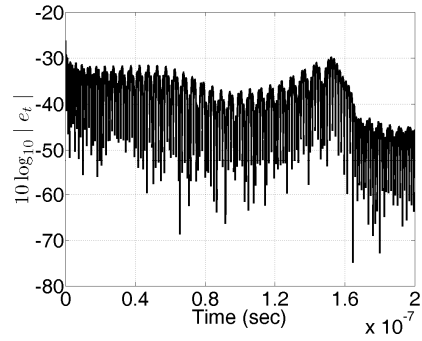
(a)



(b)

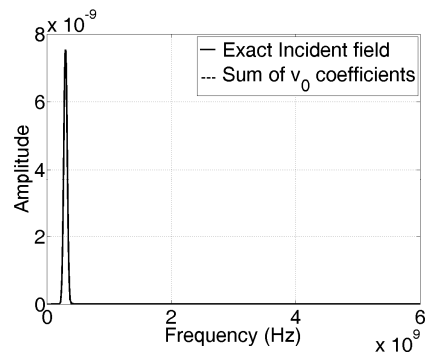


(c)

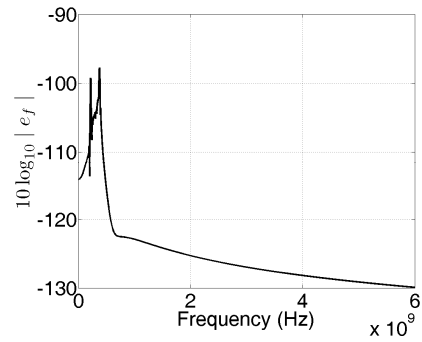


(d)

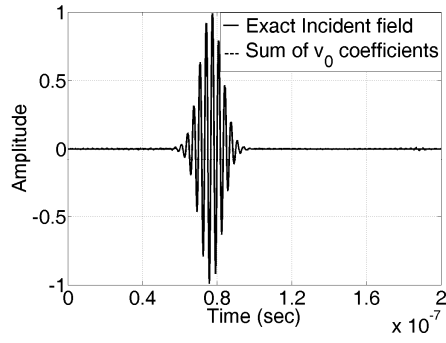
Fig. F.3. Delay 1500 timesteps (a) frequency domain comparison (b) frequency domain error  
(c) time domain comparison (d) time domain error



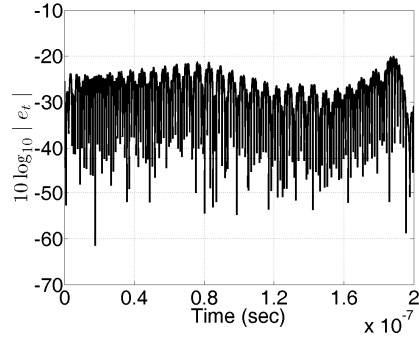
(a)



(b)



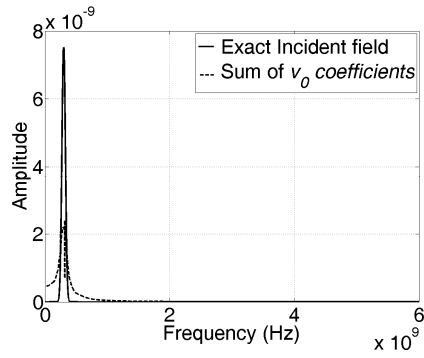
(c)



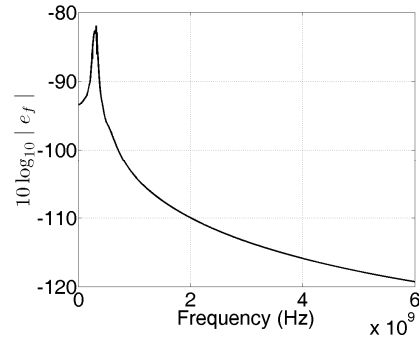
(d)

Fig. F.4. Delay 2000 timesteps (a) frequency domain comparison (b) frequency domain error

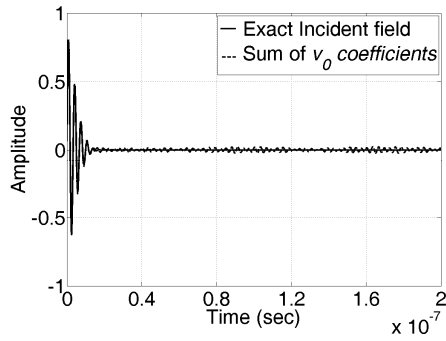
(c) time domain comparison (d) time domain error



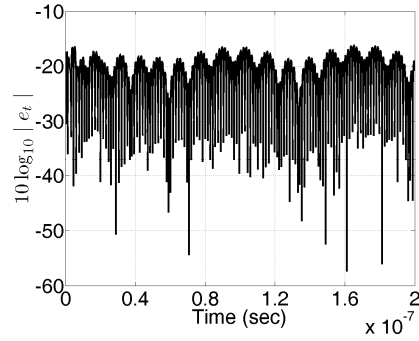
(a)



(b)



(c)



(d)

Fig. F.5. Delay 0 timesteps (a) frequency domain comparison (b) frequency domain error

(c) time domain comparison (d) time domain error

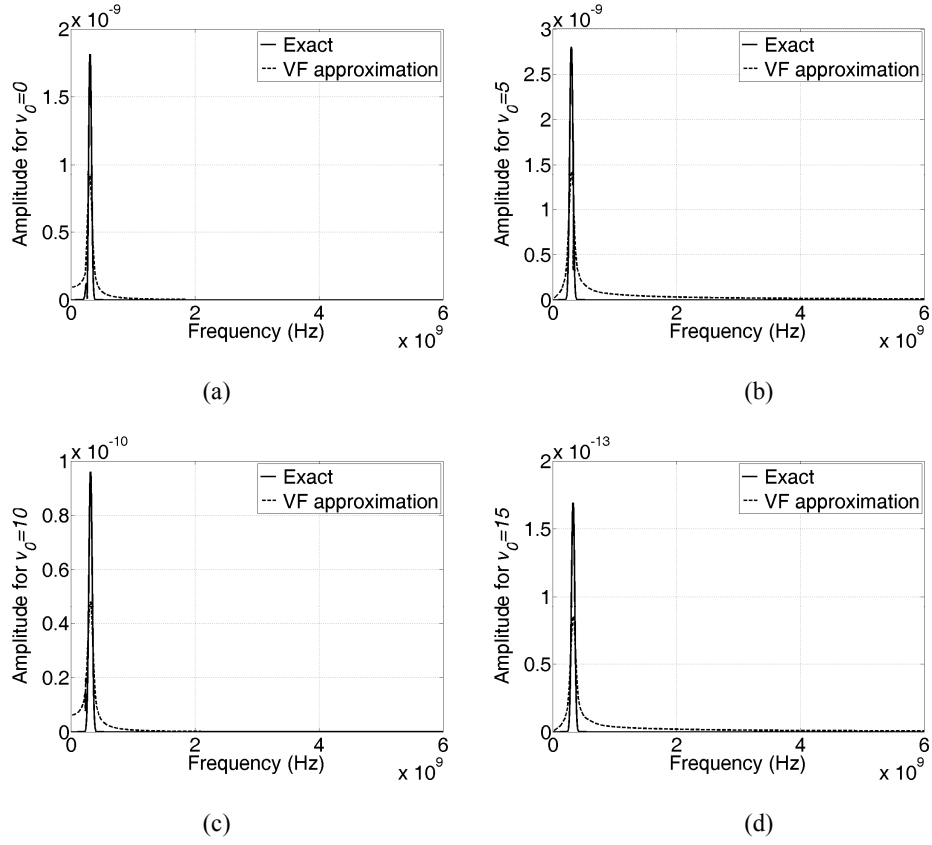


Fig. F.6. Delay 0 timesteps (a)  $v_0=0$  (b)  $v_0=5$  (c)  $v_0=10$  (d)  $v_0=15$

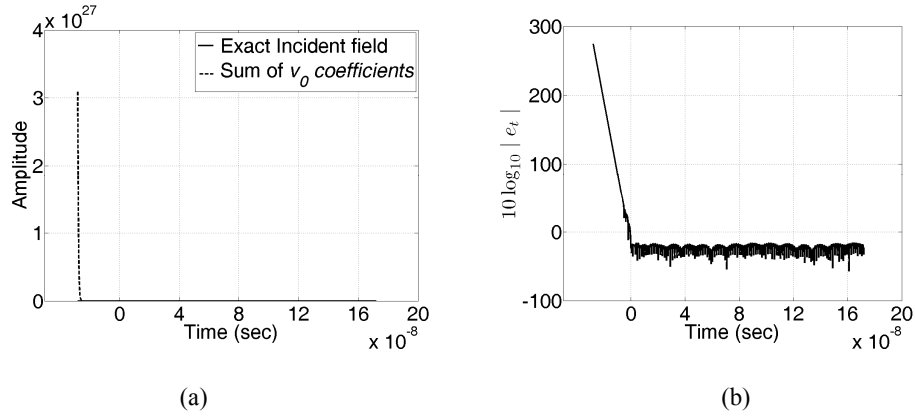


Fig. F.7. Time domain shifting by 700 timesteps (a) time domain comparison (b) error

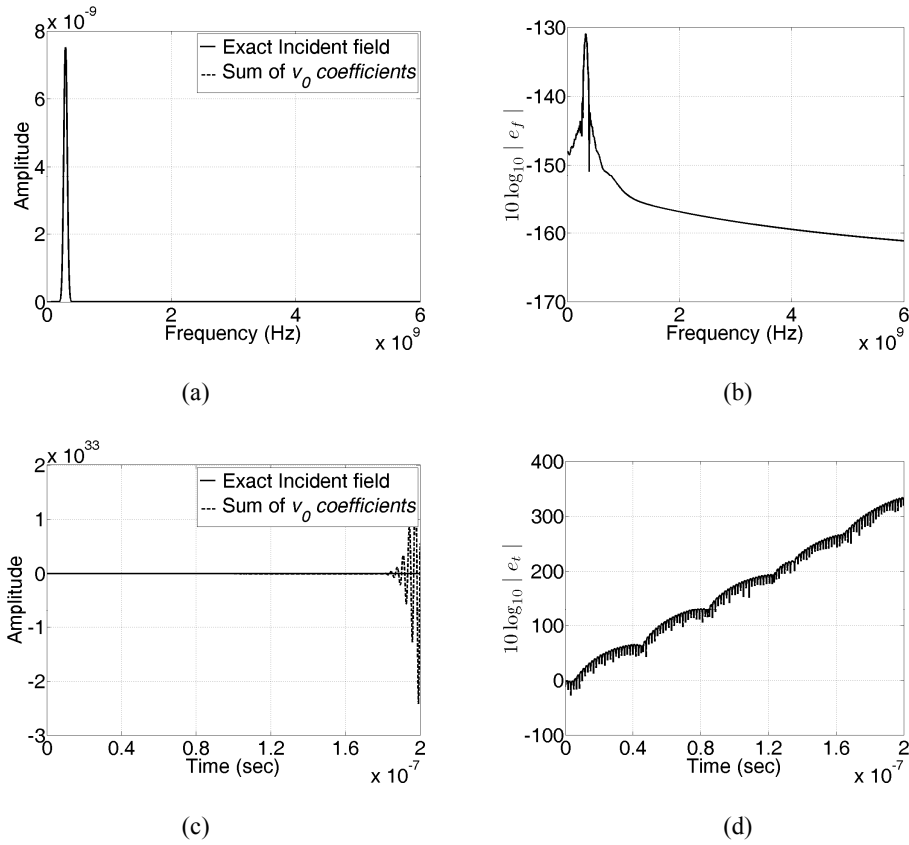
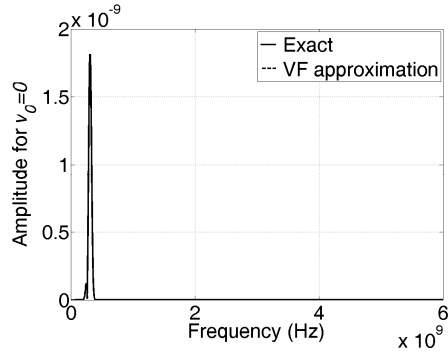
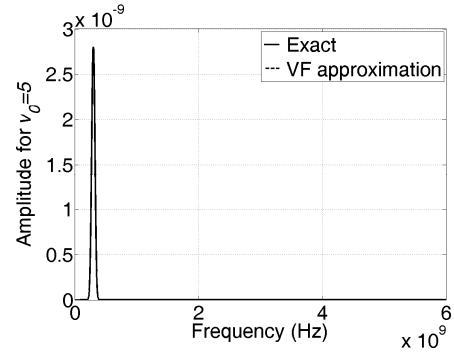


Fig. F.8. Delay 0 timesteps, kill=0 (a) frequency domain comparison (b) frequency domain error  
(c) time domain comparison (d) time domain error

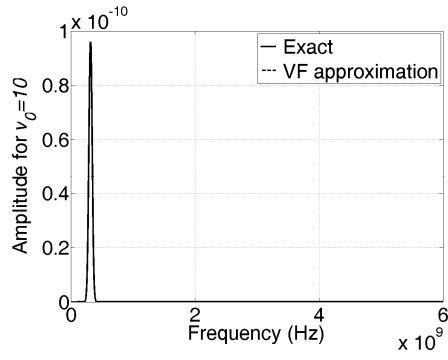
Now if one tried to shift the time domain function by 700 timesteps, the result of Fig. F.7 would be obtained. The last thing considered is to change the VF parameter kill from 2 to 0 and thus include unstable poles in the approximation. The result is depicted in Figs. F.8 and F.9. Apparently the unstable poles improve the frequency domain accuracy in this case but are not useful for time domain work.



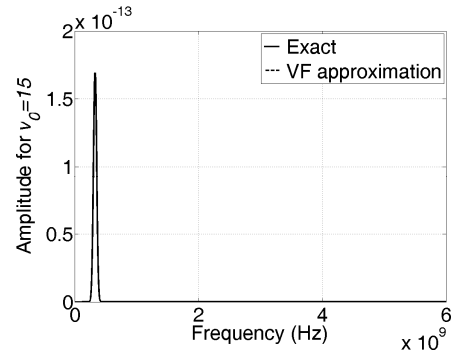
(a)



(b)



(c)



(d)

Fig. F.9. Delay 0 timesteps, kill=0 (a)  $\nu_0=0$  (b)  $\nu_0=5$  (c)  $\nu_0=10$  (d)  $\nu_0=15$

